EFFECTS OF PARTICLE SIZE AND AIR FLOW RATES ON THE RUNAWAY TEMPERATURE OF BITUMINOUS COAL AT 290K < T < 700K

V. M. Malhotra* and J. C. Crelling**

* Department of Physics
** Department of Geology
Southern Illinois University, Carbondale
Illinois 62901-4401

INTRODUCTION

Spontaneous ignition and combustion of coal are major problems not only for actual mining of coal but also for its transportation and for industrial users. Most coals are prone to spontaneous combustion, but their susceptibility to ignition increases as the coal rank decreases (1). However, there are many anomalies to this straight rank order susceptibility. Chamberlain and Hall (1) have in fact, pointed out that some higher rank coals may be more susceptible to spontaneous ignition than lower rank coals.

The causes and mechanisms of spontaneous ignition are enigmatic because exceptions exist for every previously-suggested, single cause. Several models have been advanced to describe spontaneous heating (1-4), however. Among these are coal rank , electrostatic effects, geological factors, temperature, microbial ignition, the reduction in reactivity due to deterioration, air flow rates, particle size, pyrite content, porosity and water wetting of coal.

The purpose of this research was to examine the factors which may contribute to spontaneous ignition of ultrafine (particle size < 250 μm) bituminous coals and maceral enriched fractions under storage, air flow and/or dense phase pneumatic conditions and to understand physical interactions and chemical reactions pathways which may lead to spontaneous ignition of bituminois coals. We have initiated spontaneous ignition, FTIR, DSC, TGA and EPR measurements to accumulate data which can be used to propose mathematical models for spontaneous ignition of stored and pneumatically conveyed coals. In this report, we present our preliminary results on a high-volatile bituminous coal subjected to ignition temperature and FTIR measurements.

EXPERIMENTAL

To examine the effects of air flow temperature, particle size and air flow rates on the surface properties of coal, a high-volatile bituminous coal from Elkhorn #3 seam (Kentucky) was chosen. The coal samples were crushed and sieved and were divided into following particle size ranges : <44 μm , >63μm <75μm, >75μm <106μm, >106μm <150μm, >150μm <250μm, >250μm <300μm, >850μm <900μm.

The experimental arrangement used for determining the effects of air flow temperature and air flow rates on the coal's surface temperature is shown diagrammatically in Figure 1. The coal samples were packed in a quartz tube (10x120mm), and the sample tube

was inserted in the combustion tube assembly. The reaction zone was supplied with two thermocouples (T_1 and T_2) whose hot junctions were positioned along the axis of the sample bed. Thermocouple T_2 monitored the temperature of the fluid at the entrance of the sample tube; while thermocouples T_1 and T_3 monitored the temperature of the sample and exit gases, respectively. The sample tube's location in the tube (750mm length) was determined by the residence time required by the flowing gas to attain the required stable temperature at the entrance of the sample tube. The gas temperature was monitored for 1 hour before the sample tube was inserted in the combustion tube assembly. The compaction and packing of the sample in the tube plays an important role in determining whether exothermic reactions resulted or not. Therefore, every effort was made to ensure uniform compaction of the sample for each run.

Two grams of coal sample of various particle sizes were inserted in the sample tube and subjected to ignition experiments. Ignition was arbitrarily defined as the lowest air temperature which caused any part of the sample to exceed 150 K above the set temperature of the furnace. This value was chosen as an indication of a runaway reaction. Experience has shown that a rapid temperature rise, if one were to occur at all, would take place within a few minutes of the introduction of air, generally less than 20 minutes. If ignition did not occur, a fresh batch of the coal sample was used and the air temperature raised 10K higher than before air was introduced and the sequence was repeated. All FTIR spectra were obtained on an IBM IR-32 FTIR spectrometer equipped with an IBM 9000 comupter. The alkali halide pellet technique was employed to record the spectra.

RESULTS AND DISCUSSION

Ignition Experiments:

Ignition experiments on high-volatile bituminous coals showed that the ignition temperature is strongly dependent on the mode of preheating the sample to the ignition temperature point, particle size, air flow rates, and sample compaction. When using air alone for preheating, it was found to be impossible to attain a uniform sample temperature just before ignition. Accordingly, a technique was evolved to first raise the temperature of the sample close to the ignition temperature by passing a stream of hot nitrogen or carbon dioxide through the sample. Once the constant temperature of the sample was obtained, the stream of gas was switched to air. A similar inert preheating procedure has been used by Hardman et.al. (5) to determine the spontaneous ignition temperature of activated carbons.

The ignition temperatures of three, high-volatile bituminous coals from Elkhorn #3, Ohio #5 and Pittsburgh seam are reported in Table 1. These three coals were chosen because of their large differences in their petrographic composition, especially in their vitrinite and exinite content. It has been suggested (1,2) that there is a close relationship between the coal maceral type and spontaneous oxidation potential. Chamberlain and Hall (1) demonstrated this kind of role when they found that exinites oxidized much more readily than vitrinites and inertinites. If such is the case then one will expect Ohio #5 coal to show the lowest ignition temperature. In fact, Ohio

#5 shows the highest ignition temperature among the three coals examined. Our preliminary results suggest that there may not be any correlation between the petrographic composition and ignition temperature. The sample bank, on which ignition experiments are conducted, needs to be expanded before arriving at definite conclusions.

TABLE 1

Ignition Temperatures of Three High-Volatile Bituminous Coals and Their Selected Petrographic Parameters.

	Elkhorn #3 Seam	Ohio #5 Seam	Pittsburgh Seam
Air Flow Rate (cm^3/min)	900	900	900
Particle Size (μm)	<45	<45	<45
Ignition Temperature (K)	593±10	683±10	673±10
Reflectance (%)	0.93	0.74	0.79
Exinite (vol%)	9.10	26.20	3.90
Vitrinite (vol%)	75.20	55.30	84.20
Volatile Matter (wt%)	33.86	34.70	35.80
Fixed Carbon (wt%)	57.12	43.70	53.20
Moisture (wt%)	2.45	4.20	1.40
Ash (wt%)	6.57	17.40	9.60

Effects of Air Flow Temperature :

Surface reactions of coal under dense-phase pneumatic transport or under storage conditions play a crucial role in determining the initial heatup of coal. Consequently, it is of interest to determine the exothermic reaction pathways and the effects of the physical parameters on such reactions. The Elkhorn #3 seam coal was chosen to evaluate these effects since it showed the lowest ignition temperature. When coal samples of various particle size were inserted in the ignition tube assembly at temperatures lower than the ignition temperature, a typical 'particle temperature vs. time' plot is observed and is shown in Figure 2. Based on these profiles two parameters are defined:

$$\Delta T \equiv \text{Runaway Temperature} \equiv T_s' - T_g(t) \qquad 1)$$

$$\Delta t \equiv \text{Heatwidth} \equiv \text{Time period for which } T_s(t) > T_g(t), \qquad 2)$$

where T_s' is the maximum coal surface temperature, $T_s(t)$ is the coal surface temperature at time t, and $T_g(t)$ is the temperature of the flowing air at time t. Even though ΔT is arbitrarily defined, it represents the rise in coal surface temperature due to exothermic reactions under air flow conditions. In addition, ΔT and Δt measures the overall energy balance since they are related to the generation and dissipation of heat.

Figures 3 and 4 show the effect of air flow temperature ($290\ K < T_g < 700\ K$) on runaway temperature (ΔT) and heatwidth (Δt) values for Elkhorn #3 coal, respectively for three particle sizes. ΔT and Δt values were determined by using nitrogen preheat treatment before introducing air stream. The results indicate that there is a sudden jump in ΔT value at $T_g \geq 493$ K for particle size < 106 μm. As the particle size increases, the T_g value required to induce a sudden jump in ΔT value also increases. In fact, for particle size > 850 μm

no jump in ΔT value is observed at 290 K < T_g < 700 K with or without inert gas preheat treatment. This result suggests that there is a critical particle size below which Elkhorn #3 coal will be very susceptible to spontaneous ignition. This result is at variance with the recent numerical model proposed by Brooks and Glasser (3). From their numerical solution of the steady state equations, they suggested that the coal in the particle size range of (sub 1 mm) > (particle size) < (6 mm) is most susceptible to spontaneous combustion. Their prediction of the particle size effect on the spontaneous ignition is not consistent with our experimental results.

The effects of air flow rates and coal particle size on runaway temperature and heatwidth of Elkhorn #3 seam were also examined. To determine these effects, the air flow temperature T_g = 493 K was chosen since a sudden jump in ΔT value was observed at this temperature. The samples were inserted into the ignition tube assembly under air stream. The results are shown in Figures 5 and 6 for particle size and air flow rates, respectively. The experimental data suggests a power relationship between the runaway temperature (ΔT) and the particle size of coal. The coal surface temperature (T_s) under air flow rate of 900 cm^3/min suggests a relation:

$$T_s = T_g + 4726\ (\text{Particle Size, } \mu m)^{-0.84} \qquad 3)$$

Schmidt and Elder (6) have suggested a correlation between the rate of oxidation and particle size.

$$\text{Rate of oxidation} = K^3\ (\text{Specific Surface Area})^{0.5}\ , \qquad 4)$$

where K is a constant dependent on both rank and temperature. It can be seen that our results cannot be explained by equation 4 even if it is assumed that particle shape is random. Our results suggest that Elkhorn #3 coal will be most susceptible to spontaneous ignition for particle size < 150 μm. The runaway temperature shows a parabolic dependence on the air flow rates. The data shown in Figure 6 for > 63 μm < 75 μm particle size was fitted to a 3rd order polynomial:

$$T_s = T_g - 3.80 + 0.12\ (\text{Air Flow Rate}) + 8.3 \times 10^{-5}\ (\text{Air Flow Rate})^2 \qquad 5)$$

These results indicate that the susceptibility of spontaneous ignition will increase as the coal particle size decreases. In addition, there may be a critical air flow rate range for which heat generated may exceed heat dissipated.

FTIR Measurements :

FTIR measurements were carried out on the Elkhorn #3 seam bituminous coal to determine the effect of air flow temperature (T_g) on the structure of coal. The samples used for the FTIR measurements were the same samples which were subjected to air flow temperature measurements (i.e., Figure 3, < 43 μm). The samples were withdrawn from the ignition tube assembly after reacting with flowing air (900 cm^3/min) at 290 K < T < 700 K for 10 hours. Figure 7 shows the effect of air flow temperature (T_g) on the FTIR spectrum of Elkhorn #3 coal. The details of the FTIR analysis of bituminous coal and the effects of low temperature (<423K) oxidation on its vibrational spectrum have been reported earlier in the literature (7-9). The assignment of the

observed vibrational bands was based on these published works. The FTIR spectrum of unprocessed Elkhorn #3 coal can be characterized by : (a) A very broad band with maximum near ~ 3350 cm^{-1} was observed and is attributed to hydroxyl (-OH) groups. However, it was not possible to discern whether this band was due to moisture in KBr pellets, moisture in coal or hydroxyl groups which are part of organic matrix. We believe that this band is due, in fact, to a combination of the three sources mentioned above. (b) A weak absorption band at 3030 cm^{-1} was assigned to aromatic CH stretch. (c) A shoulder at 2960 cm^{-1} and two main absorption peaks at 2920 and 2850 cm^{-1} were observed and are attributed to CH_3 groups and aliphatic CH_3, CH_2, and CH groups, respectively. (d) A weak shoulder at 1700 cm^{-1} was observed and is assigned to C=O stretch. (e) The aromatic C=C bonds produced a strong absorption at 1600 cm^{-1}, and it is believed that some oxygen containing functional groups also contribute to its intensity. (f) The medium intensity band at 1445 cm^{-1} is due mainly to CH_2 groups in coal. However, CH_3 bending mode and aromatic stretching vibrations may also contribute to the intensity of this band. The weak observed band at 1375 cm^{-1} has been assigned to CH_3 groups. (g) A weak absorption at 1261 cm^{-1} has been assigned to ethers of the types C_6H_5-O-CH_3 or -CH_2O-CH_3- . In addition to 1261 cm^{-1} band, a broad weak band centered around ~ 1160 cm^{-1} was also observed and is assigned to aldehydes and/or ketones and/or ether groups in the Elkhorn coal. (h) Three absorption bands were observed in the aromatic region i.e., at 870, 812 and 754 cm^{-1}. The band at 870 cm^{-1} has been assigned to substituted benzene rings and to aromatic HCC rocking. The band at 812 cm^{-1} has been attributed to substituted benzene rings with two neighboring H, while the band at 754 cm^{-1} is assigned to monosubstituted benzene rings and O-substituted benzene rings. Additional bands due to inorganic materials were also observed but will not be discussed in this paper.

The effects of air flow temperature (T_g) on the FTIR spectra of Elkhorn #3 coal in the frequency range 4000 - 1100 cm^{-1} have been summarized in Table 2. The absorbance changes reported in this table were determined by subtracting the unprocessed coal spectrum from the processed (290K < T_g < 700K) coal spectrum. It was not possible to follow the changes in the organic bands of the processed coal at frequency < 1100 cm^{-1} due to strong overlapping inorganic bands. Attempts were made to remove the contribution of the inorganic bands by subtracting the spectrum of low temperature ash. However, this subtraction resulted in erroneous bands in the difference spectrum due to changes in the intensity and broadening of the inorganic bands at $T_g \geq$ 473K. The effect of air flow temperature on the intensity of aromatic CH stretch at 3034 cm^{-1} and aliphatic CH stretch at 2917 cm^{-1} is shown in Figures 8 and 9, respectively. Figure 10 shows the absorbance changes in the accumulative oxygen functionalities of coal as a function of air flow temperature. The y-axis of this graph represents the sum of absorbance changes at 1835, 1780 - 1700, and 1560 cm^{-1}. At $T_g \geq$ 640K, only inorganic bands were observed signifying that all the organic matter in coal has combusted. Thus the absorbance change points at $T_g \geq$ 640K in the graphs 8,9 and 10 represent a net loss of these functional groups i.e., all the organic matter is lost.

TABLE 2

The Effects of Air Flow Temperature on the Frequency of Principal Absorption Changes of Elkhorn #3 Bituminous Coal at 290K < T_g < 700K.

Air Flow Temp.(K)	Frequency (±4 cm^{-1})
343	2913(+),2845(+),1700(+),1445(+)
393	2917(-),2851(-),1835(+),1770(+),1700(+),1445(-),1375(-), 1021(-)
443	3034(-),2917(-),2851(-),1770(+),1700(+),1560(+),1445(-), 1375(-),1109(+)
493	3034(-),2917(-),2851(-),1835(+),1770(+),1725(+),1560(+), 1445(-),1219(+),1136(+)
543	3034(-),2917(-),2851(-),1835(+),1770(+),1721(+),1555(+), 1445(-),1267(+),1211(+),1100(+)
593	3034(-),2917(-),2851(-),1835(+),1770(+),1725(+),1560(+), 1451(-), *
643	3039(-),2920(-),2855(-),1698(-),1651(-),1593(-),1441(-), *, **
693	3048(-),2918(-),2857(-),1692(-),1598(-),1445(-), *, **

\+ Sign indicates that absorption increased or new bands appeared.
\- Sign indicates that absorption decreased or bands disappeared.
* At frequency < 1200 cm^{-1}, it was difficult to follow the organic bands due to overlapping inorganic bands.
** Only inorganic bands were observed.

The increase in intensity of aliphatic vibrations (i.e., at 2917, 2851, and 1445 cm^{-1}) at $T_g \leq$ 343K was most surprising. At these low temperatures a loss of some volatile matter is expected, and this loss should result in a decrease in the intensities of aliphatic vibrations. No intensity enhancement of these vibrations results if nitrogen or carbon dioxide is used under identical gas flow and temperature conditions. The intensity of the vibrational bands not only depends on the concentration of the functional groups in the sample but also on their dipole moment i.e., on the transition probability. We do not believe that the concentration of aliphatic groups has increased at $T_g \leq$ 343K, but we conjecture that an oxygen attack on coal somehow alters the dipole moment of the aliphatic groups at this temperature. At $T_g >$ 343K there is a steady decrease in the intensity of aliphatic bands at 2917, 2851 and 1445 cm^{-1}, with a major decrease located at 393K $\leq T_g \leq$ 493K. As can be seen from Figure 9, there is no correlation between the absorbance change and the runaway temperature of this coal. Similar results were observed for aliphatic bands at 2851 and 1445 cm^{-1}. These results suggest that the loss of aliphatic groups from the coal matrix, in the form of volatile products, plays a little role in the magnitude of the runaway temperature. Under air flow conditions, the volatile products are expected to be swept away from the sample toward the exhaust of the combustion tube, thus drastically decreasing the residence time of volatile products around the sample. If the volatile combusts on the coal's surface as it leaves the coal, the combustion exothermic reactions should contribute to the runaway temperature. It is possible that these exothermic reactions contribute to the early profile of heatwidth, but it seems unlikely since no correlation exists between

absorbance changes at 2917, 2851, and 1445 cm^{-1} and heatwidth. Figure 8 shows that the aromatic CH stretch vibration at 3030 cm^{-1} remains unchanged at 290K < T_g < 400K. However, it is interesting to note that as the runaway temperature increases the intensity of CH stretch vibration decreases. This decrease is mirrored along with alterations in the aromatic region's vibrations i.e., at 900 - 700 cm^{-1}. At present it is not possible to calculate the absorbance changes in this region due to interference from inorganic bands. The dependence of aromatic stretch vibration on the runaway temperature strongly suggests that it is the oxidation of the aromatic groups that results in major contribution to the runaway temperature. As T_g increases from 293K, the C=O stretch vibration at 1700 cm^{-1} increases and shows maximum contribution at 443K. Mirrored with the increase in C=O stretch at 1700 cm^{-1} a very broad, weak band is observed in OH stretch, suggesting the formation of carboxylic acid groups largely of aliphatic type. It seems that the oxidation of aliphatic groups attached to the aromatic structure contributes very little to the runaway temperature. At 493K $\leq T_g \leq$ 593K, strong absorbance bands at 1835, 1770, 1725, 1560, 1300 - 1100 cm^{-1} appear in the spectrum, indicating massive oxidation reactions in coal which leads to the formation of anhydrides, aldehydes, lactones, esters, ketones and ethers. Figure 10 shows the effect of air flow temperature on the accumulative absorbance changes in the oxygen functional groups at 1835, 1770, 1725, 1700, and 1560 cm^{-1} of Elkhorn #3 coal. These results clearly show that these oxidation reactions make major contribution to the heat generated i.e., to runaway temperature. It was surprising that at T_g = 493K, with the coal's surface temperature reaching 790K, complete combustion of the sample did not result. It appears that the oxygen functional groups generated on the surface of coal inhibit complete combustion reaction at $T_g \leq$ 593K. Diffuse reflectance - and photoacoustic - FTIR studies are in progress on these samples to evaluate the effects of incomplete combustion reactions and runaway temperature.

ACKNOWLEDGEMENTS

This work was supported in part by U.S. Department of Energy under contract No. DE-SC22-86PC91272.

REFERENCES

1. E. A. C. Chamberlain and D. A. Hall, Colliery Guardian 221, 65 (1973).
2. J. R. Herring and F. C. Rich, " Spontaneous Coal Combustion; Mechanisms and Prediction" , Proc. 1983 International Conf. on Coal Science, August 15-19, Pittsburgh, p753 (1983)
3. K. Brooks and D. Glasser, Fuel 65, 1035 (1986).
4. J. M. Bell and R. Roche, " The European Experience With Indirect Firing of Pulverized Coal and United State Applications", Proc. Pittsburgh Coal Conf., Pittsburgh, p713 (1984).
5. J. S. Hardman, C. J. Lawn and P. J. Street, Fuel 62, 632 (1983).
6. L. Schmidt and E. Elder, Ind. Eng. Chem. 32, 249 (1940).
7. J. S. Gethner, Applied Spectroscopy 41, 50 (1987).
8. N. E. Cooke, O. M. Fuller and R. P. Gaikwad, Fuel 65, 1254 (1986).
9. P. C. Painter, R. W. Snyder, M. Starsinic, M. M. Coleman, D. W. Kuehn and A. Davis, Applied Spectroscopy 35, 475 (1981).

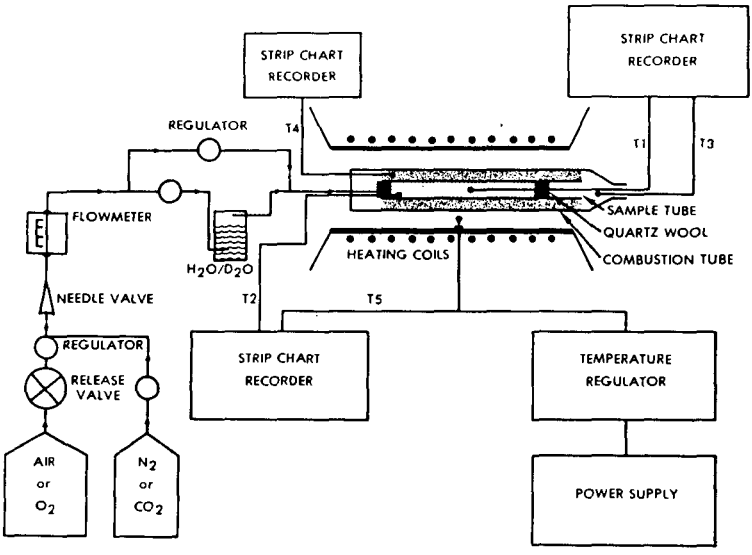

Fig. 1 Combustion tube assembly.

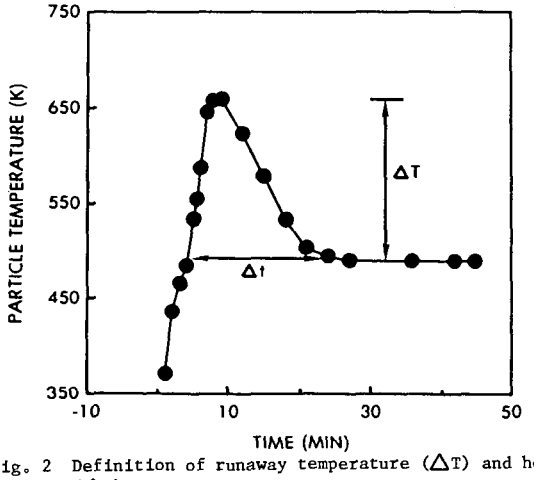

Fig. 2 Definition of runaway temperature (ΔT) and heatwidth (Δt).

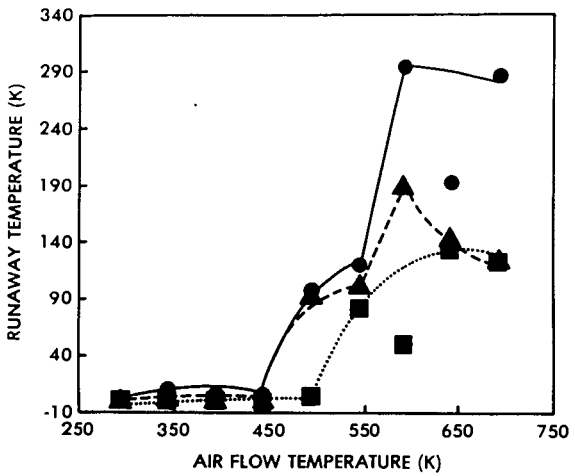

Fig. 3 Effect of air flow temperature on the runaway temperature of Elkhorn Coal. Air flow rate = 900 cc/min., ●<45 μm, ▲ 75> <105 μm, ■ 150> <250 μm.

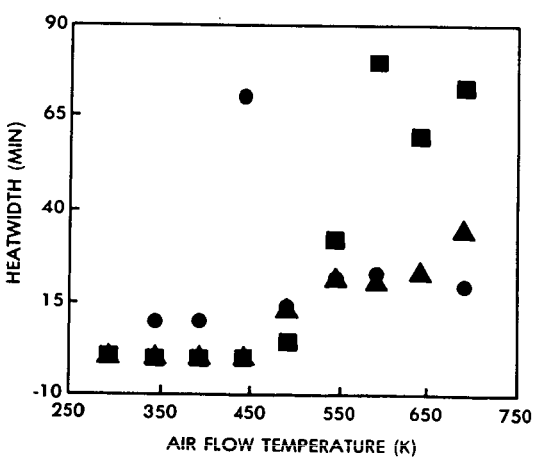

Fig. 4 Effect of air flow temperature on the heatwidth of Elkhorn coal. Air flow rate = 900 cc/min., ●<45 μm, ▲75> <105 μm, ■ 150> <250 μm.

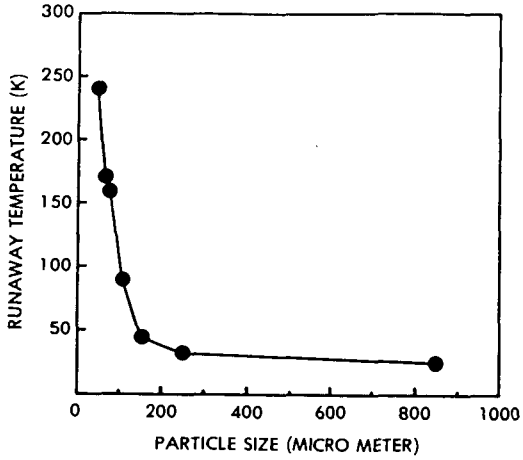

Fig. 5 Effect of particle size on the runaway temperature . $T_g \doteq$ 493K, air flow rate = 900 cc/min.

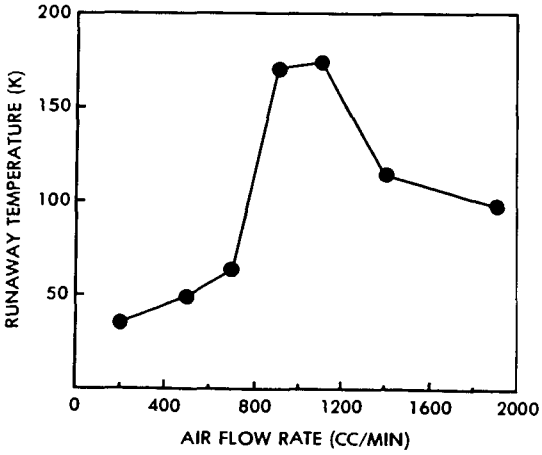

Fig. 6 Effect of air flow rate on the runaway temperature. T_g = 493K, particle size = $\lesssim$45 μm.

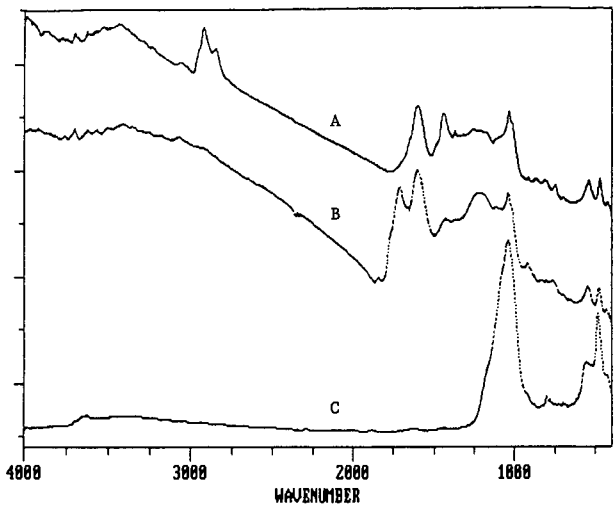

Fig. 7 FTIR spectrum of Elkhorn coal subjected to air flow experiments. (A) 293K, (B) 493K, and (C) 693K.

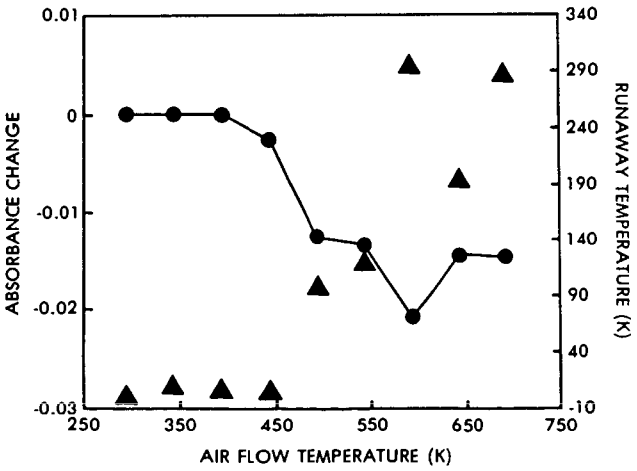

Fig. 8 Effect of air flow temperature on the absorbance of 3034 cm^{-1} band (●) and runaway temperature (▲).

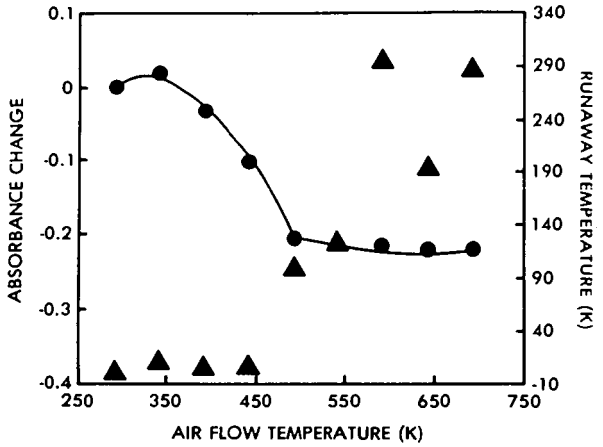

Fig. 9 Effect of air flow temperature on absorbance of 2917 cm^{-1} band (●) and runaway temperature (▲).

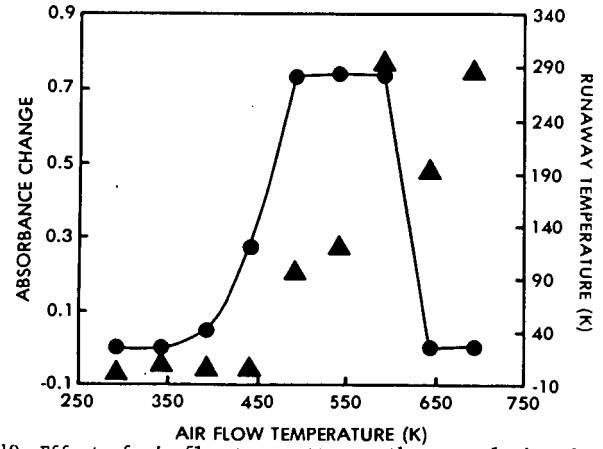

Fig. 10 Effect of air flow temperature on the accumulative absorbance of 1835, 1770, 1725, 1700 and 1560 cm^{-1} bands (●) and runaway temperature (▲).

COAL-WATER MIXTURE COMBUSTION USING OXYGEN-ENRICHED AIR AND STAGED FIRING

Y.C. Fu, G.T. Bellas, and J.I. Joubert

U.S. Department of Energy
Pittsburgh Energy Technology Center
P.O. Box 10940
Pittsburgh, Pennsylvania 15236

ABSTRACT

Coal-water mixture (CWM) combustion experiments using oxygen-enriched air were conducted in an oil-designed 700-hp watertube boiler using a bituminous CWM. The results indicated that the use of oxygen-enriched air increased carbon burnout, reduced uncontrolled fly ash emissions, and reduced combustion air preheating requirements. The boiler efficiency increased because of reduced flue gas heat losses. The improvement in boiler performance compared to an experiment without oxygen enrichment was significant when using only 2-3 percent enrichment of air (23-24 volume percent oxygen). Using combustion air enriched to 22.7 percent oxygen by volume, the required air preheating temperature was reduced to 192°F as compared to 325°F required with no oxygen enrichment, while the carbon conversion efficiency at full boiler load was increased from 95.0 percent to 97.4 percent.

Experiments on CWM combustion were also conducted using staged firing with and without oxygen-enriched air. The NO_x reduction achieved at a first-stage air/fuel stoichiometric ratio of 0.76 was about 33 percent, but it was accompanied by a reduction in combustion efficiency and an increase in particulate emissions. The use of oxygen-enriched air in the burner zone increased flame stability and carbon burnout while maintaining the effectiveness of staged combustion; however, additional experiments are needed to optimize burner-operating parameters to achieve significant NO_x reduction.

INTRODUCTION

The use of oxygen-enriched air for coal-water mixture (CWM) combustion could result in several positive effects on boiler performance: (1) preheated air requirements should be reduced or eliminated, thereby permitting the use of CWM in smaller industrial boilers that do not usually have high-temperature air preheaters; (2) the volume and velocity of the flue gas will be reduced, decreasing potential erosion problems in the boiler convection banks; and (3) boiler efficiency should increase because of reduced stack heat losses, partially compensating for loss in boiler efficiency owing to water in the slurry. Taschler et al. examined the impact of these effects on boiler operating economics and steam generation capacity in large-scale boilers (1).

Coal-water mixture combustion experiments using oxygen-enriched air were conducted at Pittsburgh Energy Technology Center (PETC) in a 700-hp watertube boiler using a commercial CWM fuel prepared from bituminous coal. The objectives of these tests were to determine (1) the optimal point of oxygen injection, (2) the minimal oxygen concentration required to stabilize the CWM flame without preheating the combustion air, and (3) the effects of boiler load conditions on oxygen enrichment requirements.

The CWM combustion experiments were also conducted using staged firing with and without oxygen-enriched air. Staged combustion is one of the most commonly applied NO_x-control techniques for coal-fired boilers (2-4). The boiler is operated with a primary fuel-rich combustion zone, in which both thermal and fuel NO_x formation is minimized. The initial combustion step is then followed by a

fuel-lean zone to complete the combustion of the residual fuel. Staged combustion in the PETC boiler was achieved by introducing the first-stage air through the burner air register, and the second-stage air through three air ports installed on a side wall of the boiler.

EXPERIMENTAL

The test unit is a Nebraska 700-hp "D"-type watertube industrial boiler originally designed for No. 6 oil firing. The boiler generates about 24,000 lb/hr of steam at full load. Figure 1 is a sectional plan view through the firebox and convection section of the boiler. Preheated combustion air is provided by an external source. The Coen single-air-zone register provided with the boiler was modified for these experiments. One of two modifications made to the air register was a diameter change of the sheet metal shroud, which increased the secondary-air linear velocities at the exit throat of the register. The other simple change was the insertion of a center air tube to establish a stable flame front. The center tube has a fixed air spinner, and both the center-tube-air and secondary-air feeds have independent flow-control systems. This allows considerable flexibility in burner-operating capabilities (5). Extensive instrumentation and a computer-controlled data acquisition system provide a large amount of data for detailed analysis and evaluation of the experiments.

Tertiary (second-stage) air is injected through three ports installed at approximately one third of the furnace length from the front wall. The port design incorporates removable sleeves to allow changing of port size to permit control of the second-stage air flow and the injection pattern.

Figure 2 is a cross-sectional view of the burner used for oxygen-enrichment tests. Oxygen is introduced through a specially fabricated oxygen guide tube (3 1/2-inch schedule-10 Monel pipe) surrounding the burner-gun guide tube. A Coen nozzle with eight 15/64-inch holes and a 60° spray angle was used. A 30° cocurrent center-air diffuser and a 45° cocurrent oxygen-guide-tube diffuser were installed during the combustion experiments.

CWM COMBUSTION USING OXYGEN-ENRICHED AIR

The use of oxygen-enriched combustion air reduces the amount of nitrogen flowing through a combustion process, resulting in elevated flame temperatures. Figure 3 shows adiabatic flame temperatures for the combustion of CWM with oxygen-enriched air at an oxygen/fuel stoichiometric ratio of 1.15. Theoretical flame temperature curves were generated at combustion air preheating temperatures of 77° (ambient), 300°, and 500°F using the PETC Multiphase Equilibrium Program for a CWM containing 70 percent Pittsburgh seam bituminous coal. The adiabatic flame temperature using normal air (O_2 = 20.69 volume percent) preheated to 500°F is 3393°F; the same flame temperature can be achieved by using 23.25 volume percent oxygen-enriched air at ambient temperature.

Because of the reduction in the amount of nitrogen per unit quantity of fuel flowing through the furnace, the amount of flue gas from the combustion of CWM using oxygen enrichment will be decreased. The decrease in flue gas volume, expressed in standard cubic feet per pound of CWM (at 70°F and 14.7 psia), is illustrated in Figure 4. For example, at 23 volume percent and 25 volume percent oxygen concentrations in the combustion air, and an oxidizer/fuel stoichiometric ratio of 1.15, the flue gas quantities decrease by 8 percent and 15 percent, respectively, compared to the quantity produced when using normal air.

Oxygen enrichment should reduce combustion air preheat requirements and reduce flue gas heat losses. Oxygen enrichment should also provide a greater range of flammability and improved flame stability compared to combustion air preheating.

A commercial CWM, ARC-COAL, produced by the Atlantic Research Corporation and containing 70 percent Eastern U.S. bituminous coal, was used in the oxygen enrichment experiments (see Table 1). Analysis of the experimental results indicates that the addition of oxygen to the combustion air results in higher carbon conversion and boiler efficiencies. Using 500°F combustion air at an oxygen level equivalent to 22.9 percent by volume in air, a carbon conversion efficiency of 97.0 percent and a boiler efficiency of 81.3 percent were obtained (see test 2 in Table 2). The base-line test (test 1) at 500°F preheating without oxygen enrichment resulted in 95.0 percent carbon conversion and 79.3 percent boiler efficiency. Because of the improvement in carbon burnout with oxygen enrichment, the carbon content of the fly ash decreased by more than 25 percent (Table 3). As a consequence, particulate emissions were also reduced. With oxygen enrichment, however, NO_x emissions increased from 0.69 to 1.00 lb NO_2/MMBtu (tests 1 and 2 in Table 3). The increased flame temperature due to oxygen enrichment apparently increased the formation of thermal NO_x.

Test 3 of Tables 2 and 3 was conducted at reduced boiler load (~70 percent of maximum capacity) using oxygen-enriched air. A slight improvement (1%) in carbon conversion was obtained compared to test 2, which was conducted at full load.

Test 4 was carried out at full load and at minimum combustion air preheat temperature (192°F) using 22.7 percent oxygen-enriched air. An improvement in boiler performance compared to the test without oxygen enrichment (test 1) is noticeable, even though the preheating temperature was reduced substantially. The minimum combustion air preheating required for a stable flame is affected by a number of variables, including CWM volatility, heating value, and oxygen enrichment (flame temperature). Other variables, such as excess oxygen level and combustion air swirl, are also important. With increased oxygen concentration in the oxygen-enriched air, the combustion air flow per unit quantity of fuel at a constant oxidizer/fuel ratio is reduced. This would reduce the intensity of the combustion air swirl and possibly adversely affect the flame stability.

CWM COMBUSTION USING STAGED FIRING

Combustion experiments were conducted at full boiler load and at total air/fuel stoichiometric ratios of 1.15 to 1.21 using combustion air preheated to about 490°F (see Tables 4 and 5). Stoichiometric ratios of the first-stage air (atomizing air plus center-tube air plus secondary air) to fuel were varied between 0.76 and 0.97 while the remaining air (tertiary air) was diverted through the side wall ports. Boiler operation could not be sustained at a stoichiometric ratio less than 0.75 in the primary combustion zone because of flame instabilities.

A base-line experiment performed without air staging (with the tertiary air ports blocked) produced NO_x emission levels of 0.77 lb/MMBtu (see test 1, Tables 4 and 5). As primary-zone stoichiometry was reduced, emissions of NO_x declined; the NO_x reduction achieved with the primary-zone stoichiometry of 0.76 was about 33 percent. The reduction in NO_x emissions, however, was achieved with some decrease in combustion efficiency. As the first-stage stoichiometric ratio was reduced from 1.15 to 0.76, the carbon conversion efficiency decreased from 95.7 percent to 92.2 percent.

It is apparent that the conditions created by deep staging (primary zone stoichiometry of less than 0.75) tend to be opposite of those conducive to good flame stability and high carbon-conversion efficiencies. Improvements in combustion efficiency may be attainable by changing the tertiary-air port location and/or velocity to increase the efficiency of tertiary-air mixing in the second stage. However, because of limitations in primary-zone temperature and residence time, it may be difficult to achieve large reductions in NO_x emissions while

firing coal or CWM in an oil-designed boiler without exacerbating the problem of fuel burnout.

CWM COMBUSTION USING STAGED FIRING AND OXYGEN-ENRICHED AIR

One approach to increasing the primary-zone temperature, flame stability, and carbon burnout under deep-staging conditions is to use oxygen-enriched air. Tables 6 and 7 show the results of CWM combustion experiments using both staged firing and oxygen-enriched air. Oxygen was introduced into the primary combustion zone through the burner oxygen guide tube (see Figure 2). These experiments were conducted using 356°F to 413°F combustion air at 1.14 to 1.16 overall oxygen/fuel stoichiometric ratio and at an overall oxygen concentration of about 26 percent by volume. Carbon conversion efficiencies ranging from 95.6 percent to 97.8 percent and boiler efficiencies ranging from 81.0 percent to 82.8 percent were obtained as the oxygen/fuel stoichiometric ratio in the primary combustion zone was varied from 1.14 (unstaged) to 0.76.

Carbon conversion efficiency was reduced only slightly and the boiler efficiency remained high as the degree of staging increased. However, a reduction in NO_x emissions was observed when the primary-stage stoichiometry was reduced to 0.76, as shown in Figure 5. With oxygen enrichment, the measured NO_x emissions at all primary-stage stoichiometries were higher than those measured in experiments conducted with no oxygen enrichment, even though the oxidizer was preheated to a higher temperature in the latter experiments.

These results suggest that the problem of reduced carbon burnout in staged combustion can be alleviated with the use of oxygen-enriched air in the burner zone while achieving a moderate reduction in NO_x emissions. However, even the experiment that provided the greatest reduction in NO_x emissions resulted in levels that are quite high (>0.6 lb NO_2/MMBtu). To further reduce NO_x emissions, it would be necessary to decrease the primary-stage stoichiometry (for this furnace, to less than 0.76). Additional experiments are required to determine if a significant reduction of NO_x emissions can indeed be achieved using oxygen-enriched air in a staged combustion system while maintaining a high level of carbon conversion efficiency.

CONCLUDING REMARKS

The combustion experiments conducted in the 700-hp watertube boiler with bituminous CWM indicate that the use of oxygen-enriched air resulted in a decrease in the level of air preheating required and an improvement in carbon burnout. The reduction in the volume of flue gas lowered heat losses and increased boiler efficiency. Using combustion air enriched to 22.7 percent oxygen by volume, the air preheating temperature could be reduced to 192°F as compared to ~325°F required with no oxygen enrichment. The improvement in boiler performance compared to the test without oxygen enrichment was noticeable even with the use of only 2-3 percent enrichment of air (23-24 volume percent oxygen).

By using staged air admission during CWM combustion in the oil-designed boiler, a reduction in NO_x emissions on the order of 1/3 was achieved. The reduction in NO_x emissions, however, was achieved with some decrease in combustion efficiency. Using 490°F combustion air at 15-21 percent excess, as the primary-stage stoichiometry was reduced from 1.15 to 0.76, NO_x emissions decreased from 0.77 lb/MMBtu to 0.52 lb/MMBtu while the carbon conversion efficiency decreased from 95.7 percent to 92.2 percent.

The use of oxygen-enriched air in the primary combustion stage increased the flame stability and diminished the problem of reduced carbon burnout while achieving moderate reduction of overall NO_x emissions. Using 356°F to 413°F combustion air at 14-16 percent excess and at an overall oxygen concentration of about 26

volume percent, NO_x emissions decreased from 0.88 lb/MMBtu to 0.65 lb/MMBtu as the primary-stage stoichiometry decreased from 1.14 to 0.76. The carbon conversion and boiler efficiencies, however, remained high and were in the ranges of 96-98 percent and 81-83 percent, respectively.

DISCLAIMER

Reference in this paper to any specific commercial product, process, or service is to facilitate understanding and does not necessarily imply its endorsement or favoring by the United States Department of Energy.

REFERENCES

1. Taschler, D.R., Nolte, F.S., and Stringfellow, T.E., "The Impact of Oxygen-Enriched Combustion of Coal Water Slurries on the Economics and Performance of Large Scale Boilers," Sixth International Symposium on Coal Slurry Combustion and Technology, Orlando, Florida, June 25-27, 1984.

2. Perkinson, G., "NO_x Controls: Many New Systems Undergo Trials," Chem. Eng., March 9, 1981.

3. Pruce, L., "Reducing NO_x Emissions at the Burner, in the Furnace, and After Combustion," Power, 125, No. 1, 33, January 1981.

4. Itse, D.C., and Penterson, D.C., "NO_x Control Technology for Industrial Combustion System," American Flame Research Committee Symposium on Combustion Diagnostics from Fuel Bunker to Stack, October 5, 1983.

5. Fu, Y.C., Bellas, G.T., and Joubert, J.I., "Combustion Testing of Coal-Water and Coal-Methanol-Water Mixtures in Oil-Designed Boilers," ASME Winter Annual Meeting, New Orleans, Louisiana, December 9-14, 1984, ASME paper 84-WA/RT-93.

Table 1. Typical Analyses of ARC-Coal

	As Received	Dry Basis
Weight Percent Coal	70.59	
Particle Size Consist (% minus-200-mesh)	89	
Proximate Analysis (%)		
Moisture	29.41	--
Volatile Matter	22.40	31.73
Fixed Carbon	42.81	60.65
Ash	5.38	7.62
Ultimate Analysis (%)		
Hydrogen	6.82	5.04
Carbon	56.86	80.53
Nitrogen	1.08	1.53
Sulfur	0.53	0.75
Oxygen	29.33	4.53
Ash	5.38	7.62
Heating Value (Btu/lb)	10,140	14,365
Viscosity (cP @ 100 sec^{-1} after 50 seconds, 79°-81°F)	584	
Ash Fusion Temperatures (°F)		
Initial Deformation Temp.	2580	
Softening Temp.	2670	
Fluid Temp.	2700	

Table 2. Operating Conditions and Boiler Performance, CWM Tests with Oxygen Enrichment

Test Number	1	2	3	4
O_2 Vol. % in Comb. Air	20.69	22.91	22.83	22.68
Overall Oxygen/Fuel Stoichiometric Ratio	1.16	1.15	1.14	1.25
O_2 Injected (lb/hr)	0	598	385	618
Fuel Flow (lb/hr)	2791	2733	1843	2833
Steam Flow (lb/hr)	24250	24390	16540	24010
Thermal Input (MMBtu/hr)	30.20	29.22	19.67	30.04
Combustion-Air Temp. (^oF)	501	491	490	192
Total Air Flow (lb/hr)	24656	21423	14379	25052
Atomizing-Air Flow (lb/hr)	1287	1316	1312	1338
Atomizing-Air Pressure (psig)	128	126	129	130
Fuel Pressure at Burner (psig)	109	105	88	148
Center-Tube-Air Flow (lb/hr)	4910	4749	4516	5804
Avg. Flue Gas Temp. (^oF)	500	509	463	503
Carbon Conversion Eff. (%)	95.0	97.0	98.1	97.4
Boiler Eff. (%) (Heat Loss Method)	79.3	81.3	82.2	80.0
Heat Loss Due to H_2O in Fuel (%)	3.21	3.26	3.21	3.24
Heat Loss from Burning Hydrogen in Fuel (%)	3.74	3.79	3.74	3.95

Table 3. Flue Gas Emissions in CWM Tests with Oxygen Enrichment

Test Number	1	2	3	4
Flue Gas Analysis				
O_2 (%)	2.9	3.1	3.9	4.2
CO_2 (%)	15.1	17.1	16.2	15.7
CO (ppm)	72	50	55	51
SO_2 (ppm)	646	693	667	662
(lb/MMBtu)	1.24	1.20	1.24	1.23
NO_x *(ppm)	499	800	753	703
(lb/MMBtu)	0.69	1.00	1.00	0.94
THC (ppm)	1.7	0.8	1.0	3.0
Particulate Emissions (Uncontrolled)				
(lb/hr)	168	133	45	124
(lb/MMBtu)	6.07	4.91	2.49	4.26
C in Fly Ash (%)	46.6	34.6	41.4	33.9

*As ppm of NO + ppm of NO_2; calculated as lb of NO_2/MMBtu.

Table 4. Operating Conditions and Boiler Performance, CWM Tests with Staged Combustion

Test Number	1	2	3	4
Total Air/Fuel Stoichiometric Ratio	1.15	1.20	1.21	1.15
First-Stage Air/Fuel Stoichiometric Ratio	1.15	0.97	0.85	0.76
Fuel Flow (lb/hr)	2888	2969	2940	3026
Steam Flow (lb/hr)	23990	24630	24080	24000
Thermal Input (MMBtu/hr)	30.74	31.77	31.45	32.40
Combustion-Air Temp. (^{o}F)	491	490	481	494
Total Air Flow (lb/hr)	25380	27170	27210	26460
Secondary-Air Flow (lb/hr)	17740	15360	13300	12110
Center-Tube-Air Flow (lb/hr)	6096	5340	4682	4122
Tertiary-Air Flow (lb/hr)	--	5264	8046	8985
Atomizing-Air Flow (lb/hr)	1164	1206	1182	1243
Atomizing-Air Pressure (psig)	127	126	129	125
Fuel Pressure at Burner (psig)	114	119	117	124
Avg. Flue Gas Temp. (^{o}F)	525	542	528	519
Carbon Conversion Eff. (%)	95.7	95.5	93.8	92.2
Boiler Eff. (%) (Heat-Loss Method)	77.5	77.6	76.9	76.0
Heat Loss Due to H_2O in Fuel (%)	3.55	3.55	3.53	3.51
Heat Loss from Burning Hydrogen in Fuel (%)	3.81	3.81	3.79	3.77

Table 5. Flue Gas Emissions in CWM Tests with Staged Combustion

Test Number	1	2	3	4
Flue Gas Analysis				
O_2 (%)	2.1	3.5	3.7	3.4
CO_2 (%)	15.8	14.5	14.5	14.5
CO (ppm)	81	74	92	124
SO_2 (ppm)	608	597	610	658
(lb/MMBtu)	1.10	1.19	1.20	1.28
NO_x (ppm)*	560	532	469	375
(lb/MMBtu)*	0.77	0.76	0.66	0.52
THC (ppm)	0.8	3.1	2.1	3.3
Particulate Emissions (uncontrolled)				
(lb/hr)	209	185	203	248
(lb/MMBtu)	7.37	6.33	7.01	8.33
C in Fly Ash (%)	48.9	40.7	50.4	53.3

*As ppm of NO + ppm of NO_2; calculated as lb of NO_2/MMBtu.

Table 6. Operating Conditions and Boiler Performance, CWM Tests with Staged Combustion and Oxygen Enrichment

Test Number	1	2	3	4
O_2vol.% in Combustion Air	26.2	26.3	26.4	26.0
Overall Oxygen/Fuel Stoichio-Ratio	1.14	1.16	1.16	1.14
First-Stage Oxygen/Fuel Stoichiometric Ratio	1.14	1.02	0.88	0.76
Oxygen Injected (lb/hr)	1448	1505	1564	1433
Fuel Flow (lb/hr)	2871	2890	2949	2953
Steam Flow (lb/hr)	23330	23400	23660	23500
Thermal Input (MMBtu/hr)	30.32	30.65	31.77	31.99
Combustion-Air Temp. (°F)	375	356	411	413
Total Air Flow (lb/hr)	18405	18872	19068	19143
Secondary-Air Flow (lb/hr)	12960	10910	8767	7263
Center-Tube-Air Flow (lb/hr)	4293	3638	2944	2389
Tertiary-Air Flow (lb/hr)	--	3166	6213	8299
Atomizing-Air Flow (lb/hr)	1152	1158	1144	1192
Atomizing-Air Pressure (psig)	130	130	131	130
Fuel Pressure at Burner (psig)	117	113	119	122
Avg. Flue Gas Temp. (°F)	489	493	499	496
Carbon Conversion Eff. (%)	97.8	96.8	95.6	96.0
Boiler Eff. (%) (Heat-Loss Method)	82.8	81.8	81.0	81.3
Heat Loss Due to H_2O in Fuel (%)	3.54	3.54	3.50	3.48
Heat Loss From Burning Hydrogen in Fuel (%)	3.51	3.51	3.46	3.44

Table 7. Flue Gas Emissions in CWM Tests with Staged Combustion and Oxygen Enrichment

Test Number	1	2	3	4
Flue Gas Analysis				
O_2 (%)	4.3	5.1	6.1	5.2
CO_2 (%)	19.7	19.0	18.5	18.3
CO (ppm)	64	77	64	79
SO_2 (ppm)	795	818	809	774
(lb/MMBtu)	1.18	1.25	1.25	1.21
NO_x (ppm)*	806	792	814	604
(lb/MMBtu)*	0.88	0.87	0.89	0.65
THC (ppm)	2.2	2.6	2.3	2.3
Particulate Emissions (uncontrolled)				
(lb/hr)	82	110	166	122
(lb/MMBtu)	2.70	3.59	5.23	3.81
C in Fly Ash (%)	44.1	47.8	44.5	55.2

*As ppm of NO + ppm of NO_2; calculated as lb of NO_2/MMBtu.

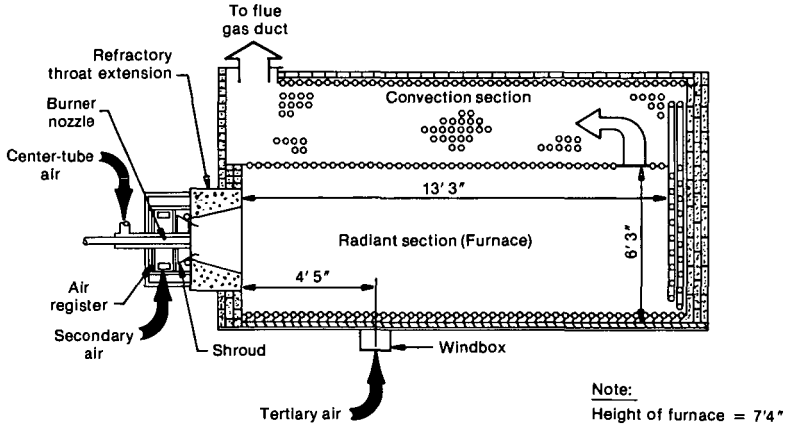

Figure 1. Horizontal cross-sectional view of 700-hp watertube boiler

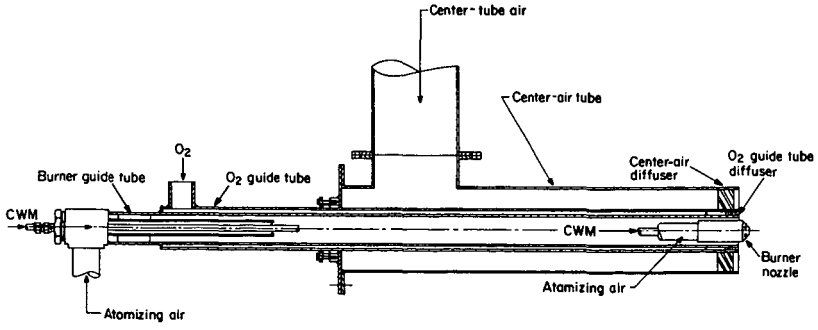

Figure 2. Burner used in oxygen enrichment tests

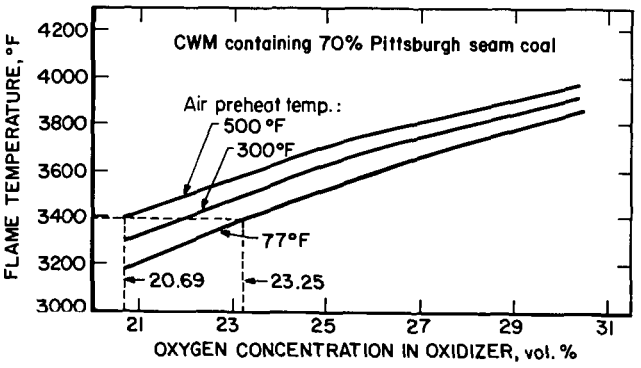

Figure 3. Adiabatic CWM flame temperature with oxygen-enriched air at various combustion air preheat temperatures (oxygen/fuel stoichiometric ratio = 1.15)

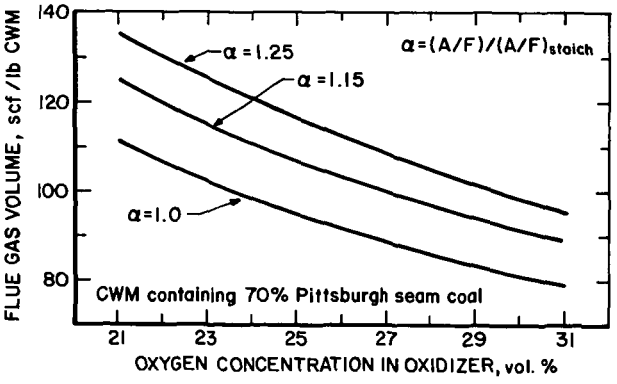

Figure 4. Flue gas volume for CWM combustion with oxygen-enriched air

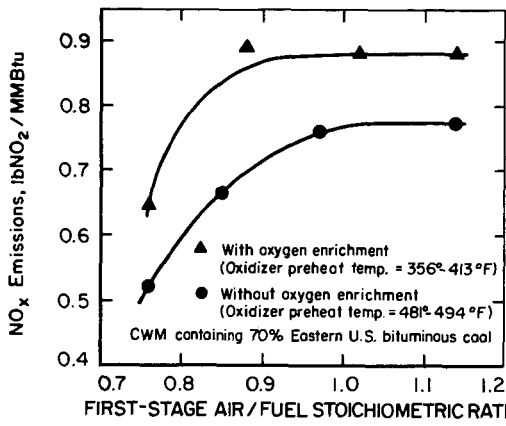

Figure 5. Effect of Staged Firing on NO_x Emissions (Overall oxygen/fuel stoichiometic ratio ≈1.15; full boiler load)

Fluidized Bed Combustion of Petroleum Cokes: Kinetics and Catalytic Effects

Dennis E. Walsh and Gary J. Green

Mobil Research and Development Corporation
Central Research Laboratory, P.O.Box 1025, Princeton, New Jersey 08540

INTRODUCTION

In the fluid coking process, large quantities of coke particles are circulated between a burner vessel and the fluid coking reactor, with the coke-to-fresh feed ratio generally about 7 to 8 pounds of coke per pound of residual feed. During each burning cycle, a portion of coke equivalent to about 5% of the charge is burned off, and the hot coke particles are then returned to the coker supplying process heat. As a result of this type of repeated burning and coke deposition cycle, the coke is deposited in multiple, thin "onion-skin" layers. Product coke is withdrawn from the burner vessel, the temperature of which is maintained between ~595° and 650°C. Because the fluid coking process itself takes place at ~510°C, followed by the coke being first steam stripped and then burned at ~625°C, an essentially "dry" coke product is produced, i.e., one which is free of residual oils.

In the delayed coking process, coke is produced in a batch fashion. Residual oil is fed to a coke drum while a companion drum, used in the previous cycle, is de-coked. Product oil vapors pass upward through the forming coke mass en route to exiting. Coke drum inlet temperatures are maintained at ~485°C-500°C while the outlet is maintained at ~440°C; thus, cooling of the charge takes place during the 24 hour fill cycle. This process, therefore, produces coke at a lower temperature than fluid coking. Hence, the coke product from a delayed coking process is not free of residual oils (~2-10 wt.% on coke).

Although fluid coking is attractive from the viewpoint of higher liquid yield, the coke tends to be higher in sulfur than delayed coke, which could create SO_x pollution problems in any subsequent combustion application. In addition to the sulfur question is that of the intrinsic combustibility of fluid coke vs. delayed coke. Since little information is available in the literature on this point, the present work examined whether process differences have any major impact on the combustion characteristics of the coke products.

A second goal of this study was the investigation of the possibility of catalytically enhancing coke burning rates by employing separate particle catalysis. Though the catalytic oxidation effect of metals impregnated on solid carbonaceous fuel has been recognized for many years, no industrial process using this catalytic technique is in operation due to concerns over the cost of catalyst loss and possible environmental effects of emitted metal particles (1). Fluid bed combustion of solid fuels for steam generation operates at temperatures which may be low enough (~650 to 900°C) for catalytic effects to be operative. Such catalysis would allow increased throughput for a given unit size or permit the use of a smaller unit for a given steam production rate. Catalytically enhanced combustion of solid fuels such as petroleum cokes by active metals on separate particles could obviate the above cited problems associated with direct impregnation of catalysts on a solid fuel.

EXPERIMENTAL

Coke samples were first calcined in nitrogen for ~1 hour at a temperature in excess of the highest anticipated experimental temperature (~650°C) to drive off any residual volatiles which might complicate data interpretation. As noted above, little or no volatiles evolution was observed in the case of fluid coke; delayed coke samples did evolve some volatile constituents. The delayed coke samples included both "needle" and "sponge" cokes, which have different morphologies as reflected by their names. Also, in the case of the delayed coke samples, a brief exposure (~90 sec.) to high temperature air was employed to effect a mild surface area enhancement. Thus, all the samples are compared at "dry" conditions (i.e., free of residual oil volatiles) and at similar initial surface areas. Properties of these materials are given in Table 1. At each temperature, repeat runs with successively smaller coke particle sizes were performed until burning rates remained unchanged, thereby insuring that all burning rate data were uninfluenced by diffusion.

The sample of coke to be burned was diluted to 0.1-1.0 wt.% in a bed of acid washed sand particles. The bed was then fluidized in N_2 and brought to reaction temperature in a three zone furnace. Initiation of the experiment, collection of data and termination of the run were all computer controlled. Essentially, the solenoid valve supplying N_2 to the flow controller closes and the O_2 valve opens to start an experiment. Combustion gases leaving the fluid bed are quenched, dried and filtered. An NDIR monitors the CO and CO_2 concentrations and the computer records the CO_x levels and bed temperature as a function of time. The interval between readings accelerates or decelerates depending upon the CO_x level in the product gases. Bed isothermality was usually $\pm$ 2-3°C and the oxygen supply rate was generally $\geq$10 times the consumption rate. Experiments were conducted over the temperature range from 500-600°C; reactor pressure was atmospheric.

Preparation of candidate catalytic materials was accomplished by impregnation of clean sand using aqueous solutions containing a quantity of metal sufficient to provide the desired loading (generally ~1 wt.%). The dried preparations were then O_2 calcined at ~600°C prior to use. When Pt preparations were made (using H_2PtCl_6), dried samples were H_2 reduced (~2 hours at 425°C) prior to O_2 calcination. A low surface area support (viz. sand) was chosen since solid-solid contacting at the exteriors of the fuel and catalyst particles would be the likely mechanism of any catalytic combustion enhancement; "interior" active sites present in high surface area catalyst formulations would likely be unavailable for catalyzing the primary combustion step ($C+O_2 \rightarrow CO/CO_2$). Metals analyses of catalyst-impregnated sand samples taken from the bed before and after combustion showed that no measurable decrease in catalyst concentration occurred during the course of any of the experiments. In addition, negligibly small amounts of bed material were lost to entrainment.

RESULTS AND DISCUSSIONS

Burning Characteristic of Fluid Coke vs. Delayed Coke

The burning rate data for all coke samples tested were adequately described by first order kinetics over ~85% of the burn off. As illustrated in Figure 1, a plot of the natural log of the fraction of unburned carbon vs. time is well-fit by a straight line, the slope of which is the apparent first order rate constant.

Figure 2 is an Arrhenius plot of the rate constant data obtained for the delayed coker needle coke samples; the activation energy is ~41 kcal/mole. This value is in excellent agreement with that reported recently for the combustion of a sample of petroleum coke used in the preparation of pre-baked anodes for aluminum production (2). This value is also comparable to that observed for uncatalyzed combustion of carbon deposited on solid oxide supports (3). Additionally, 41 kcal/mole is in good agreement with the value calculated (4) based on literature data for a wide variety of carbonaceous materials including some delayed coker petroleum cokes. For comprehensive treatments of carbon combustion/ gasification kinetics, the reader is referred to several excellent reviews (5,6,7).

Figure 3 is an Arrhenius plot of the rate constant data for the fluid coke samples. Again, the data define a straight line, the slope of which yields an activation energy of ~27 kcal/mole. This value is in good agreement with ~30 kcal/mole found over a slightly lower temperature range for carbons doped with vanadium at levels roughly equivalent to that of the fluid coke (8). For comparison, Figure 4 shows Arrhenius plots for both delayed coker needle coke and fluid coke, as well as points obtained for sponge coke, which is a delayed coke with substantially larger metals content than the needle coke samples. The lines in Figure 4 converge at ~550°C, showing behavior very consistent with that found for pure and vanadium-doped carbon oxidation (8). This convergence indicates the increasing influence of the higher activation energy, thermal oxidation relative to the catalyzed oxidation reaction.

Figure 4 shows that fluid coke burns at a somewhat faster rate than delayed coker needle coke at temperatures below ~550°C. However, delayed coker sponge coke behaves in a manner similar to fluid coke. Both of these materials have high metals contents (Table I) relative to delayed coker needle coke, which exhibits lower rates and a higher activation energy. Thus, it is probable that petroleum cokes having higher metals concentration exhibit catalytically influenced combustion. In fact, such catalytic effects were reported (8) for carbons containing as little as 150 ppm vanadium, with little change in activation energy for vanadium concentrations up to 3.5%!

In summary, it appears that process origin does not have a major impact on the burning rates of "dry" petroleum cokes having similar initial surface areas and metals contents. The metals content of the coke can exert a catalytic influence on its burning rate. However, this effect is lessened at higher temperatures. Based upon these observations, it was inferred that any major differences between the combustibility of fluid coke and delayed coke under practical industrial conditions would likely be due to the presence of the heavy residual oils in the delayed coke. Volatilized residual oils would be more readily oxidized than the delayed coke itself and thus would aid in initiating and stabilizing the coke combustion process.

Enhancement of Coke Burning Rates by Separate Particle Catalysis

Effect of temperature Burning rate data for needle coke burned in the presence of clean sand and sand impregnated with metallic catalysts are presented in Figure 5. It is apparent that all the candidate catalytic materials investigated produced a burning rate enhancement. The apparent activation energy for coke burning in a 1% Pt/sand bed was ~17 kcal/mole versus ~41 kcal/mole for the baseline

(clean sand) data. The divergence of the two lines shows that the relative rate enhancement decreases with increasing temperature. When extrapolated, the two lines converge at a point corresponding to ~555°C, virtually identical to the point of convergence observed for the burning rate data presented in Figure 4 which showed the effect of metals intrinsic to the coke. This consistent finding suggests that a significant catalytic benefit of metals (whether intrinsic or present on separate particles) for burning rate enhancements may be realized only at temperatures below ~550°C. Furthermore, the data indicate that this effect is not highly sensitive to the identity of the metal.

Choosing 505°C as a comparison temperature, the data show that both 0.1% Pt and 1% Pt are equally effective, increasing the rate by a factor of 2.2. This behavior might be expected on such a low surface area support since more than enough Pt is present in both cases to cover the available surface. Also, nickel oxide is as effective as Pt in enhancing the burning rate, while cobalt oxide is only slightly inferior. Both Ni and Co have been previously reported as having catalytic activity for carbon gasification when directly impregnated on the solid fuel (9). As shown in Figure 5, sodium oxide is also quite effective as a catalyst. Alkali metal oxides have also been identified previously as effective gasification catalysts when impregnated on the fuel (10,11). However, they are believed to function by a different mechanism than noble or transition metals (12), some evidence of which is given below.

The data in Table II present the CO/CO_2 ratio in the combustion gases at 50% carbon burnoff. In all baseline cases with clean sand as the bed material, both CO and CO_2 were produced over the course of the burn in fairly fixed proportions, while in all Pt and transition metal experiments CO was never observed, indicating more efficient combustion. The similarity between the CO/CO_2 ratios of the baseline data and the sodium oxide data indicates that the alkali metal oxide enhances gasification of carbon to CO but does not effectively improve combustion efficiency by promoting complete conversion of CO to CO_2.

Figure 6 presents baseline and catalytic results obtained using sponge coke. Catalysis was again observed, but the 40% rate enhancements at 500-510°C are more modest than those observed with needle coke. The similar behavior of fresh and used Pt suggest that there is no rapid deterioration in performance. In contrast, fresh nickel oxide, which was initially as effective as Pt, rapidly lost its activity as shown by a decrease in burning rate and the appearance of CO in the combustion gases upon subsequent use. Though this suggests that the catalyst was being poisoned, presumably by coke-derived impurities, it is not clear why, under similar circumstances, the Pt activity remained unaffected. For comparison, Figure 7 shows baseline and 1% Pt/sand catalytic data for fluid coke. At ~505-510°C a moderate rate enhancement of ~50% was observed.

Based on the collective results shown in Figures 5-7, it may be concluded that no significant rate enhancement benefits are to be gained by separate particle catalysis in practical fluid bed combustors, which typically operate at temperatures >650°C. However, the results given in Table II show that separate particle catalysis can be beneficial in completing the conversion of CO to CO_2, resulting in higher combustion efficiencies and minimizing CO emissions from the unit. This benefit of lowered CO emissions, even

at the higher temperatures typical of practical fluid bed combustors, is not unexpected in light of the proven effectiveness of Pt CO combustion promoter additives used in the fluid bed, air regeneration of fluid cracking catalysts at temperatures >650°C (13).

Effect of intrinsic metals The higher rate increases observed with low-metals needle coke vs. sponge and fluid cokes parallel the relative burning rates discussed above in the absence of separate catalytic particles. Moreover, this behavior suggests that the extent to which a rate enhancement can be obtained with separate particle catalysts also depends upon the intrinsic metals content of the coke. To examine this point further, some additional data were obtained by burning toluene-derived soot (96% C, 2% O, 2% H) as a convenient model of a metals-free carbonaceous pyrolysis residue.

Although differing in "process" origin, both coke and soot are carbonaceous pyrolysis products having quite similar elemental analyses. Furthermore, both coke and soot have been shown elsewhere to have very similar reactivities and activation energies (~39 kcal/mole) with respect to combustion (4). In contrast, high purity graphite does not exhibit burning behavior similar to that of low-metals needle coke, as evidenced in related studies where the burning rate constant for ultra-high purity graphite (<5 ppm total impurities) was found to be over two orders of magnitude lower than that of the coke. This result is also consistent with earlier work which showed that high purity graphite has a reactivity ~3 orders of magnitude lower than coke and has a much higher activation energy (~50 to 70 kcal/mole) (4). This evidence shows that soot better models "high purity" petroleum coke burning behavior than do other carbonaceous residues such as ultra-high purity graphite.

Soot experiments were performed over clean sand, over 1% Pt/sand, and over clean sand with the soot directly impregnated with 1% Pt. These results are summarized in Table III. Despite its extremely fine particle size, in the absence of catalyst particles, the soot burning rate constant at 505°C was 6-7 times lower than that of low-metals needle coke. This factor seems reasonable in light of the soot's zero metals content and the discussions in the previous section.

In discussing the impact of added catalyst particles, the use of burning rate enhancements, i.e. relative burning rates with and without a catalyst, will facilitate comparisons among the various carbonaceous materials. Figure 8 shows the relative burning rates ($k_{catalyst}/k_{baseline}$) at ~505°C for soot and all the cokes investigated using 1% Pt on sand. The data point for needle coke is plotted somewhat arbitrarily at 30 ppm since the reported analytical results provided only upper bounds on the Ni and V contents (see Table I). The plot indicates that the extent of rate enhancement obtained by separate particle catalysis is a function of the intrinsic metals content of the solid fuel being burned. Therefore, above a certain threshold concentration of metal ($\sim$ 100 ppm Ni + V) intrinsic to the carbonaceous fuel, the otherwise large influence of external catalysts will be greatly diminished.

Pertinent to the question of intimacy between the metal and the solid fuel, a 17 fold increase in rate was obtained by separate particle catalysis of metals-free soot (Table III). In this case, soot was burned in a bed of Pt impregnated sand where the initial atomic Pt/C ratio was ~0.26/1. A 30 fold increase resulted, however,

when soot impregnated with 1 wt.% Pt was burned in a bed of clean sand where the initial atomic Pt/C ratio was 400 times lower. Clearly, the more intimate the contact between carbon and metal, the more effective the catalysis.

Mechanistic implications The fact that coke burning rate enhancements are observed when the bed material (sand) is impregnated with metals indicates that "solid-solid" catalytic interactions are occurring between the coke particles and bed particles in the presence of oxygen. Regardless of the particular metal or metal oxide particle, intimate contact between it and the carbon surface is required for the oxidation-reduction cycle of the metal particle to occur at the carbon surface, which is the generally accepted mechanism for the catalyzed oxidation of carbon (12). It is highly unlikely that gas phase transport of the metal or metal oxide to the carbon surface is involved under the current experimental conditions due to the low vapor pressures of these species at temperatures below 550°C.

The first step in any heterogeneous catalytic reaction is the transport of reactants from the bulk phase to the external surface of the catalyst. In the present work, only the external mass transfer step can influence and mask the intrinsic kinetics since the catalyst particles employed are non-porous and intraparticle diffusion is not a factor. If the external mass transfer step is rate controlling, then the observed apparent activation energy will be lower than that of the true activation energy of the catalyzed chemical reaction. This results because, compared to the reaction rate constant, the mass transfer coefficient is much less sensitive to changing temperature.

Standard methods exist for estimating the importance of external mass transfer gradients on the observed kinetic parameters (14). However, those procedures were developed for fluid phase reactants and, therefore, are not directly applicable to the case at hand where the reactants are macro-sized carbon particles. Nevertheless, the strong influence of convective transport of coke particles to the active external surface seems reasonable in light of the size of the solid reactants. Such an influence would explain the decline in apparent activation energy from ~27 kcal/mole for carbon particles containing a significant amount of intimate catalytic sites (fluid and sponge cokes) to ~17 kcal/mole where few such sites exist and transport of the carbon particle to external catalytic centers is required (needle coke). External mass transport rate control would also account for the apparent insensitivity of catalyst type on the extent of the rate enhancement observed for needle coke burning in the presence of external catalyst particles versus burning in the absence of an external catalyst.

CONCLUSIONS

The burning rates of "dry" petroleum cokes (i.e., cokes which are free of residual oil volatiles) having similar initial surface areas are not influenced by process origin (delayed vs. fluid coking). Differences in burning rate among the coke samples tested are related to the metals level in the coke which can exert a catalytic influence on the burning rate. This effect diminishes with increasing temperature as higher activation energy thermal reactions begin to dominate.

The addition of separate particles of low surface area catalytic solids can accelerate the combustion of petroleum coke and similar carbonaceous residues. The extent of the rate enhancement from an external catalyst declines with increasing temperature and increasing intrinsic metals content of the solid fuel. Moreover, these findings suggest that the primary benefit from separate particle catalysis in practical fluid bed combustors for steam generation would be enhanced conversion of CO to CO_2. Finally, the low activation energies observed are qualitatively consistent with a rate-limiting step involving transport of coke particles to the surface of the catalyst particles.

ACKNOWLEDGEMENTS

The technical assistance of Messrs. D. B. Steel and L. R. Koenig and Ms. B. A. Paquin are gratefully acknowledged in the construction of the apparatus and execution of the experiments. Helpful discussions with Drs. H. J. Schoennagel and J. Wei are also appreciated.

REFERENCES

1. Juntgen, H. (1983). Application of catalysts to coal gasification processes: incentives and perspectives. Fuel 62, 234.
2. Tyler, R. J. (1986). Intrinsic reactivity of petroleum coke to oxygen. Fuel 65, 235.
3. Weisz, P. B. and Goodwin, R. D. (1966). Combustion of carbonaceous deposits within porous catalyst particles. II. Intrinsic burning rate. J. Cat. 6, 227.
4. Smith, I. W. (1978). The intrinsic reactivity of carbons to oxygen. Fuel 57, 409.
5. Walker, Jr., P. L., Rusinko, Jr., F., and Austin, L. G. (1959). Gas reactions of carbon. Advances in Catalysis 11, 133.
6. Laurendaen, N. M. (1978). Heterogeneous kinetics of coal char gasification and combustion. Progress in Energy and Combustion Science 14 (4), 221.
7. Mulcahy, M. F. R. and Smith, I. W. (1969). Kinetics of combustion of pulverized fuels: a review of theory and experiment. Reviews of Pure and Applied Chemistry 19, 81.
8. Buch, T., Guala, J. A., and Caneiro, A. (1978). Oxyreactivity of doped sucrose carbon. Carbon 16, 377.
9. Marsh, H. and Adair, R. R. (1975). Catalytic gasification of doped carbon - a kinetic study. Carbon 13, 327.
10. McKee, D. W., Spiro, C. L., Kosky, P. G., and Lamby, E. J (1983). Catalysis of coal char gasification by alkali metal salts. Fuel 62, 217.
11. McKee, D. W. (1980). Mechanisms of catalyzed gasification of carbon. General Electric Corporate Research and Development Report No. 80CRD143.
12. McKee, D. W. (1981). The catalyzed gasification reactions of carbon. In Walker, Jr., P. L., and Thrower, P. A. (Ed.), Chemistry and Physics of Carbon, Marcel Dekker, New York, Vol. 16, pp. 1-118.
13. Chester, A. W., Schwartz, A. B., Stover, W. A., and McWilliams, J. P. (1981). Catalyzing the energy balance of "cat" cracking. Chemtech 11, 50.
14. Hougen, O. A. (1961). Engineering aspects of solid catalyst. Industrial and Engineering Chemistry 53 (7), 509.

TABLE I

COKE ANALYSES

	Needle Coke+	Sponge Coke+	Fluid Coke*
C (wt%)	93.8	90.4	87.3
H	2.4	1.7	1.6
O	2.3	1.7	1.6
N	0.48	1.1	1.2
S	0.54	3.68	8.0
Ash	0.53	1.17	.33
Ni (ppm)	<20	145	275
V	<25	390	540
Cu	5	7	5
Fe	200	215	60
Surface Area, m^2/g	8	6	8

+ N_2 Calcined to 650°C, air burned at 650°C, ~90 sec, ~1hr. N_2 calcination at 600°C.

* ~1 hr. N_2 calcination at 600°C.

TABLE II

CO/CO_2 RATIO AT 50% NEEDLE COKE BURN-OFF (505°C)

Catalyst	CO/CO_2
None	0.64
.1% Pt	0
1% Pt	0
1% NiO	0
1% CoO	0
1% NaO	0.67

TABLE III

INFLUENCE OF Pt ON TOLUENE SOOT BURNING RATE AT 505°C

	$k\ (min^{-1})$	k_{Pt}/k_{base}
Base case (no catalyst)	0.015	1.0
1 wt% Pt on Sand	0.260	17.3
1 wt% Pt on Soot	0.452	30.1

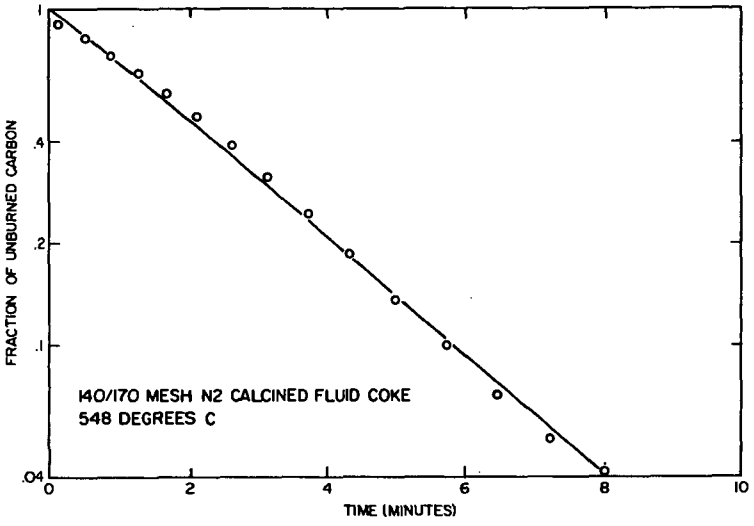

FIGURE 1. FRACTION OF UNBURNED CARBON VS. TIME

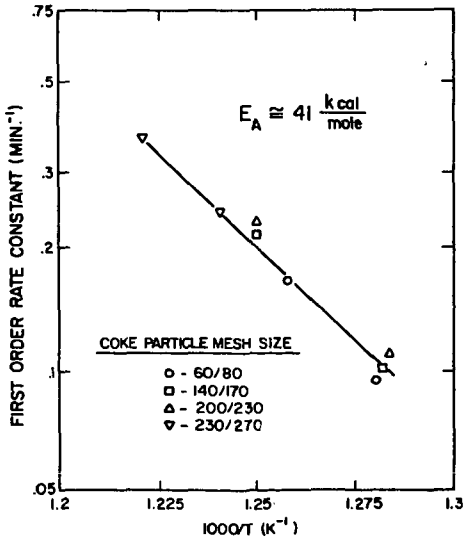

Figure 2. ARRHENIUS PLOT FOR NEEDLE COKE COMBUSTION

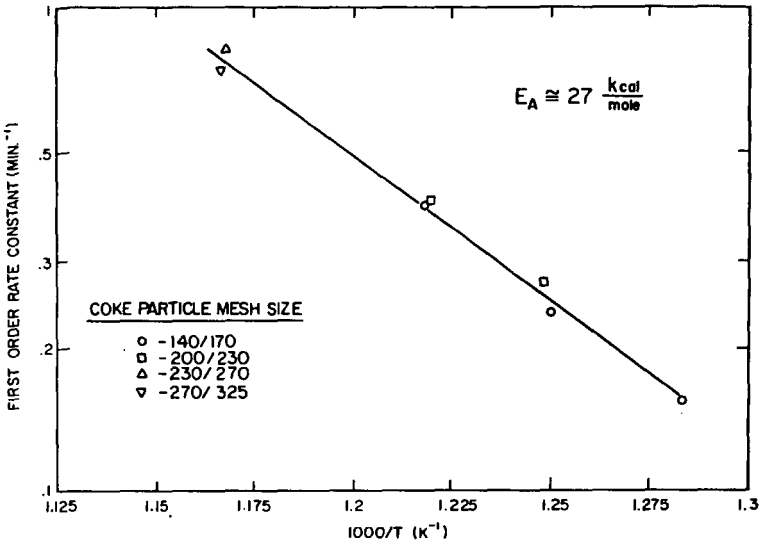

Figure 3. ARRHENIUS PLOT FOR FLUID COKE COMBUSTION

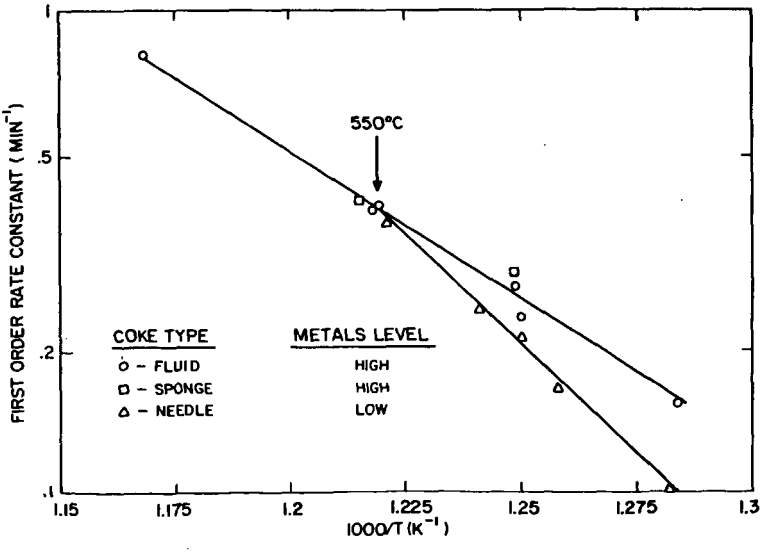

Figure 4. INFLUENCE OF COKE METALS CONTENT ON ARRHENIUS BEHAVIOR

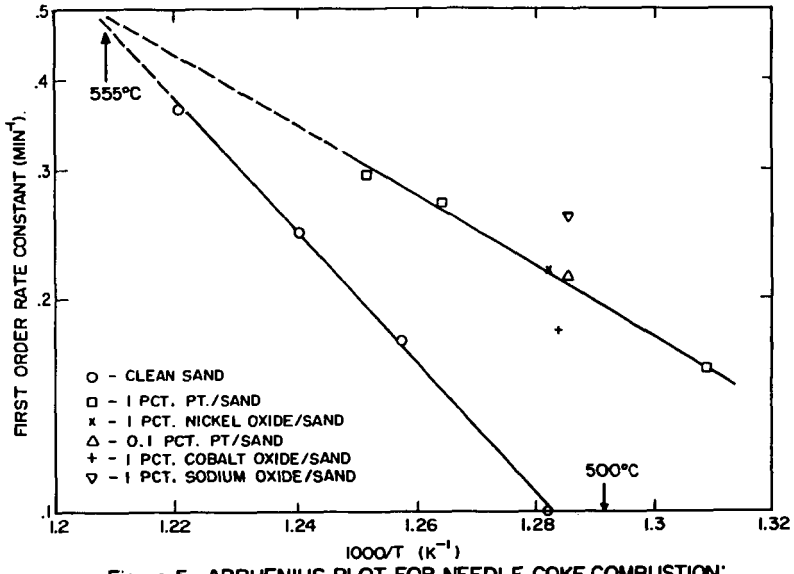

Figure 5. ARRHENIUS PLOT FOR NEEDLE COKE COMBUSTION: EFFECT OF SEPARATE PARTICLE CATALYSIS

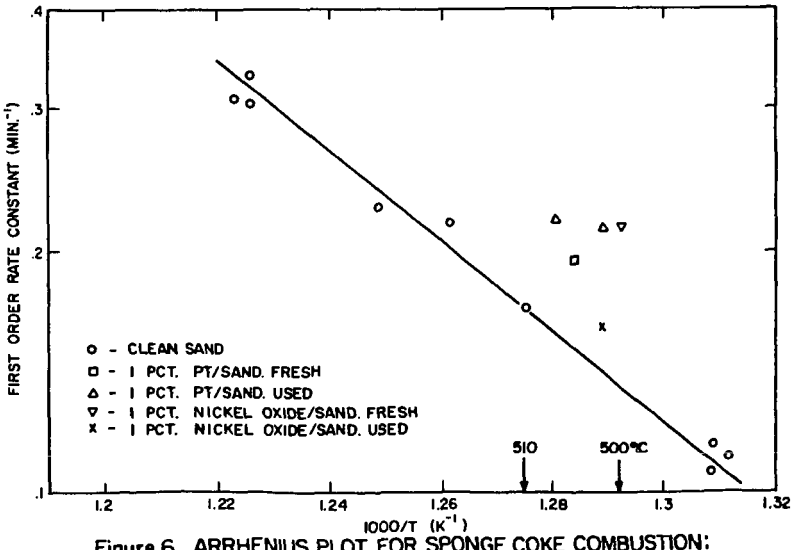

Figure 6. ARRHENIUS PLOT FOR SPONGE COKE COMBUSTION: EFFECT OF SEPARATE PARTICLE CATALYSIS

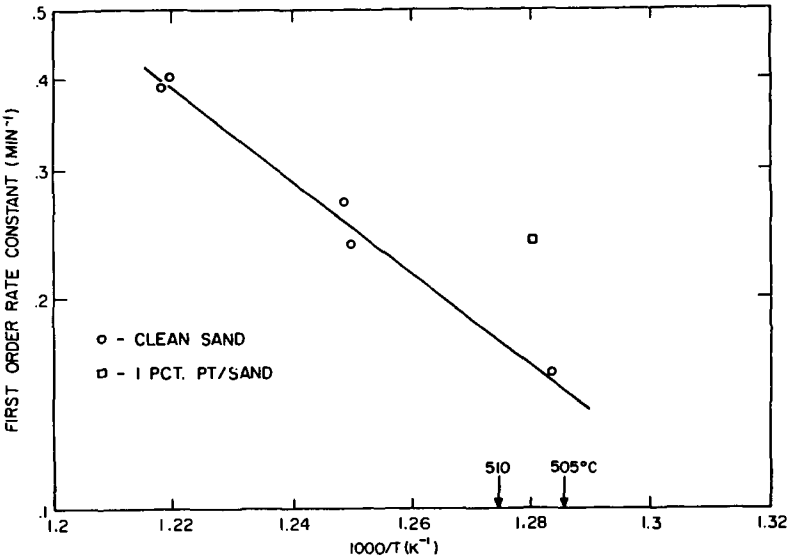

Figure 7. ARRHENIUS PLOT FOR FLUID COKE COMBUSTION: EFFECT OF SEPARATE PARTICLE CATALYSIS

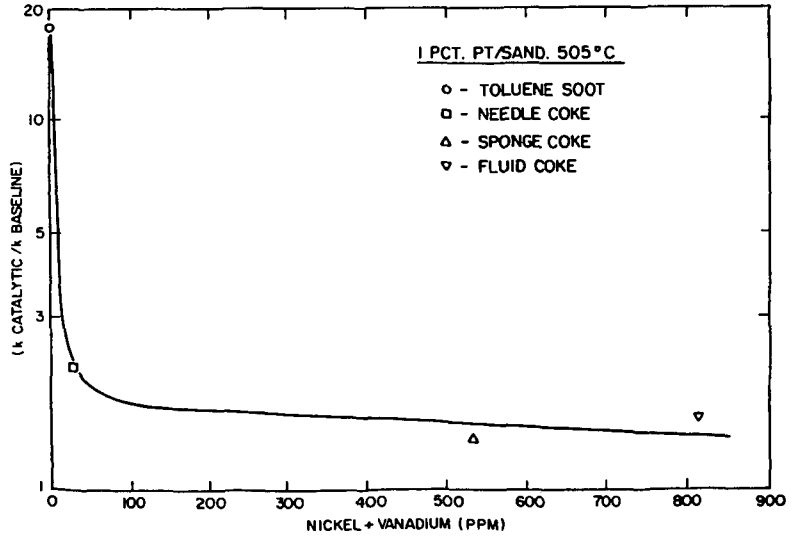

Figure 8. RATE CONSTANT RATIO VS. INTRINSIC METALS CONTENT

THE PREDICTION OF SLAGGING PROBLEMS AS A RESULT OF COAL BLENDING

Edward J. Zecchini and Gary L. Foutch

School of Chemical Engineering
Oklahoma State University
Stillwater, Oklahoma 74078-0537

INTRODUCTION

Power generating facilities which use coal face several problems caused by the nature of the fuel. Of these problems, fireside fouling and deposition is of major importance. Fireside deposition affects boiler availability and operating efficiency. Determination of when a coal or blend of coals will cause significant slagging problems is extremely important. The properties and mechanisms behind fireside deposition due to coal blending is the focus here (1).

Such a problem occurred at the Public Service Company of Oklahoma's (PSO's) northeast generating facility. The problem arose when two Wyoming, subbituminous coals were blended. These two coals, Jacob's Ranch (JR) and Clovis Point (CP) cause only moderate fireside deposition when burned separately. Any blend of the two coals causes more boiler deposition and fouling than either pure coal, based on observations by PSO's engineers (2). The blend which results in the most severe fireside deposition is approximately 75% JR-25% CP. Although avoiding blending eliminates this problem, in some circumstances operating conditions require the use of blended coals.

When blending coals, care must be taken to determine if the two (or more) coals are compatible. Lee and Whaley (3) examined the modification of combustion and fly-ash characteristics due to the blending of coals. They concluded that potential operational problems due to the blending can be minimized or avoided by careful determination of coal and coal ash properties before usage. Dooley and Chacinski (4) agreed on not using empirical slagging correlations to predict blended coal slagging propensities. To further support this, a number of the standard slagging indices (5) have been evaluated with the available data on Jacob's Ranch and Clovis Point coals. As Table I summarizes, none of the standard indices describe the problem as observed by PSO's engineers.

As a result, a new approach seems to be necessary. A possible approach, and the one used in this study, is one analogous to reaction order theory.

EXPERIMENTAL DATA

There is certain data that is necessary in evaluating the predictive method to be employed in this study. A proximate analysis of both coals (Jacob's Ranch and Clovis Point) is given in Table II (6). The data that will be of most interest in the approach used here are the coal ash compositions. There are two different sets of coal ash composition data, one is an independent analysis conducted by Williams Brothers Laboratory (6), the other is the analysis at OSU. This data is presented in Table III. The analysis of the ash from different blends of the two coals is presented in Table IV.

GENERAL APPROACH

The approach selected to predict the observed problem is similar to reaction rate theory. If one coal is rich in component A and the other coal is rich in component B, then a reaction analogy applies. An interaction between two components is modeled as if it were a reaction with a rate equation given by: $aA + bB \rightarrow$ Products (reaction or interaction); Rate $\alpha [A]^n [B]^m$ (rate expression). Where n and m are exponents on the concentrations of reactants A and B, respectively. The order of the interaction is given by n + m. There are certain unknowns here that need to be selected or determined by trial and error.

DISCUSSION

The general description of the deposition problem leads immediately to a conceptual form of the desired slagging correlation (Figure 1). The problem is how to predict such a dramatic change in the slagging properties of the coal burned as the %Jacob's Ranch in the blend changes with the numerous variables that are as of yet undefined. The most pressing problem is the selection of the data to be used as concentrations. Finding actual concentrations in such a situation is impossible, so some means of finding relative or pseudo concentrations is necessary. The weight percents of oxides in the ash represent relative concentrations. Using these values as the concentrations in the rate equation resolves two of the unknowns. The problem of interaction order needs to be addressed, since it has been shown that overall first order involving either sodium or iron (historically the most important elements in slagging) has not been successful. An overall second order has been selected for application in this study. The most reasonable values for n and m in this scheme are one. The final problem is in determining A and B, the coal and coal ash constituents. The selection of A and B is not obvious and will be determined via trial and error with those resulting in the desired profile considered further. The interactions will be plotted as a function of the percent Jacob's Ranch in the blend. Where available the actual blend data points will also be included on the graph to compare the predicted value with the actual data.

There is more than one basis to calculate these interactions. The first and simplest is to assume that the relative amounts of ash contributed by each coal are the same. This means that the interaction is just the product of the values determined for the percentages of the oxides in the ash. A more realistic approach is to employ an ash correction factor to account for the two coals have differing ash contents. This correction factor is based on equal weights of the coals (or blends) being burned. A further correction may be used to account for differing heating values for the coals to produce the same heat output. A linear relationship between the pure coal heating values for the heating values of blends has been used. The actual effect of this correction factor will be to shift the curve towards the Clovis Point axis (0% JR).

Those curves with the desired profile are shown in Figures 2 through 5. Table V summarizes the interactions that showed the desired profile for any one of the above methods. Those interactions that are of most interest involve sodium or iron. These elements have been considered most influential in the formation of fireside deposits. Hence, these interactions support work done with pure coals.

CONCLUSIONS

This work is preliminary and involves only the two coals used at PSO where the blending problem was observed. Further work in this area is clearly necessary. However, the results clearly indicate that an overall second order reaction analogy can show an optimum as a function of coal blend which previous slagging prediction methods could not do. Efforts are continuing to evaluate interaction for other blending problems in hopes of obtaining a correlation which will be predictive for any coal blend.

REFERENCES

1. Zecchini, E. J., Masters Thesis, Oklahoma State University, 1986.

2. Lehman, D., "Slagging Experiences while Blending Wyoming Coal," Internal Report, Public Service Company of Oklahoma, Northeast Station, Oologah, Oklahoma, 1983.

3. Lee, G. K. and H. Whaley, Journal of the Institute of Fuel, 190, 1983.

4. Dooley, R. B. and V. Chacinski, Proceeding of the American Power Conference, 43, 106, 1981.

5. Raask, E., Mineral Impurities in Coal Combustion, Hemisphere Publishing Corp., New York, 1985.

6. Personal Communication from Williams Brothers Laboratory, Analysis of Jacob's Ranch and Clovis Point Coals, 1984.

TABLE I
STANDARD SLAGGING CORRELATION SUMMARY

	Williams Brother Data			This Study HTA Data		
Index	JR	Blends	CP	JR	Blends	CP
Silica Ratio	MS	MS	MS	HS	HS	HS
$\%Na_2O$	MS	MS/HS	HS	MS	MS/HS	HS
$\%Fe_2O_3$	LS	LS	LS	LS	LS	LS
Na Equivalent	LS	LS	LS	LS	LS	LS
R_b/a	LS	LS	LS	SS	SS	SS
Fy	MS	MS	MS	MS	HS	HS
Fs'	LS	LS	LS	LS	LS	LS

ND = Not Determined
LS = Low Slagging
MS = Medium Slagging
HS = High Slagging
SS = Severe Slagging

TABLE II
PROXIMATE ANALYSIS OF PURE COALS

Jacob's Ranch			
Analysis (wt%)	As Received	Moisture Free	Moisture and Ash Free
Moisture	25.44	****	****
Vol Matter	36.55	49.02	53.95
Ash	6.81	9.13	****
Fixed Carbon	31.70	41.85	46.05
H.H.V. Btu/lb	8,863	11,886	13,081
Clovis Point			
Analysis (wt%)	As Received	Moisture Free	Moisture and Ash Free
Moisture	31.32	****	****
Vol. Matter	33.85	49.28	54.11
Ash	6.14	8.94	****
Fixed Carbon	28.69	41.78	45.89
H.H.V. Btu/lb	8,014	11,668	12,813

Data from Williams Brothers Laboratories

TABLE III
JACOB'S RANCH ASH ANALYSIS

Component	Williams Brothers	This Study HTA
Iron as % Fe_2O_3	7.15	5.93
Calcium as % CaO	14.22	19.43
Magnesium as % MgO	3.15	4.75
Sodium as % Na_2O	0.68	0.76
Potassium as % K_2O	1.37	0.33
Silicon as % SiO_2	46.38	45.45†
Aluminum as % Al_2O_3	13.81	15.04
Titanium as % TiO_2	1.15	N.D.
Phosphorus as % P_2O_5	1.11	N.D.
Sulfur as % SO_3	6.05	N.D.
% Ash in the Coal	6.81	6.40

N.D. = Not Determined
† = By Difference

TABLE III
(Continued)

Clovis Point Ash Analysis

Component	Williams Brothers	This Study HTA
Iron as % Fe_2O_3	4.29	3.94
Calcium as % CaO	14.64	21.93
Magnesium as % MgO	3.12	5.58
Sodium as % Na_2O	1.08	1.66
Potassium as % K_2O	1.45	0.10
Silicon as % SiO_2	50.24	44.71†
Aluminum as % Al_2O_3	13.55	15.04
Titanium as % TiO_2	0.95	N.D.
Phosphorus as % P_2O_5	1.56	N.D.
Sulfur as % SO_3	4.53	N.D.
% Ash in the Coal	6.14	7.0

N.D. = Not Determined
* = Negligible
† = By Difference

TABLE IV
ASH COMPOSITION OF SELECTED BLENDS

a) High Temperature Ash (HTA)

Component	100%JR	75%JR-25%CP	50%JR-50%CP	25%JR-75%CP	100%CP
Fe_2O_3	5.93	4.72	4.49	3.94	3.94
CaO	19.43	20.14	20.62	21.15	21.93
MgO	4.75	5.15	5.25	5.35	5.58
Na_2O	0.76	1.04	1.18	1.44	1.66
K_2O	0.33	0.27	0.22	0.16	0.10
SiO_2	45.45†	46.21†	45.52†	45.40†	44.71†
Al_2O_3	15.04	14.76	15.04	15.04	15.04
TiO_2	N.D.	N.D.	N.D.	N.D.	N.D.
P_2O_5	N.D.	N.D.	N.D.	N.D.	N.D.
SO_3	N.D.	N.D.	N.D.	N.D.	N.D.

* = Negligible
† = By Difference

TABLE V
POSSIBLE INTERACTIONS FOR SLAGGING PREDICTION

	Interaction Williams Brothers Data			This Study HTA		
	Uncorr.	Ash Corr.	Heat Corr.	Uncorr.	Ash Corr.	Heat Corr.
Na * Fe	DP	DP	DP	NP	NP	NP
Na * K	NP	NP	NP	DP	DP	DP
Fe * P	NP	NP	NP	DP	UP	UP
Na * S_{coal}	NP	DP	NP	NP	NP	NP
Na * S_{ash}	NP	UP	NP	NP	ND	NP

NP = No Peak
DP = Desired Profile
UP = Undesired Profile

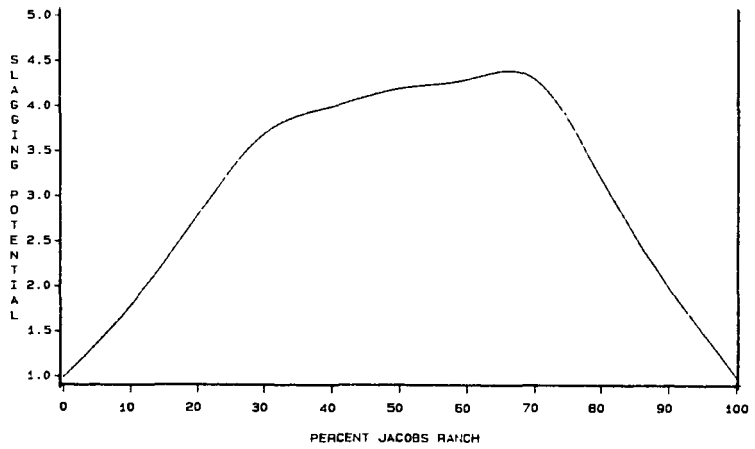

Figure 1. Desired Slagging Index Profile as a Function of Blend

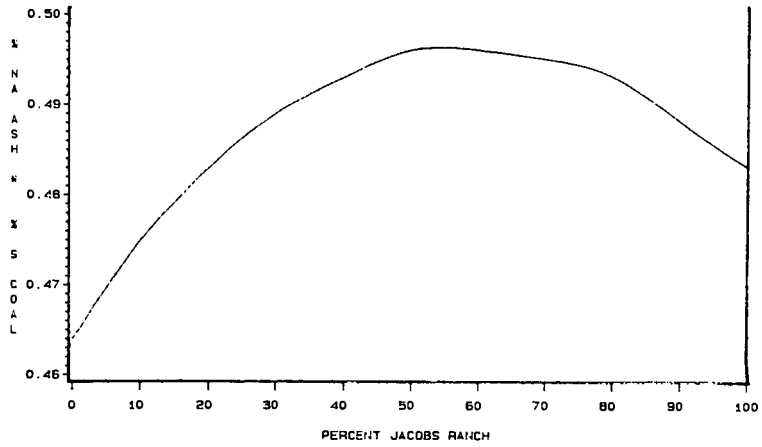

Figure 4. Ash Corr. 2nd Order Interaction of Na and S(coal)
(Williams Brothers Data)

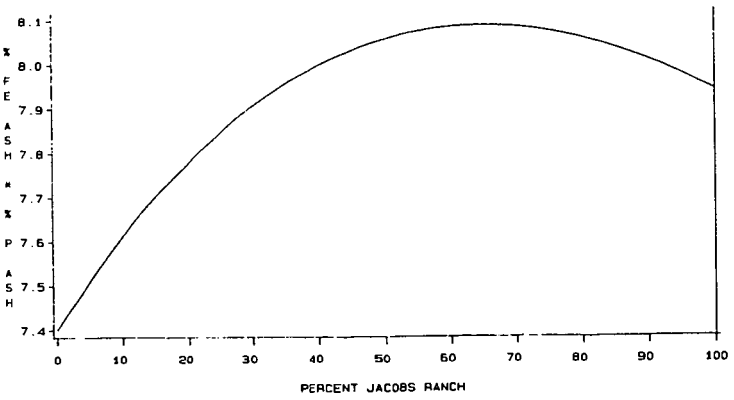

Figure 5. Heat Corrected 2nd Order Interaction of Fe and P
(Williams Brothers Data)

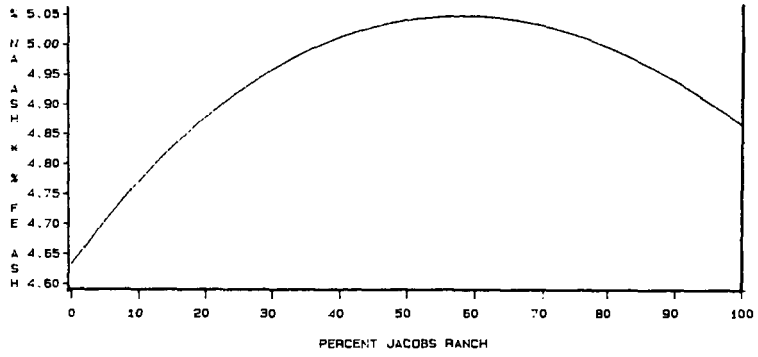

Figure 2. Uncorrected 2nd Order Interaction of Na and Fe
(Williams Brothers Data)

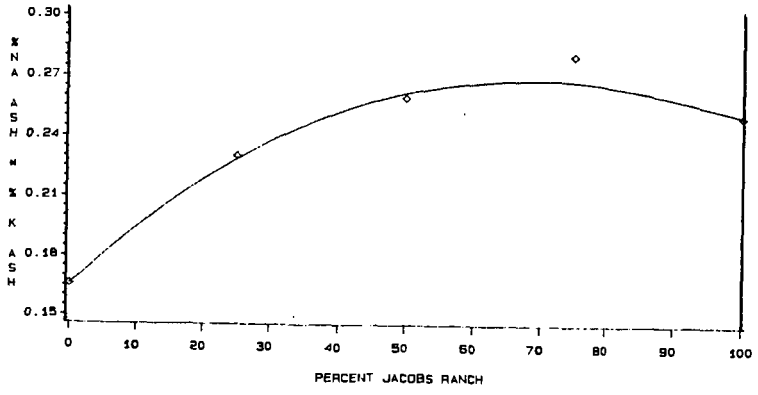

Solid line= This Study Predicted
Diamond= This Study Actual Data

Figure 3. Uncorrected 2nd Order Interaction of Na and K

THE EFFECT OF SODIUM ON DEPOSITION IN A SIMULATED COMBUSTION GAS TURBINE ENVIRONMENT

Jeffrey S. Ross and Rodney J. Anderson
U.S. Department of Energy
Morgantown Energy Technology Center
Morgantown, West Virginia 26505

Ramamurthy Nagarajan
Department of Mechanical Engineering
West Virginia University
Morgantown, West Virginia 26506

ABSTRACT

The effect of gas phase alkali concentration on the adhesion properties of micronized coal has been studied using a laboratory-scale entrained reactor capable of accelerating the combustion products of an injected coal-air mixture to the velocities observed in a combustion gas turbine. Alkali metal sulfates are reputed to act as liquid "glue" binders which promote inorganic deposit formation under these conditions. In this study, the concentration of alkali was varied by utilizing a series of naturally occurring coals (Arkwright Pittsburgh bituminous, Spring Creek Montana subbituminous, and North Dakota lignite), and by doping Arkwright coal samples with sodium benzoate. Measured sticking coefficients (i.e., the mass fraction of incident ash which sticks to a deposition target) obtained from this series exhibited trends consistent with the glue hypothesis and with the amount of liquid phase sodium sulfate predicted by equilibrium thermodynamic and vapor deposition rate calculations. Thus, between the melting point and dew point of sodium sulfate, higher sodium concentrations in the coal feed resulted in enhanced sticking. Below the sulfate melting point, the sodium concentration had no effect. These measurements provide a confirmation of the glue-like behavior of sodium sulfate in enhancing deposition rates and represent the first successful probing of the effect of an individual element upon the properties of fly ash originating from natural and chemically doped fuels under gas turbine combustor temperature and velocity conditions.

INTRODUCTION

One purpose of the U.S. Department of Energy's Fossil Energy Program is the development of technology for use of fossil fuels in the production of energy for domestic consumption. As a part of that program, the Morgantown Energy Technology Center has initiated a program to examine deposition effects in coal-fired heat engines, with the final objective being the development of techniques to mitigate the deposition problem in direct coal-fired gas turbines. This paper reports results from an effort, as a part of that program, to sepa-

rate the deposition problem from erosion and corrosion and to identify the relationship between deposition and the various chemical constituents in coal.

The use of coal and coal-derived fuels in direct-fired gas turbines provides an attractive alternative to other fuel sources such as petroleum or natural gas. Advantages of coal-based direct-fired turbine systems are the increase in efficiency provided when steam vaporization is removed from the energy production cycle, low capital costs for construction of moderate capacity systems, and a readily available inexpensive fuel. Limitations to the use of coal include dry handling costs and the large fraction of non-combustible material occluded within the coal matrix. Impurities can damage turbine components by a combination of erosion, corrosion, and deposition. These three complications can result in increased maintenance costs and/or losses in cycle efficiency due to either deposit buildup on the airfoils or the imposition of filtration equipment to prevent the problems. The effect of dry handling on the use of coal derives from two sources. First, the technology of dry fuel is considerably different from that of liquid feeding processes. Thus, power plants equipped for diesel or petroleum are not equipped to utilize coal, except perhaps as a coal-water mixture (CWM). However, the formulation of a CWM requires significant grinding of the coal and represents an added expense. Also, the problems of erosion, corrosion, and deposition all require grinding and/or beneficiation of the coal in order to meet gas turbine particulate operating specifications. If these problems can be solved, coal-based plants based on gas turbines can have a distinct competitive price relative to alternatives such as oil, natural gas, or petroleum.

The context of the present study derives from the observation that deposit growth may be promoted by the presence or formation of a liquid layer on the surfaces of ash particles (1,2,3,4). The liquid layer may consist of sodium (or other alkali) sulfate(s) which, due to rapid cooling arising from the expansion out of a gas turbine nozzle, can condense on the surface of an ash particle or on a component surface (rotor or stator blade). The condensation mechanism may be either heterogeneous as observed by Liang, et al. (5), in a recent binary nucleation study or homogeneous as suggested by the calculations of Ahluwalia, et al. (6). Regardless of the mechanism of deposition, experimental determinations of the elemental composition of ash particles have confirmed that surface enrichment does occur on the outer surfaces of fly ash particles (7). In fact, such observations have led to the suggestion that the injection of small particles into combustion turbines could have a mitigating effect on liquid-assisted deposition by acting as sodium gettering sorbents (8).

This set of observations has led to our determination of the "sticking coefficients" of a variety of coals under a wide range of conditions. Portions of this work have appeared as preliminary communications in which the qualitative effects of target temperature, reactor temperature, particle velocity, and coal composition have been discussed (9,10,11). We have now merged our previous deposition results with new observations made on sodium-doped coals and, in an effort to rationalize our observations and predict the sticking behavior of other coals, present those observations within the framework of a preliminary theory of molten glue-assisted deposition (12).

EXPERIMENTAL

The deposition tests were performed in a laboratory-scale entrained reactor (LETR) which consisted of a mass flow controlled air flow circuit, a particle injection system, a high-temperature furnace, a deposition target assembly, a filtration assembly, and a set of temperature and pressure diagnostics interfaced to a personal computer (Figure 1). The system attempts to simulate deposition processes at the leading edge of a gas turbine. To accomplish this, coal particles are entrained from a fluidized bed feeder and transported into the combustion zone (muffle tube H [Figure 1]) of the LETR. Combustion of the coal leaves the occluded inorganic material entrained as "ash" particles in the hot gas stream. These particles are, in turn, accelerated through a pinhole nozzle located at the end of the muffle tube to velocities in excess of 100 m/s. The degree of acceleration depends upon the temperature of the gas, the pressure drop across the nozzle, and the nozzle diameter. The high velocity particles then impinge upon a platinum target placed normal to the downflow of the gas-particle mixture. Target temperature is measured by radiation pyrometry. The sticking coefficient of the particular sample is obtained as the fraction of ash impinging on the target that actually adheres to the target. A detailed description of the LETR and the typical operating procedure are given below.

Particle Injection System

The particle injection system consisted of a TSI Model 3400 fluidized-bed aerosol generator (FBAG), a source of dry mass flow controlled compressed air, and a sample splitter, also mass flow controlled, in series with a vacuum pump. Prior to an experiment, the sample compartment of a TSI Model 3400 fluidized-bed aerosol generator was charged with about 10 grams of coal. All coal samples were ground to below -400 mesh (< 40 microns) to facilitate entrainment by the carrier gas. A small motorized conveyor transferred the coal particles into a 1.5-inch diameter bed that was filled with 100 grams of clean copper beads, which served to break up coal agglomerates. A dry air stream was used as both the fluidizing gas and the entrainment gas. The volumetric flow rate of the gas was mass flow controlled at 14 liters per minute, with 80 percent of the flow directed through the bed and the remainder used to purge the particle conveyor. A mass flow controlled aspirator near the entrance of the furnace served to limit the total flow of particle-laden gas to the reactor to below 5.0 liters per minute. The remainder of the gas was exhausted through a filtration system. This throttling was required to hold the nozzle pressure drop within safe limits.

Furnace Assembly

The furnace was an Astro Industries Model 1000 vertical graphite element tube furnace equipped with a helium purge gas system and an alumina muffle tube assembly. An alumina nozzle (25 mm length, 0.127 mm diameter) was cemented into the muffle tube so that the nozzle exit was 2.5 inches from the exit of the muffle tube. The temperature of the muffle tube was estimated with the aid of two thermocouples, one of which was held in contact with the muffle tube, while the other monitored the temperature adjacent to the heating element. Heating of the tube was accomplished by radiation and conduction through the helium purge gas, which also prevented oxidation of the graphite elements. A set of profiles of the temperature at the center line of the muffle tube (Curves a-c [Figure 2]) obtained with no acceleration nozzle in place were consistent with laminar flow through the furnace.

Deposition Target Assembly

The platinum target disks (0.25 mm thick, 5 mm diameter) were supported on an Inconel pedestal (Figure 3) bolted to the bottom of the furnace assembly. Pedestal height was adjusted by a series of stainless steel shims in order to position the target at approximately one nozzle diameter (1.27 mm) from the nozzle exit. The pedestal was hollow and contained a quartz lens which focused infrared light emitted from the target onto the entrance of a bifurcated fiber optic bundle. The two legs of the fiber bundle were directed to optical filters with wavelengths of 902.5 nm (14 nm bandwidth) and 1,039.5 nm (19 nm bandwidth), respectively. The transmitted signals were detected by photodiodes, amplified, and output as millivolt signals to an Apple computer. This permitted determination of the target temperature by radiation pyrometry. The targets were weighed to within +/-3 micrograms before and after a deposition run and the deposit weight determined by difference. Deposit weights were typically in the range of 20 to 100 micrograms.

Filtration Assembly

The arrival rates of ash particles at the target surface were estimated by replacing the target with a filtration assembly fabricated from a combination of a Gelman stainless steel filter holder and a 4-inch porous alumina cylinder. An air flow of 2.0 liters per minute through the porous cylinder provided a radial pressure which prevented deposition of ash vapor and/or particles except on a silver membrane filter (Osmonics, Inc.) held in place by the filter holder. A vacuum pump downstream from the filter was used to balance (via mass flow control) the sampling rate through the filter with the gas input from the furnace exit and the filter inlet. The balance was required in order to prevent escape of particles from the filter and to prevent thermal shock to the muffle tube due to aspiration of room temperature air. In a typical deposition run, three to five filter samples were obtained and used to establish an average ash arrival rate (10 to 80 micrograms per minute, depending on the settings of the particle injection system).

Preparation of Sodium-Doped Coals

A known amount of sodium benzoate (Fischer Scientific) was dissolved in excess (> 150 mL) of HPLC grade methanol (J. C. Baker) and the clear solution added to a round-bottomed flask containing 10 grams of Arkwright Pittsburgh bituminous coal. The methanol was then removed using a rotary evaporator. The ground glass joints of the evaporator were ungreased to avoid contamination of the coal with silicon. The product consisted of a grayish-black powder with some small whitish lumps of (presumably) pure sodium benzoate occluded within the coal matrix. This material was then ground to pass a 400 mesh screen.

Typical Deposition Procedure

The coal sample of interest was loaded into the FBAG and the entrainment gas flow and aspiration rates adjusted such that the pressure drop across the acceleration nozzle in the muffle tube was within safe limits and was providing a gas stream of high velocity. During this process, the coal particles were removed from the gas flowing to the reactor by an absolute filter (close Valve 1, open Valves 2 and 5 [Figure 1]) to prevent contamination of the cold furnace. After the muffle tube (heated at a rate of 200°C per hour) and the

deposition target reached their appropriate test temperatures, the filter was removed from the flow path (open Valve 1, close Valves 2 and 5 [Figure 1]) and the particle-laden flow was directed into the muffle tube. After collection of several samples, the filtration assembly was removed and the absolute filter reinserted into the particle flow stream. The target assembly was then affixed to the furnace and the target allowed to reach thermal equilibrium in the absence of particles. Blank runs were performed and indicated that deposition ceased when the absolute filter was in the flow path. The absolute filter was then removed from the flow path and the deposition process allowed to proceed for about 1 hour, after which the target was isolated from particles, the target assembly removed, and the target weighed.

Data Acquisition

Furnace temperature, target temperature, reactor coolant temperature, and nozzle pressure drop measurements were recorded continually during each test by an appropriate interface to a personal computer. For high-speed measurements of the nozzle pressure drop (which determines the nozzle exit particle/gas velocities) and of the target temperature, an IBM PC-AT was employed as a data acquisition device. The IBM interface hardware included a Data Translation DT2805 12 bit A/D board and a DT2807 interface board. Data was acquired by means of a FORTRAN program which employed subroutines from PCLAB and Wiley's FORTRAN Scientific Subroutines, and Fifty More FORTRAN Scientific Subroutines.

RESULTS AND DISCUSSION

This combined experimental and theoretical report deals only with the effects of deposition in direct-fired coal-burning systems and, therefore, it is appropriate to first outline the justifications for neglecting or removing other effects during the subject experiments (e.g., erosion and corrosion). Also appropriate is a brief discussion of the chosen target design and its relationship to deposition phenomena.

Industrial combustion turbine research has shown that if the gas stream particle size is kept below 10 microns, then deposition and corrosion, not erosion, are the effects responsible for limiting the useful lifetime of a gas turbine (13). This observation was used to decouple erosion from LETR experiments; only micronized coal samples (< 400 mesh) were used. An added benefit of micronized coal is that the particles are easily entrained and when moving through the apparatus, they follow the flow paths of the gas (i.e., they have a negligible inertial slip velocity). This helps to eliminate deposition of slag within the reactor which could develop in a drop tube by overloading of the combustion zone. Some of the detrimental effects of slagging in a test reactor are changing combustion heat transfer properties, a buildup of liquid/glass phase species of unknown vapor pressure that could contaminate future samples, and variation within sample runs of the equilibrium vapor pressures of slag components. By employing the entrainment principle, the combustion zone loading is sufficiently low to avoid slagging.

The decoupling of corrosion from LETR experiments was accomplished by fabricating the targets from platinum metal. This is justified by the inertness of platinum toward oxidation, poor affinity for adsorption of gases such as carbon monoxide and carbon dioxide, and resistance to attack by hot corrosive liquids (14,15,16). An important qualification which has not been

addressed is the utility of deposition data in absence of the competing effects of erosion and corrosion.

Conversely, after combustion of the coal particles, it is desirable to force as much of the ash as possible to impact upon the target. The use of a target placed normal to the gas stream at the nozzle exit satisfies this condition if the target diameter is much larger than the nozzle diameter and if the target is located less than five nozzle diameters from the nozzle exit (17). This design was employed in the LETR and imposed the requirement of zero velocity (both particle and gas) at the target surface. The overall result is that a stagnation point has been created at the intersection of the target and the expanding gas-particle jet. The significance of this is that particle arrival rates and vapor deposition rates are at or near their maximum values under stagnation conditions which should result in the observation of the maximum effect of an additive upon coal ash deposition properties. Finally, the leading edge of a gas turbine blade also has a stagnation line configuration.

Deposition data was obtained for the following coals: Arkwright Pittsburgh bituminous (APB), Spring Creek Montana subbituminous (SCMS), AMAX-II (cleaned) Kentucky bituminous (KB), North Dakota lignite (NDL), and acid-washed North Dakota lignite (AWL). The ultimate analyses for these coals are presented in Table 1. Figure 4 shows a plot of the "sticking coefficient" (mass fraction of material adhering to the target) obtained for these coals at a variety of target temperatures.† These data are reproducible to within about ± 20 percent. Although NDL has the highest ash content and the highest sticking coefficient, the correspondence between ash content and sticking coefficient does not continue for the other coals. Similarly, although increased sodium content may increase the fouling tendencies of coal, a simple (i.e., linear) correspondence between sodium and sticking coefficient does not appear to be operative here. Furthermore, the ordering of the sticking coefficients is not explained by simple parametric indices such as the fouling index (10,18). Thus, although the extreme cases agree with predictions based on coal ash content, alkali level, or fouling index, a more detailed description of coal ash sticking must be employed in any rational analysis of ash deposition.

The approach offered here is to use the ash analysis as an input for chemical equilibrium thermodynamic calculations to determine the amount of liquid glue likely to be present in the deposit at a given deposition temperature. The quantity of liquid phase was, in turn, used as input for the sticking code (vide infra) and directly compared to the observed sticking coefficients (Figure 4). The first step in our predictive procedure is calculation of combustion deposit compositions based on the premise that the condensed solution phases indicated by an equilibrium thermodynamic analysis are the ones likely to appear on the target surface. The NASA CEC free-energy minimization computer program (19) is widely used toward this end in spite of several numerical difficulties associated with its newly acquired ideal solution capability; these are usually singular matrices and convergence problems

† There is no provision in the LETR to vary the target temperature independently of the combustion gas temperature; this makes it difficult to decouple the effects of the two temperatures on the sticking coefficient.

are encountered when condensed phases are added. Significant improvements (i.e., the addition of a phase rule check) have been incorporated in the PACKAGE code (20) which is, thus, essentially a more robust version of the CEC-solution code. Due to its demonstrable efficiency in analyzing the complex phase equilibria in coal conversion gas streams and cleanup devices, the PACKAGE program has been used to perform the equilibrium/thermodynamic computations presented here.

Having obtained the condensed liquid phase fraction and composition by exercising the PACKAGE code at the pressure, surface temperatures, and feed compositions of interest, the steady-state sticking coefficient, $\underline{s}$, of impacting fly ash particles is evaluated in the presence of the deposited liquid glue. This is done by means of a mechanistic theory of deposition (12) which incorporates impaction/diffusion interactions neglected in previous work. Briefly, the principles underlying this theory of "self-regulated" liquid-enhanced capture of supermicron ash may be stated as follows. The inertial impaction deposition rate will depend linearly on $\underline{s}$, but $\underline{s}$ itself will depend on the inventory (and physical properties) of "glue" available to each particle on the deposit surface layer. Therefore, the steady-state values of $\underline{s}$ and particle deposition rate must be obtained by solving a coupled nonlinear equation. This fundamental concept is discussed in more detail by Rosner and Nagarajan (12) and Ross, et al. (21).

In Figure 5, the PACKAGE-generated liquid-condensate mole fraction is plotted as a function of surface temperature for the four coals. The glue-liquid solution (assumed to be ideal) is comprised principally of aluminosilicates, silicates, oxides, and sulfates of calcium, potassium, sodium, aluminum, silicon, and titanium. Solid phases predicted to separate out include Al_2TiO_5, Al_2SiO_5, $CaAl_2Si_2O_8$, $CaSO_4$, Fe_2O_3, K_2SO_4, and SiO_2; these are relatively benign with respect to fouling and corrosion, although they could contribute to the erosion of surface material if they were encapsulated in particles larger than about 10 μm diameter. The plotted results show that a minimum fraction of feed material condenses as liquid for KB, while NDL experiences maximum liquid inundation. However, the Arkwright Pittsburgh and Montana subbituminous coals are inverted with respect to Figure 4. Thus, as with ash content, alkali level, and fouling index, the fraction of condensing material in the combustion product stream gives a reasonable qualitative indication of the sticking propensity of the coal-ash but does not correlate exactly with the sticking coefficient, $\underline{s}$. This demonstrates the inadequacy of a strictly thermodynamic analysis to predict the sticking coefficient and again hints at some unknown but vital piece of information required to provide an accurate gauge of deposition behavior. To address this problem, the thermodynamic analyses have been combined with the effects of mass transfer between the gas mainstream and the deposition surface, with the assumption that $\underline{s}$ depends primarily upon the relative arrival rates of ash particles and glue-liquid to the surface.

Using the thermodynamic data to provide the total condensed phase fraction at a given temperature and providing that data to a modified version of the self-regulated sticking computer code (based on the work of Rosner and Nagarajan [12]), calculated sticking coefficients can be obtained for each of the tested coals (Figure 6). Now the predicted ordering of coals with respect to their sticky nature is in line with experimental observation (i.e, NDL >

SCMS > APB > KB).† There is even good quantitative agreement in certain ranges of surface temperature. Discrepancies between the measured temperature dependence of $\underline{s}$ and the prediction may be accounted for by uncertainties in the experimental data collection procedure or limitations in the accuracy of the admittedly preliminary model for sticking or, most likely, both. For instance, the theory does not model the process of ash softening due to high-energy impact (12) in sufficient detail. Improvements to the present theoretical model will be made as fresh data or insight into the physical processes become available.

Another facet of the LETR deposition tests was to study the effectiveness of metallic additives in mitigating deposition-related problems as well as to identify troublesome coal constituents that need to be selectively removed. There are a few precedents reported in literature for our additive strategy. Nagarajan (22) has investigated the use of trace additives to minimize turbine blade "hot corrosion" due to molten alkali sulfate condensation from jet fuel combustion gases. Rathnamma and Nagarajan (23) have studied high-temperature corrosion control by metal additions to vanadium-contaminated fossil fuels. A recent study conducted by Battelle Columbus Laboratories evaluated the use of chemical additives to reduce gas-side fouling and corrosion in oil- and coal-fired systems (24). Attempts have been made to counteract high-temperature fouling with $CaCO_3$ and with boron-, manganese-, and magnesium-based additives. The Saskatchewan Power Corporation has used limestone to combat ash fouling in boilers fired with lignite (24). Austin (25) has examined the effect of sodium on the strength of sintered ash mixtures. The effects of added alumina and emathalite particles were investigated by Shannon (26) in an effort to reduce alkali concentration by gettering sodium in the combustion process.

However, even when such tactics have proved to be successful, the reasons for the success have not been clearly understood, particularly in coal combustion applications. In order to address this deficiency in our appreciation of the roles played by the individual additives, our research does not merely acquire empirical information regarding the "best" additive, but attempts to gain insight into what makes the "best" additive so effective.

The first round of deposition tests in the LETR were conducted with sodium benzoate as the metal-containing additive. Upon addition of a 30-fold excess of sodium to a sample of APB coal, the sticking coefficient at 1,107 K was raised from about 0.15 to about 0.6, a four-fold magnification. This is consistent with the formation of a larger condensed phase fraction following the addition of a large excess of sodium (Figure 9). Sticking coefficients obtained for lower target temperatures (< 1,000 K) showed no change upon addition of the sodium, which is expected because the liquid phase fraction is not sensitive to sodium level as the temperature decreases significantly below the melting point of sodium sulfate (1,157 K). Future experiments will utilize dopants containing aluminum, magnesium, calcium, and other metals.

---

† The lower ash content of the Spring Creek coal relative to the Arkwright coal implies a larger inventory of glue available per impacting particle and, hence, enhanced sticking coefficients.

An equilibrium thermodynamic analysis of the effect of these additives on condensed liquid formation during the combustion of the APB coal in the LETR has been carried out and the results are displayed in Figures 8 and 9. In these figures, the mole fraction of the molten solution condensate in the combustion product mixture is plotted against additive concentration, the axes being nondimensionalized with respect to corresponding reference Arkwright coal values. From Figure 8, it appears that iron, silicon, calcium, and aluminum are all effective suppressants of glue-liquid formation, with aluminum being the most effective of these. Figure 9 indicates that potassium, sulfur, and titanium are bad additives (i.e., adulterants that should be removed from the coal to reduce its fouling tendency). Sodium and magnesium additions do not result in monotonic trends; 10 times as much sodium in the seeded coal as in the reference coal results in a minimum solution phase fraction, and about 10 times as much magnesium results in maximum. Since, on the basis of the ash deposition theory (12), these phase fractions correlate fairly well with predicted sticking coefficients, an optimum level of each additive that minimizes sticking may be determined on the basis of these plots. However, the added mass loading introduced may increase erosion of machine components even though fouling is alleviated. These considerations, while of secondary importance to this paper, should certainly be included in a more ambitious life prediction venture.

The influence of sodium and aluminum additives on the predicted sticking coefficient at a LETR target temperature of 1,107 K is displayed in Figure 7. With the addition of sodium beyond 10 times its level in the reference Arkwright coal, $\underline{s}$ begins to increase until it reaches a value of about 0.6 at 30 times the reference value of sodium concentration which is in reasonably good quantitative agreement with the experimentally measured sticking coefficient under these conditions. In the aluminum added case, $\underline{s}$ drops to about a third of its value of 0.6 (corresponding to combustion of sodium-enriched coal) with the addition of only about five times as much aluminum as is present in the reference Arkwright coal and remains nearly constant with further increases in the aluminum concentration. The predictions in Figure 7 also suggest the interesting possibility of decreased $\underline{s}$ upon addition of smaller quantities of sodium; a fact which no doubt contributed to the lack of correlation between alkali level and sticking coefficient. These trends will be explored as testing of sodium- and aluminum-doped coals continues. A confirmation, based on such comparisons, of the accuracy of our theory in predicting sticking behavior of coals will imply the availability of a powerful predictive tool that will enable us to evaluate different coals with respect to their fouling characteristics and aid in the development of suitable seeding/cleanup techniques to minimize ash deposition.

To assist in acquisition of the sticking data, a new deposition test facility has been fabricated. It is performance rated at 12 atmospheres as opposed to the previously available atmospheric pressure LETR unit and contains three sets of optical access ports which permit the use of non-intrusive optical diagnostic equipment. The combustion/deposition entrained reactor (CDER) has a higher throughput, a wider range of accessible velocities and temperatures, a temperature-controlled target assembly, and an extensive set of automated control features. In addition, the target assembly may be modified to examine impaction geometries other than 90° and thereby extend our studies beyond the stagnation point to model deposition on the pressure and vacuum sides of a gas turbine blade. Some of the code modifications under way include an improved

description of deposit thermal conductivity (21), incorporation of deposit shape effects and differential sticking coefficients (obtained from high-speed photography of growing deposits), addition of a subroutine to allow glue uptake by particles during their transit across the boundary layer (this may be studied experimentally by methods similar to those of Liang [5]), consideration of simultaneous deposit erosion (i.e., negative instantaneous sticking coefficients), and incorporation of phase change processes and particle-glue diffusion within already formed deposits (possibly accessible by in situ specular reflectance FTIR).

CONCLUSIONS

Predictions of ash fouling behavior have previously been made based on a variety of empirical or thermodynamic factors. Unfortunately, neither the empirical parameters (i.e., sodium level, fouling index) nor the thermodynamics-based liquid phase fraction provided an adequate prediction of the sticking behavior of a given coal. However, by a combination of thermodynamic analysis via the PACKAGE code to obtain liquid phase fractions and the application of that data within the context of the self-regulated sticking concept (12), a fairly good comparison was obtained between predicted sticking values and experimental results. This was especially encouraging because the self-regulation concept is still in its developmental stages.

The overall objective of this research has been to suggest methods of mitigating the deposition process in direct coal-fired gas turbines and, thus, relieve the economic burdens of maintenance and aerodynamic efficiency loss. The good agreement between the simple equilibrium/mass transfer model and the sticking coefficients obtained in the LETR represents a first step toward that objective. Thus, given the ultimate analysis of a particular lot of coal, the propensity of that coal to form deposits in a boiler or gas turbine could be determined. In addition, specific coal cleaning procedures or coal additives could be recommended to mitigate the formation of deposits. A combined experimental and theoretical program has been initiated that extends the work presented here to provide a data base of standard coal, coal additive, and pure mineral sticking coefficients. In the course of these tests, the sticking model will be updated to better reflect conditions within actual gas turbines. Future manuscripts will provide detailed comparisons between the operational characteristics of real-life gas turbines and the deposition and combustion environments in the LETR and the CDER, and the relationships between sticking coefficients, turbine fouling rates, and actual as well as simulated turbine deposit compositions.

ACKNOWLEDGMENTS

This work was funded by the U.S. Department of Energy's Fossil Energy Advanced Research and Technology Development Program. Jeffrey S. Ross acknowledges funding through the Oak Ridge Associated Universities Postdoctoral Training Program. The authors appreciate the assistance of Dale W. Wilson, Jr. in construction of the apparatus, David R. Goff in the design of the two-color optical pyrometer, and Cindy J. Romanowski for the collection of some of the experimental data.

DISCLAIMER

The use of trade names by the authors of this paper does not imply the endorsement of any product, apparatus of configuration by the authors, the U.S. Department of Energy, or by Oak Ridge Associated Universities. Such references are made only for the purpose of clarity.

REFERENCES

1. Cross, N.L., and R.G. Picknett, "Particle Adhesion in the Presence of a Liquid Film," The Mechanism of Corrosion by Fuel Impurities, H.R. Johnson and D.J. Littler, eds., Butterworths, London, pp. 383-390 (1963).

2. Wibberley, L.J., and T.F. Wall, "Alkali-Ash Reactions and Deposit Formation in Pulverized Coal-Fired Boilers: The Thermodynamic Aspects Involving Silica, Sodium, Sulphur, and Chlorine," Fuel, 61, 87-92 (1982).

3. Wibberley, L.J., and T.F. Wall, "Alkali-Ash Reactions and Deposit Formation in Pulverized Coal-Fired Boilers: Experimental Aspects of Sodium Silicate Formation and the Formation of Deposits," Fuel, 61, 93-99 (1982).

4. Wibberley, L.J., and T.F. Wall, "Deposit Formation and Sticky Particles from Alkali-Ash Reactions," Fouling and Slagging Resulting from Impurities in Combustion Gases, R.W. Breyers, ed., Engineering Foundation, New York, New York, pp. 493-513 (1983).

5. Liang, B., A. Gomez, J. Castillo, and D.E. Rosner, "Experimental Studies of Nucleation Phenomena within Thermal Boundary Layers -- Influence on Chemical Vapor Deposition Rate Processes," submitted to AIChE Journal.

6. Aluwalia, R., K. Im, C.F. Chuang, and H.K. Geyer, "Evolution and Deposition of Ash Particles in Coal-Fired Gas Turbines," Proceedings of the First Annual Heat Engines Contractors Meeting, May 1-3, 1986, pp. 317-325, DOE/METC/84-31(CONF-8405138--)(DE85001953).

7. Raask, E., "Creation, Coalescence, and Capture of Mineral Species in Coal Flames," J. Institute of Energy, 231-239 (1984).

8. Scandrett, L.A., and R. Clift, "The Thermodynamics of Alkali Removal from Coal-Derived Gases," Journal of the Institute of Energy, 391 (1984).

9. Anderson, R.J., C.J. Romanowski, and J.E. France, "The Adherence of Ash Particles from the Combustion of Micronized Coal," Research Report, DOE/METC-85/2007 (DE 85008600), October 1984.

10. Anderson, R.J., C.J. Romanowski, R.E. Conn, and R.A. Dennis, "Deposition Effects in the Combustion of Coal-Derived Fuels," Proceedings of the Advanced Research and Technology Development (ARTD) Direct Utilization Contractors Review Meeting, 252-264 (August 1985). DOE/METC-85/6027 (DE85013718).

11. Anderson, R.J., S.D. Woodruff, R.A. Dennis, and J.S. Ross, "Deposition Effects in the Pressurized Combustion of Coal-Derived Fuels," Proceedings of the Advanced Research and Technology Development (ARTD) Direct Utilization Contractors Review Meeting, September 1986, in Press.

12. Rosner, D.E., and R. Nagaranjan, "Toward a Mechanistic Theory of Deposit Growth from Ash-Laden Flowing Combustion Gases: 1. Self-Regulated Sticking of Impacting Particles in the Presence of Vapor- or Submicron Mist Glue," to be presented at the AIChE-ASME-ANS National Heat Transfer Conference, Pittsburgh, Pennsylvania, August 9-12, 1987.

13. Hoy, H.R., A.G. Roberts, and J. Stringer, "Combined-Cycle Power Plant Via Pressurized Fluidized-Bed Combustion," Proceedings of the Second Conference on Advance Materials for Alternative Fuel Capable Heat Engines," U.S. Department of Energy and Advance Fuel Research Institute, 2-115 (1985).

14. Satterfield, C.N., "Heterogeneous Catalysis in Practice," McGraw-Hill, New York (1980).

15. Klabunde, K.J., "The Chemistry of Free Atoms and Molecules," Academic Press, New York (1980).

16. Speight, J.G., "The Chemistry and Technology of Coal," Marcel Dekker, New York (1983).

17. Marple, V.A., and K. Willeke, "Impactor Design," Atmospheric Environment, 10, 891-896 (1976).

18. Ghosh, S.K., "Understanding Thermal Coal Ash Behavior," Mining Engineering, 158-162 (1986).

19. Gordon, S., and B.J. McBride, "Computer Program for Calculation of Complex Chemical Equilibrium Compositions, Rocket Performance, Incident and Reflected Shocks, and Chapman-Jouguet Detonations," NASA Sp-273, Interim Revision, March 1976.

20. Yousefian, V., M.H. Weinberg, and R. Haimes, "PACKAGE (Plasma Analysis, Chemical Kinetics, and Generator Efficiency): A Computer Program for the Calculation of Partial Chemical Equilibrium/Partial Chemical Rate Controlled Composition of Multiphase Mixtures Under One-Dimensional Steady Flow," Aerodyne Research, Inc., Report No. ARI-RR-177 (1980).

21. Ross, J.S., M. Ramezan, R.J. Anderson, and R. Nagarajan, "Prediction and In Situ Measurement of the Thermal Conductivity of Multiphase Fouling Deposits Formed in Direct Coal-Fired Combustors," to be presented at the ASME 1987 Winter Annual Meeting Session on Measurements in Combustion Equipment, Boston, Massachusetts, December 13-18 (1987).

22. Nagarajan, R., "Theory of Multicomponent Chemical Vapor Deposition Boundary Layers and Their Coupled Deposits," Dissertation Thesis, Department of Chemical Engineering, Yale University, May 1986.

23. Rathnamma, D.V., and R. Nagarajan, "High-Temperature Hot Corrosion Control by Fuel Additives," to be presented at the Tenth International Conference on Metallic Corrosion, Madras, India, November 7-11, 1987.

24. Marner, W.J., "Gas-Side Fouling," Mechanical Engineering, pp. 70-77, March 1986.

25. Tangsathitkulchai, M., and L.G. Austin, "Studies of Sintering of Coal and Ash Relevant to Pulverized Coal Utility Boilers," Fuel, 64, 86-92 (1985).

26. Shannon, S., MS Thesis, University of Pittsburgh, 1986.

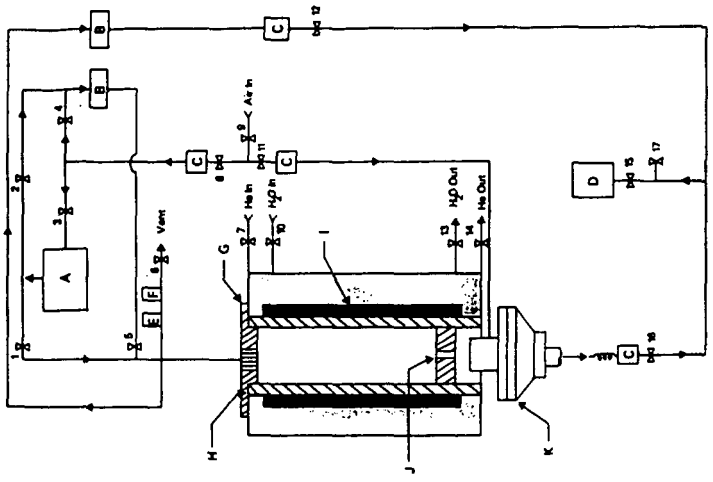

Figure 1. Laboratory Entrained Test Reactor (LETR) Schematic Drawing: A, Fluidized-bed aerosol generator; B, Absolute filters; C, Mass flow controllers; D, Vacuum pump; E, Pressure relief valve; F, Pressure transducer; G, Preheater with flow straightener; H, Alumina muffle tube; I, Graphite heating element; J, Acceleration nozzle; K, Filter holder.

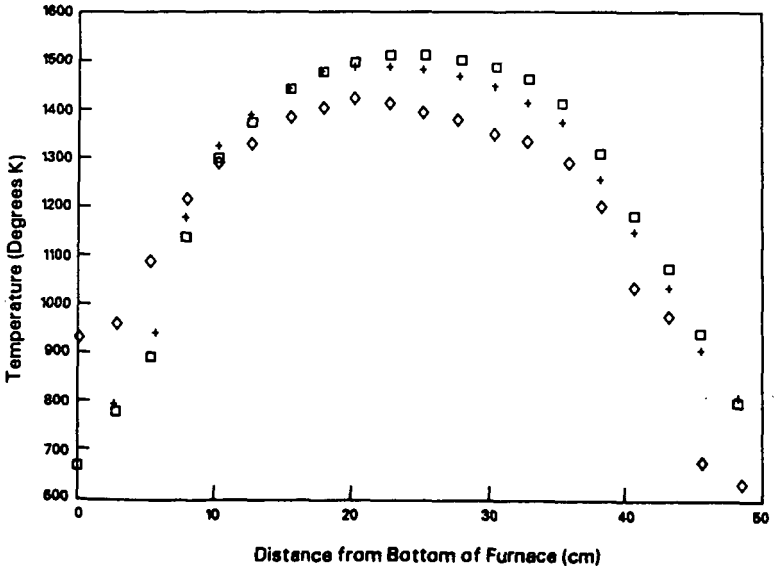

Figure 2. Temperature Profile in the LETR Without a Nozzle: □, 42 m Volts and 0.3 lpm; +, 42 m Volts and 1.0 lpm; ♦, 42 m Volts; and 3.0 lpm.

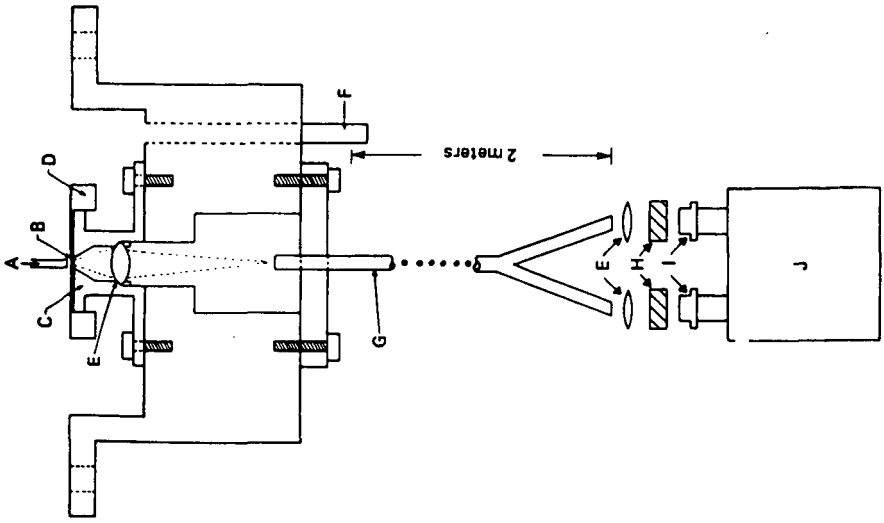

Figure 3. Target Assembly with Fiber Optic Pyrometer: A, Nozzle; B, Target; C, Target Pedestal; D, Target Retaining Ring; E, Lens; F, Exhaust; G, Fiber Optic; H, Optical Filter; I, Detector; J, Signal Amplifier, Electronics and Computer Interface.

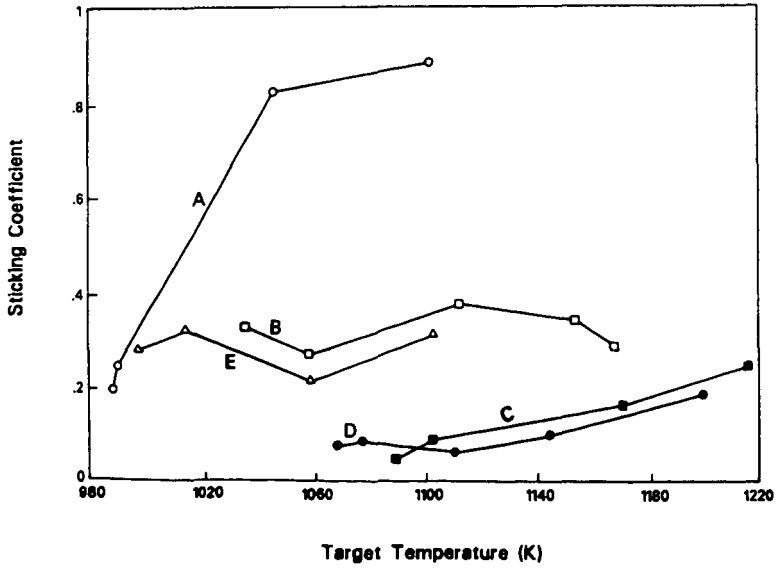

Figure 4. Measured Values of Sticking Coefficient Versus Target Temperature for Tested Coals: A, North Dakota Lignite; B, Spring Creek Montana Subbituminous; C, Arkwright Pittsburgh Bituminous; D, Kentucky (Cleaned AMAX-2) Bituminous; E, Acid Washed Lignite.

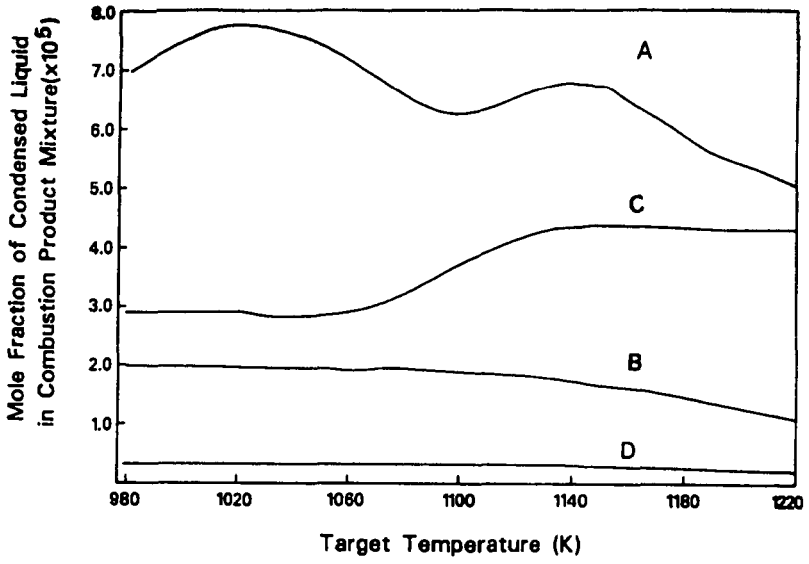

Figure 5. Predicted Values of Condensed Glue Fraction Versus Target Temperature for Tested Coals: A, North Dakota Lignite; B, Spring Creek Montana Subbituminous; C, Arkwright Pittsburgh Bituminous; D, Kentucky (Cleaned AMAX-2) Bituminous.

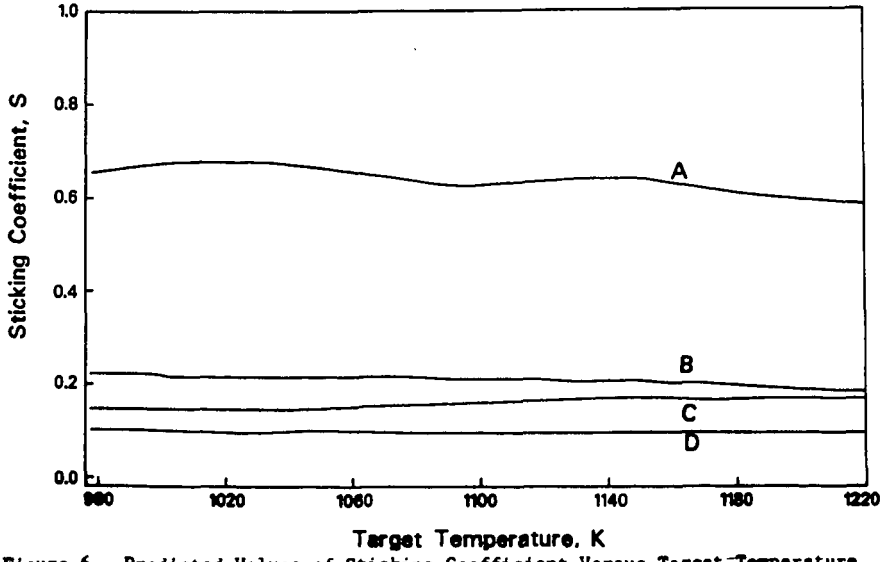

Figure 6. Predicted Values of Sticking Coefficient Versus Target Temperature for Tested Coals: A, North Dakota Lignite; B, Spring Creek Montana Subbituminous; C, Arkwright Pittsburgh Bituminous; D, Kentucky (Cleaned AMAX-2) Bituminous.

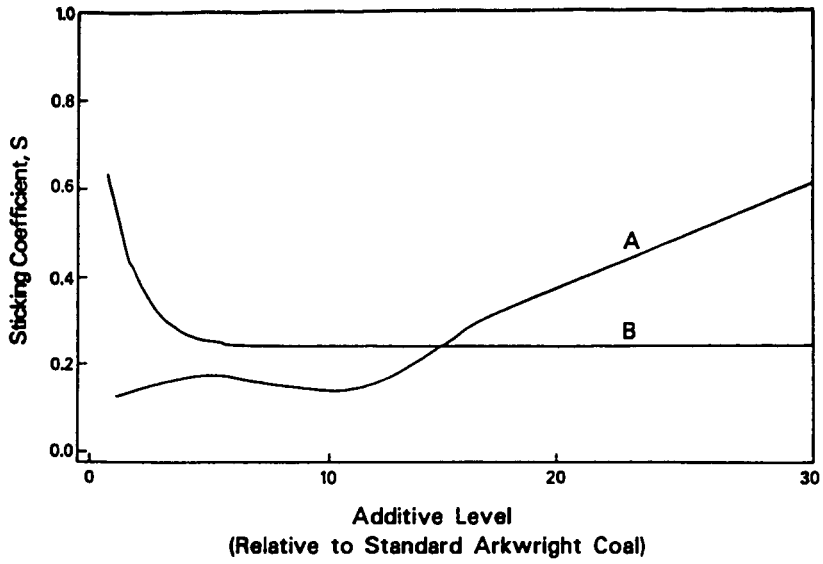

Figure 7. Predicted Effect of Additives on Impacting Ash Particle Sticking Characteristics in the LETR. Target Surface Temperature = 1107 K. A, Sodium; B, Aluminum.

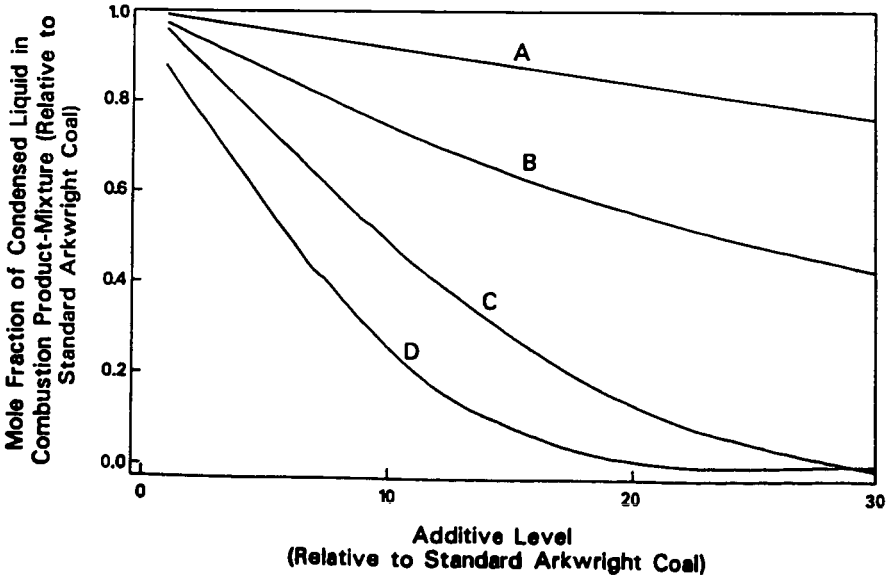

Figure 8. Predicted Effect of Additives in Supressing Condensation of Liquid Glue on the Target Surface in the LETR. Target Surface Temperature = 1107 K. A, Iron; B, Silicon; C, Calcium; D, Aluminum.

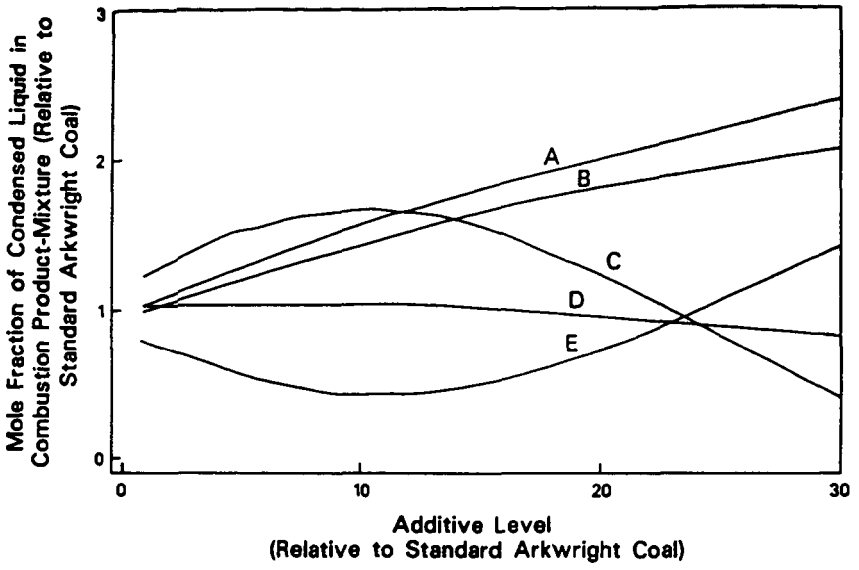

Figure 9. Predicted Effect of Additives on Condensation by Liquid Glue on Target Surfaces in the LETR. Surface Temperature = 1107 K. A, Potassium; B, Titanium; C, Magnesium; D, Sulfur; E, Sodium.

TABLE 1

Ash Composition of Coals Tested in LETR

COAL RANK	Arkwright Pittsburgh Bituminous	Kentucky (Cleaned) Bituminous	Spring Cr. Montana Subbituminous	North Dakota Lignite	North Dakota (Acid Washed) Lignite
% ASTM ash	6.93	0.68	2.30	20.45	16.05
Ash Comp.(Wt%)					
SiO_2	48.09	25.48	18.6	20.08	*
Al_2O_3	25.07	15.92	13.5	11.19	*
Fe_2O_3	10.95	32.35	4.7	13.19	*
TiO_2	1.27	7.77	1.3	0.48	*
P_2O_5	0.18	0.48	0.4	0.28	*
CaO	5.78	1.32	26.5	22.85	*
MgO	1.25	0.62	6.5	6.68	*
K_2O	1,16	0.30	0.1	0.32	*
Na_2O	0.90	9.53	13.1	8.26	*
SO_3	5.34	6.22	15.4	16.07	*

* An insufficient quantity of coal ash was available for quantitative analysis.

DESORPTION TURNOVER NUMBERS FOR THE CARBON-OXYGEN REACTION

Joseph M. Ranish
General Electric Company
Cleveland, OH 44112

Philip L. Walker, Jr.
The Pennsylvania State University
University Park, PA 16802

INTRODUCTION

For graphitic carbons reacting with O_2, it is well established that the C atoms in the gasification products originate from the active surface, the (11*l*) and (10*l*) planes [1,2,3,4,5,6]. Even when the basal plane is gasified, it is gasified at defects which expose C atoms in these planes [7]. The gasified atoms are produced via either or both of the reactions below depending upon the reaction conditions.

$$C_{sd}(O)(s) \xrightarrow{k_1} CO(g) \tag{1}$$

$$2C_{sd}(O)(s) \xrightarrow{k_2} CO_2(g) + C_{sd}(s) \tag{2}$$

The 'sd' subscript (strongly desorbing) in reactions 1 and 2 is used to show that only part of the active surface, the part comprised of C_{sd} surface atoms, is able to form the $C_{sd}(O)$ surface complex which is the precursor to the desorbed products. The rest of the surface oxygen complex is stable [8,9]. The fraction of the active surface which can form unstable surface oxides increases with increasing temperature. Because it is difficult to separate primary product CO or CO_2 from that produced by secondary reactions, a net desorption turnover number for C gasification, TON_C, will be used. It is defined in Equation (3) below as the atoms of C gasified per unit time per O atom of surface complex and incorporates the two more fundamental constants from reactions 1 and 2 above.

$$TON_C = k_1 + k_2[C_{sd}(O)] \tag{3}$$

Square brackets, [ ], denote species activities. Equation (4) shows that TON_C is the slope of the C gasification rate versus $[C_{sd}(O)]$ plot.

$$\text{C gasification rate} = TON_C\,[C_{sd}(O)] \tag{4}$$

To the extent that the steady state primary product CO/CO_2 ratio is large, the gasification rate will be a more linear function of the unstable surface oxide concentration and the TON_C will better approximate k_1.

Although low temperature O_2 chemisorption techniques have been used to measure the active surface [8,10,11], the part of the active surface actually measured and its relationship to the part involved in the gasification, the covered strongly desorbing part, is not always clear. Aside from an in situ spectroscopic examination of the surface which, as yet, is undeveloped, a better way to estimate the surface involved in gasification may be to cool down a gasifying sample in O_2 and then measure the surface O content. At the instant of cooldown, the surface oxides consist

of stable and unstable types. As the temperature decreases, more of the unstable surface oxides become stable. Some of the unstable surface oxides desorb but should be replaced because the activation energies for adsorption and migration of O species are smaller than the activation energy for desorption [12,13,14]. The replacement of recently desorbed surface oxide would be less complete as the kinetics become less dominated by the desorption step. This limits the technique to low temperature, high O_2 pressure gasification. The cooled sample then contains oxygen originating from both the stable and unstable surface oxides. This oxygen can be recovered as CO and CO_2 by heating the surface oxides to about 1240 K [8].

The technique described above was used to study the gasification of a spectroscopic purity graphite powder in various pressures of O_2 at temperatures low enough so that the observed gasification rates were clearly chemically controlled. The results demonstrate a relationship between the gasification rate and the amount of surface oxide collected immediately after gasification. The relationship may be interpreted in terms of stable and unstable surface oxide and yields an estimate for the TON_C. This estimate is compared to global turnover numbers from the literature. The comparisons dramatize the importance of active site coverage in clarifying the role of active surface in gasification.

EXPERIMENTAL

Reactivity and linear programmed thermal desorption (LPTD) runs were performed in the same computer interfaced high pressure flow reactor. Gasification or desorption products were quantified by CO and CO_2 nondispersed infrared detectors and a mass flowmeter. Hydrocarbon free O_2 of >99.99% purity with a reported moisture content < 3 ppm was used for the reactivity studies. Ultra high purity Ar (>99.999%), passed through a Zr alloy gettering furnace to lower H_2O and O_2 levels to < 0.1 ppm, was used for the LPTD runs. The carbon studied was Union Carbide SP-1 spectroscopic purity graphite powder which had a total impurity content of < 0.1 ppm. It was supported unconsolidated in the reactor on high purity alumina or quartz trays or on sapphire disks.

Graphite samples were loaded into the reactor, given a LPTD, then gasified to 20% burn-off at 840±3 K at a fixed O_2 pressure. After cooling in O_2, the surface oxide was collected with another LPTD. Once loaded into the reactor, the sample was not exposed to ambient air until the final LPTD was finished. LPTD's were performed from ca. 300 K to 1234 K at 5 K/min. Full details are given elsewhere [15].

RESULTS AND DISCUSSION

Gasification proceeds through three stages as noted before [16,17]. All samples were burnt-off to 20% to be within the range of steady state gasification. Figure 1 illustrates that, when the reaction conditions are kept constant, the gasification rate exhibits more variability at low sample weights and decreases with increasing sample weight. A mass transfer calculation following the procedure in reference [19] for the case most limited by O_2 transfer yields a value of $\phi^2\eta = 0.0032$ which is safely below the 0.1 upper limit for chemical control. ($\phi^2\eta$ is roughly the ratio of the actual O_2 consumption rate to the mass transfer limited O_2 supply rate.) Therefore, O_2 mass transfer limitation is not causing the decrease in gasification rate with increasing sample weight. For the largest weight samples, CO inhibition can explain the slight gasification rate decreases [18]. For the smaller weight samples, however, the decrease in rate with sample weight appears to be due to the influence of extrinsic catalysis. This view is supported by the higher CO_2/CO

ratio in the product gas for these samples as well as microscopic examinations of the burnt graphite powder which reveal that the smaller weight, higher reactivity samples exhibit a much higher incidence of flakes with roughened edges and channels. The gasification rates were not significantly influenced by changing the sample support materials.

A typical LPTD profile obtained after 20% burn-off in 2.3 MPa O_2 at 837 K is illustrated in Figure 2. All LPTD profiles were similar and differed mainly in the evolution rates and total amounts but little in the rate-temperature profile. Most of the gas recovered during LPTD was CO. It is likely that the similarity in LPTD profiles is due at least partly to very rapid surface oxide migration or rearrangement.

Figure 3 illustrates the relationship between the steady state gasification rate and the surface oxide collected afterwards expressed in terms of total O collected. Because a vertical temperature gradient existed at the highest O_2 pressure, 3.5 MPa, the sample temperature during gasification at this pressure could be as high as 851 K. Regardless of whether the rate differences among the samples are caused by sample size (catalysis) or O_2 pressure differences the data follow the same trend. A least squares linear fit to the data shows that 5.5 μmole O/g of the surface oxide is stable. The excess is unstable and has a TON_C of 0.043 s^{-1}. The absence of significant curvature in Figure 3 implies that the TON_C closely approximates k_1.

This turnover number is compared with other more global turnover numbers from the literature in Figure 4. In Figure 4, the right hand vertical scale is in units appropriate for turnover numbers, the left hand vertical scale is in units appropriate for edge recession rates. Where necessary, reactivities in Figure 4 were extrapolated to 1.3 KPa using an O_2 reaction order of 0.5. The literature global turnover numbers are the gasification rates divided by the total active surface areas, i.e. C atoms gasified per unit time divided by C atoms exposed at edges of basal planes. These global turnover numbers may be obtained directly from microscopic observations of the recession rates of pits in the basal plane [5,20,21,22,25] or of the recession rates of unwet catalyst channels at points far from the catalyst particle [23,24]. They may also be obtained by dividing the gasification rate by the amount of chemisorbed O [8]. The chemisorption conditions must be chosen with care. Low temperature chemisorption may suffer from failure to saturate the entire active surface due to kinetic limitations. At higher temperatures, significant fractions of the active surface will be C_{sd} type and unable to retain surface oxide. Since active surface coverages are not known for the literature global turnover numbers, they cannot be converted into TON_Cs, however they do represent the lower limits to the TON_Cs. The scatter in the data in Figure 4 is probably due to variable coverages of active surface caused by variable degrees of catalysis, since the data were normalized for O_2 pressure. The upper line in Figure 4 is constructed using data having the lowest reported O_2 reaction order of 0.3 [21] and thus the highest active surface coverage. This line should more closely approximate the TON_C.

ACKNOWLEDGEMENTS

This research was performed at The Pennsylvania State University and was supported by the Division of Chemical Sciences, Office of Basic Energy Sciences, U. S. Department of Energy on Contract No. DE-AC02-79ER 10488.

References

[1] J. A. Hedley, Nature, 188, 44 (1960)

[2] I. M. Dawson, E. A. C. Follett, and D. M. Donaldson, Proc. Eur. Reg. Conf. on Electron Microscopy, Delft 1960, Vol. I, p. 337

[3] G. R. Hennig, J. Chim. Phys., 58, 12 (1961)

[4] I. M. Dawson and E. A. C. Follett, Proc. Roy Soc., A274, 386 (1963)

[5] E. L. Evans and J. M. Thomas, Proc. of Third Conference on Carbon and Graphite London 1970, p. 3, Soc. Chem. Ind., London (1971)

[6] J. R. Fryer, Proc. Third Conf. on Industrial Carbon and Graphite, p. 246, Soc. Chem. Ind., London (1971)

[7] C. Wong, R. T. Yang, and B. L. Halpern, J. Chem. Phys., 78(6), 3325 (1983)

[8] N. R. Laine, F. J. Vastola, and P. L. Walker, Jr., J. Phys. Chem., 67, 2030 (1963)

[9] P. L. Walker, Jr., F. J. Vastola, and P. J. Hart in *Fundamentals of Gas-Surface Reactions*, (H. Saltsburg, J. N. Smith, Jr., and M. Rodgers -Eds.), p. 307, Academic Press, NY (1967)

[10] E. M. Suuberg, J. M. Calo, and M. Wojtowicz, ACS Div. Fuel Chem. Prep., 31 (3), 186 (1986)

[11] L. R. Radovic, P. L. Walker, Jr., and R. G. Jenkins, Fuel, 62, 849 (1983)

[12] J. Nagle and R. F. Strickland-Constable, Proc. of the Fifth Conf. on Carbon, Vol 1, p. 154, Pergamon Press, NY (1962)

[13] J. Dollimore, C. M. Freedman, and B. H. Harrison, Carbon, 8, 587 (1970)

[14] P. R. Olander, W. Siekhaus, R. Jones, and J. A. Schwartz, J. Chem. Phys., 57, 408 (1972)

[15] J. M. Ranish, Ph. D. Thesis, The Pennsylvania State University, (1984)

[16] P. Magne and X. Duval, Bull. Soc. Chem., France, 5, 1585 (1971)

[17] D. J. Allardice and P. L. Walker, Jr., Carbon, 8, 375 (1970)

[18] J. M. Ranish and P. L. Walker, Jr., Carbon, 24, 109 (1986)

[19] P. L. Walker, Jr., F. Rusinko, Jr., and L. G. Austin in *Advances in Catalysis*, Vol. XI (D. D. Eley, P. W. Selwood, and P. B. Weisz -Eds.), p. 133, Academic Press, NY (1959)

[20] G. R. Hennig in *Chemistry and Physics of Carbon*, Vol. 2, (P. L. Walker, Jr.-Ed.), p. 1, Marcel Dekker, NY (1966)

[21] J. M. Thomas in *Chemistry and Physics of Carbon*, Vol. 1, (P. L. Walker, Jr.-Ed.), p. 121, Marcel Dekker, NY (1965)

[22] R. T. Yang and C. J. Wong, J. Chem. Phys., 75(9), 4471 (1981)

[23] R. T. K. Baker and P. S. Harris, Carbon, 11, 25 (1973)

[24] R. T. K. Baker and J. J. Chludzinsky, Jr., Carbon, 19, 75 (1981)

[25] J. J. Baker, Ph. D. Thesis, The Pennsylvania State University (1970)

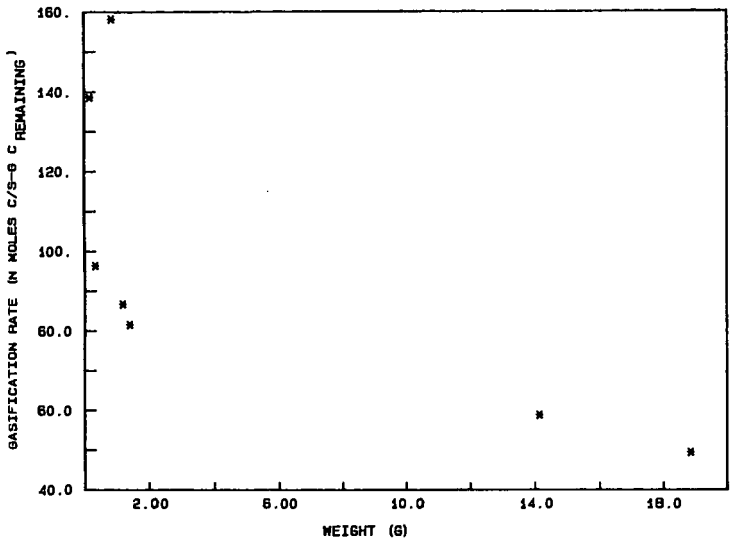

Figure 1: Effect of Initial Sample Weight on Gasification Rate. Gasification at 840±3 K, 0.1 MPa O_2, 20% Burn-Off

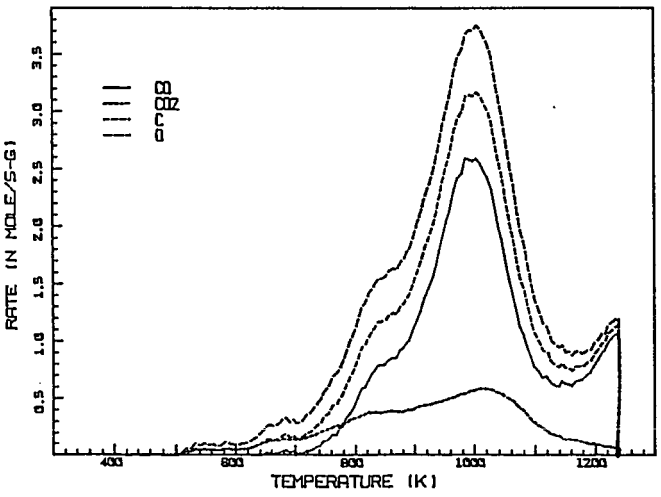

Figure 2: Evolution Rates During LPTD After Gasification. Gasification to 20 % Burn-Off at 837 K in 2.3 MPa O_2

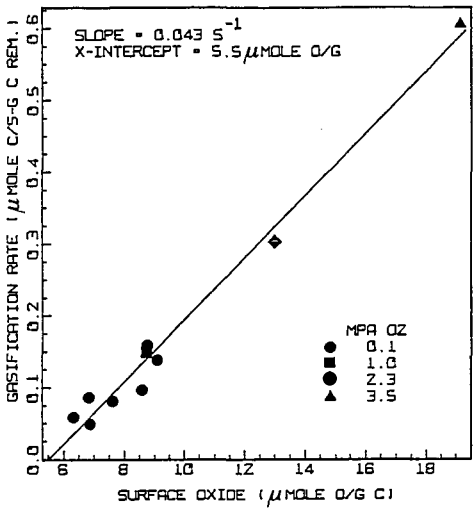

Figure 3: GASIFICATION RATE AT 20 % BURN-OFF, 840±3 K VERSUS SURFACE OXIDE

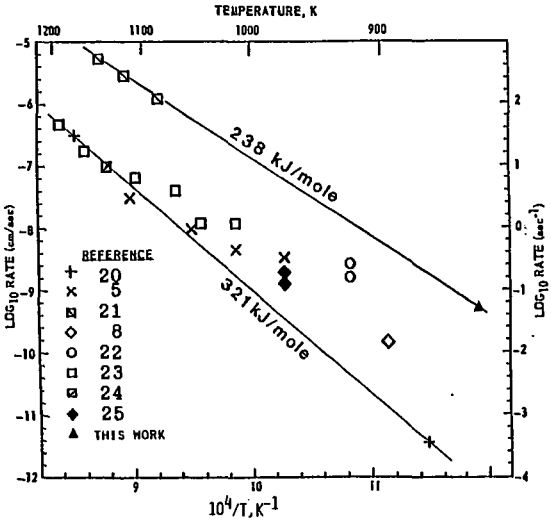

Figure 4: TURNOVER NUMBERS FOR THE CARBON-OXYGEN REACTION AT 1.3 KPA

THE RELATIONSHIP BETWEEN CHAR REACTIVITY AND PHYSICAL AND CHEMICAL STRUCTURAL FEATURES

P.E. Best+, P.R. Solomon, M.A. Serio, E.M. Suuberg*,
W.R. Mott, Jr., and R. Bassilakis
Advanced Fuel Research, Inc., 87 Church Street, East Hartford, CT 06108

INTRODUCTION

This study focuses on correlations observed between char reactivity, on the one hand, and char resistivity and structural properties on the other. It is the continuation of a study reported recently on the relationship between char reactivity and pyrolysis conditions (1). There, it was found, as others have observed before (2-5), that for most coals, reactivity decreases with increasing degree of pyrolysis. As pyrolysis progresses a number of changes occur in the char: hydrogen and oxygen content decrease, a greater degree of order is brought about and changes occur in the sample shape, pore size distribution and surface area.

With so many factors varying, the observation of a correlation between char reactivity and one factor need not imply a cause and effect relationship between the two. The traditional way to deduce cause-and-effect is to vary only one factor at a time, and observe its effect on the measurement. This is not readily done for chars. The result is that the research in char reactivity has established trends, but not a quantitative theory.

A great deal is known about char reactivity, as can be seen from two reviews of the subject (4,5). For the present work, only a subset of this information is needed, which we take from the reviews. Correlation of char reactivity has been made with heteroatom content (oxygen and hydrogen in this instance), with structure and with mineral content. The "structure" generally refers to the number of exposed edge atoms of lamellae (6,7). In pure graphite these sites have been shown to be the most reactive towards oxidation, and it is commonly held that these edge sites are most reactive in chars, also. An exception to this is the location of sites activated by mineral matter. These sites are found in the basal plane of graphite (4). Reactivities have also been correlated with resistivity (8).

In this work, chars have been characterized with respect to reactivity, surface area, heteroatom content, ash content, x-ray diffraction, and resistivity. The char characteristics have been correlated with coal rank, coal mineral content, and the heating rate and final temperature used for char preparations. The paper presents a summary of the observed trends.

EXPERIMENTS

Char Preparation

The experiments described here were carried out on a char formed from phenol formaldehyde resin, as described by Suuberg, et al. (9) and on chars formed from raw and demineralized coals and lignites. Demineralization was carried out by the procedure of Bishop and Ward (10). The chars were formed by heating in an inert gas within an entrained flow reactor (EFR) for a variety of residence times and maximum temperatures, or by heating in a Thermogravimetric Analyzer (TGA) at 30°C/min to 600, 700, 800 or 900°C. The composition of the starting material as well as those of the charred materials, are shown in Table I.

*Div. of Engineering, Brown University, Providence, RI, 02912
+Physics Department, University of Connecticut, Storrs, CT 06268

Reactivity Measurements

Initial char reactivity measurements were made using the isothermal technique developed at Pennsylvania State University (11). In this method, the char is heated in a TGA in nitrogen to the desired temperature, usually 400-500°C. The time for 50% burnoff, $\tau_{0.5}$, is used as the reactivity index. In our char characterization work, we had difficulty applying the isothermal techniques to chars formed over a wide range of conditions. A temperature level selected for one char was inappropriate for another.

In order to overcome this difficulty, a non-isothermal technique was developed using a Perkin-Elmer TGA 2 (1). The sample (about 1.5 mg) is heated in air at a rate of 30 K/min until a temperature of 900°C is reached. The TGA records the sample weight continuously and, at the end of the experiment, the weight and derivative are plotted. The temperature (T_{cr}) at which the derivative of the fractional weight loss with respect to time reaches a value of 0.11 wt. fraction/min was chosen as an index of reactivity. This was compared with the $\tau_{0.5}$ values measured by the isothermal technique and a good correlation was observed (1).

Surface Area Determinations

The surface areas reported in this paper have been obtained at Brown University using a Quantasorb instrument, manufactured by Quantachrome, Inc. The sample cell is immersed in liquid N_2 for N_2 adsorption or a dry ice-acetone bath at -78°C, for CO_2 adsorption. Determinations of surface area from the sorption data have been made using classical BET theory; typically three points have been taken at values of (P/P_o) of 0.1, 0.2, and 0.3.

X-Ray Diffraction Measurement

Powder diffraction patterns were recorded on film with a Debye-Scherrer camera (dia. 57.3 mm), in air. The films were read with a diode-phototransitor pair, feeding a logarithmic amplifier whose output drove the Y-channel of an X-Y recorder. The X-Y chart record, then, is of film darkening (proportional to x-ray intensity) versus distance along the film. Graphite was the reference material. The sample capillary diameter (0.5 mm) and the aperture of the limiting slit in the film reader, were chosen so that the **(100)** and **(101)** lines of graphite were resolved.

Where intensity measurements of more than one sample are compared, the same exposure conditions and times were used to record the data. The background scattering from air and capillary were determined by a "blank" (empty capillary) run, and sample densities were estimated from the sample contribution to the large angle scattering, assumed to be incoherent (12). Heteroatom contribution was not taken into account when estimating the sample density. "Line" intensities were determined by subtracting the interpolated smooth background from the corrected data.

Resistivity Measurements

The apparatus that was used for the sample cell in the electrical resistivity tests is similar in form to that described by Mutso and DuBroff (8), although smaller. In the apparatus used here, a small amount of sample (about 15 mg) is introduced into the cell, and the electrical resistance of the sample, under a constant pressure of 1000 p.s.i. is measured by a digital ohm-meter. Both the exact ($\pm$ 0.1 mg) sample weight and compressed density are determined, and from these measurements and the known cell dimensions, a resistivity is calculated.

It is possible that interparticle resistance, as well as the intrinsic material property, contributed significantly to the measured resistivity. This possibility was investigated for a number of chars by measuring the resistivity for a sieved sample (-200 +325 mesh), and a sample ground to micrometer sized particles. A small effect was seen, although all measurements on one char were within $\pm$ 5%.

Likewise, the effect of char drying on resistivity was investigated. No significant effect was observed between the resistivity of chars that had been in jars for several days, and that of freshly dried material.

RESULTS AND DISCUSSION

Reactivity vs. Extent of Pyrolysis

Figure 1 summarizes the results for chars from the five coals. This figure is based on Fig. 5 of Ref. 1 with additional coals and with measured values rather than calculated values of hydrogen for the Kentucky No. 9 chars. The critical temperature (T_{cr}), which varies inversely with reactivity, is plotted as a function of the (daf) hydrogen content, which is used as a measure of the extent of pyrolysis. For each char type, there is a trend for increasing T_{cr} (decreasing reactivity) with decreasing hydrogen. Most of the change occurs below 2 1/2% hydrogen, after the evolution of aliphatic hydrogen is complete. That is, T_{cr} appears to vary primarily with the concentration of aromatic hydrogen. This variation could be due to a variation in the active site concentration, possibly correlated with the ring condensation accompanying the elimination of aromatic hydrogen. There does not appear to be any drastic effects due to heating rate for low rank coals containing minerals, as chars for a wide range of conditions all fell along the same curve. The preliminary results for bituminous coals and demineralized low rank coals do not exhibit the same degree of reactor independence.

It should be noted that there is also ring oxygen in the char which is removed at about the same rate as the hydrogen and which may be related to the reactivity changes. Similar correlations were observed with oxygen concentration for chars produced from a single coal, i.e., the reactivity decreases with decreasing char oxygen concentration. However, it is thought that the hydrogen is the major indicator of reactivity, since it is present at about five times the level of oxygen on an atomic basis. Our studies indicate that the oxygen content of the parent coal is more important (see below).

The upper solid line in Fig. 1 is a "best fit" line drawn through the data for Kentucky No. 9 and Pittsburgh Seam bituminous chars. The lower solid line is a best fit line drawn through the Zap lignite chars.

Reactivity vs. Mineral Content

It is known that the vertical displacement of the curves in Fig. 1 is at least partly due to the variations in catalytic activity of minerals. This effect has been observed in previous studies which have been reviewed by Mahajan and Walker (13). The most reactive chars are for the Zap lignite which are known to have a high Na and Ca content. The results for T_{cr} versus daf hydrogen content for Zap chars demineralized by two procedures are shown in Fig. 2. In both procedures, the Bishop and Ward technique (10) was used, except that in procedure 1 the HF was used at one-fifth normal strength. It is apparent that this produced a lower extent of demineralization, which was verified by XPES analysis. Both data sets are compared to the "best fit" line drawn through the Zap data in Fig. 1. It is evident that reactivity results for the Zap demineralized by procedure 2 are similar to chars from bituminous coals (see Fig. 1). Samples of Pittsburgh Seam and Illinois No. 6

bituminous coals were also subjected to demineralization but did not exhibit as dramatic an effect.

Reactivity vs. Surface Area

Another area of investigation was the differences in surface area among the chars that were tested for reactivity. N_2 surface areas varied from 1 to over 100 m^2/gram. In general, for any given coal, N_2 surface areas went up with decreasing hydrogen content below 3% hydrogen, where the reactivity was observed to decrease. N_2 surface areas also increase with the extent of burnoff at essentailly constant reactivity. So reactivities do not correlate with N_2 surface areas.

CO_2 surface areas varied from around 10 to over 300 m^2/gram with almost all chars in the range of 100 to 300 m^2/gram. The CO_2 surface area which varies by factors of 3 shows no correlation with reactivity which varies by factors of 100.

The fact that reactivities do not correlate with surface is not surprising. As discussed by Walker and coworkers (3,7,13), it is the active surface area (ASA) as measured by oxygen chemisorbtion which is important. However, Suuberg, et al., (9) have recently called into question the utility of oxygen chemisorbtion as a technique for measuring the ASA of "young" chars. In this work, we have not attempted to measure ASA's.

Reactivity vs. Rank

A systematic study of the variations of reactivity with coal rank has been performed. Figure 3 presents a correlation between the oxygen content in the parent coal and the reactivity of char produced in the TGA by heating in nitrogen at 30°C/min to 900°C. The open squares are results obtained for raw coals, the solid squares show the results for demineralized coals. For raw coals there is a decrease in reactivity with increasing rank. Similar results were summarized by Mahajan and Walker (13). For demineralized coals above 8% oxygen, the reactivity does not vary with oxygen. The results suggest that the decrease in reactivity with increasing rank is a property of the organic matter at high rank (less than 8% oxygen) and mineral matter at lower rank (greater than 8% oxygen).

Reactivity vs. Molecular Order

For a series of chars formed from Eastern and demineralized Western coals and lignites, the reactivity and the x-ray diffraction patterns were measured. With increasing degree of pyrolysis, T_{cr} increases, indicating reduced reactivity (1). This correlation has been observed before (7). Also with increasing degree of pyrolysis, the extent of ordering increases, as indicated by the greater intensity and lower breadth of the **(10)** diffraction line from the chars (Fig. 4). Franklin was amongst the first to describe this particular correlation (14). Combining the two, it is seen that there is a correlation between decreasing reactivity and increasing order, apparently implicating lamellae edges as the active sites.

In looking for a parameter from the x-ray scattering data to characterize "order" in a simple way, it is noted that most workers in the field use crystallite diameter, L_u. For ideal crystallites, the diameter can be found from the breadth of the **(10)** line, or its angular shift$_o$(15). For the chars investigated in this work, lamellae diameters are under 30 A, and do not change dramatically during pyrolysis. On the other hand, the intensity in the **(10)** band, for a fixed density of lamellae, increases as N^2, where N is the number of atoms in the lamellae (15). Under these circumstances, the intensity increases with L_u to the fourth power. The intensity is a very sensitive measure of lamellae growth, and therefore, of order. This is the parameter which Radovic, et al. used in their work (7).

Figure 5 presents the intensity of the (10) band versus the critical temperature, for a number of chars formed by slow heating. These chars were all prepared from demineralized chars to avoid interference from the mineral diffraction lines. It is seen that there is a trend of increasing intensity of the (10) band with increasing T_{cr}. In other words, the chars become less reactive as they become more ordered (7). As mentioned above, other properties of the char change with increasing heat treatment. It has not been demonstrated here that the correlation in Fig. 5 is one of cause and effect; the relationship is as expected, however (5). Chars created at high heating rates (not shown) appeared to fall near the other chars but with higher uncertainty due to their low density.

Reactivity vs. Resistivity

In continuing to seek correlations between char reactivity and other parameters, we were led by the work of Mutso and DuBroff to investigate the relationship between reactivity and resistivity (8).

In the work described in Ref. 8, and other earlier wqrks, the relationship between reactivity and resistivity was performed for cokes, formed from coking coals which come from a relatively narrow range of coal rank. In the present case we plot reactivity, indicated by T_{cr}, versus resistivity, for a wider range of starting coals, including the demineralized lignite, as well as for the resin char (Fig. 6).

Also in Fig. 6 are plotted data points for chars formed from North Dakota lignite without treatment. These are the points on the line far removed from the shaded band which encompasses all other points. For Eastern coals, and for demineralized Western lignite, there is an excellent correlation between char reactivity and electrical resistivity.

The removal of the data points from the shaded band for lignite with minerals, can be traced to the effect of minerals on reactivity (4). The minerals do not have a major effect on resistivity for the samples measured here.

CONCLUSIONS

Results are presented which are used to make, or to restate, the following conclusions:

- A new test has been developed which allows relative reactivity to be determined for chars of widely varying reactivity.
- Reactivity was found to decrease with increasing extent of pyrolysis, as determined by (daf) hydrogen content.
- The effect of heating rate or reactivity appeared to be unimportant for non-demineralized low rank coals.
- The differences in reactivity of chars do not depend strongly on the char surface area measured by N_2 or CO_2.
- For coals with more than 8% oxygen, mineral effects appear to be important in determining reactivity differences between chars from different coals.
- A relationship between extent of order and char reactivity is demonstrated for chars formed by slow heating. This is done by plotting T_{cr} against the intensity of the (10) x-ray diffraction line.

- The work done by others (8) showing a correlation between coke reactivity and electrical resistivity, is extended to chars. Again, a correlation is observed, although only in the absence of mineral effects.

ACKNOWLEDGEMENT

This work was supported under Contracts No. DE-AC21-84MC21004 and DE-AC21-85MC22050 from the Morgan Energy Technology Center of the Department of Energy.

REFERENCES

1. Solomon, P.R., Serio, M.A., and Heninger, S.G. ACS Div. of Fuel Chem. preprints, **31**, (2), 200, (1986).
2. van Krevelen, D.W., Coal, Elsevier, NY, (1961).
3. Laine, N.R., Vastola, F.J., and Walker, P.L., Jr., Proceedings of the 5th Carbon Conference, **2**, 211, Pergamon Press, NY (1963).
4. Essenhigh, R.H., in Chemistry of Coal Utilization, Suppl. Vol., (H.H. Lowry, Ed.), J. Wiley, Chapt. 20, (1962) and references therein.
5. Laurendeau, N.M., Progr. En. Comb. Sci, **4**, 221, (1978) and reference therein.
6. Chang, H.W. Rhee, S.K., Carbon, **16**, 17, (1978).
7. Radovic, L.R., and Walker, P.L., Jr., Fuel, **62**, 849, (1983).
8. Mutso, R. and DuBroff, W., Fuel, **61**, 305, (1982).
9. Suuberg, E.M., Calo, J.M., and Wojtowicz, M., ACS Div. of Fuel Chem. preprints, 31, (3), 186, (1986).
10. Bishop, M. and Ward, D.L., Fuel, **37**, 191, (1958).
11. Mahajan, O.P., Yarzab, R., and Walker, P.L., Jr., Fuel, **57**, 643, (1978).
12. Franklin, R.E., Acta, Cryst. **3**, 107, (1958).
13. Mahajan, O.P. and Walker, P.J., Jr., Chapter 32 in Analytical Methods for Coal and Coal Products, Vol. II, (C. Karr, Ed.), Academic Press, NY, pp 465-492, (1978).
14. Franklin, R.E., Proc. Roy Soc. A. **209**, 196, (1951).
15. Warren, B.E., Phys. Rev. **59**, 693, (1941).

TABLE I

Composition of Starting Demineralized Coals and Chars (wt% DAF)

	Carbon	Hydrogen	Nitrogen	Ash
Zap Lignite	63.54	4.32	0.79	0.18
Lignite Charred in EFA to 0"	78.85	2.55	1.05	0.76
8"	86.31	1.36	0.79	0.60
16"	87.55	0.93	0.91	1.54
24"	88.74	0.51	0.53	0.43
Lignite Charred in TGA at 30°C/min to a final temp. of 600°C				0.38
700°C				0.37
800°C				0.49
900°C				0.29
Pocahontas Coal	91.03	4.71	0.98	1.54
Rosebud Coal	72.10	4.90	1.20	3.68
Pittsburgh Seam Coal	80.90	5.50	1.40	2.31

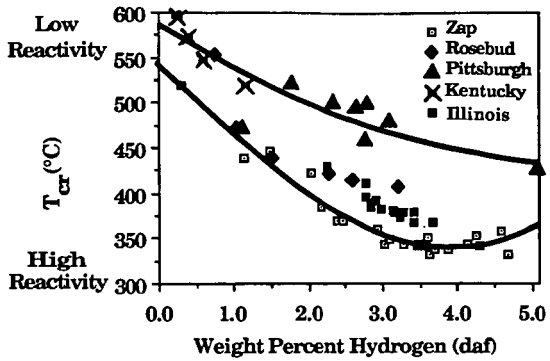

Figure 1. Comparison of Reactivity for Chars from Five Coals of Various Rank as a Function of Hydrogen Concentration. T_{cr} Varies Inversely with Reactivity.

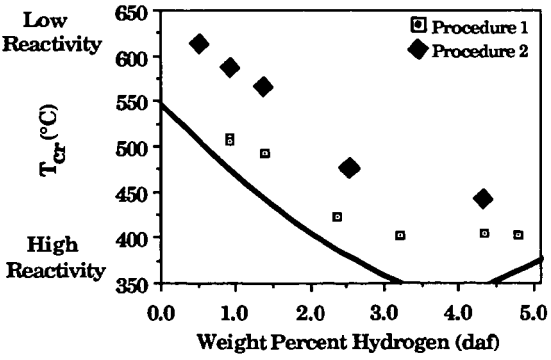

Figure 2. Comparison of Reactivity of Chars from Demineralized Zap Lignite (data) with Chars from Raw Zap Lignite (line from Figure 1). Procedure 1 was a Modification of the Bishop and Ward (ref.10) technique with a Lower HF Strength. Procedure 2 was the Standard Bishop and Ward Technique.

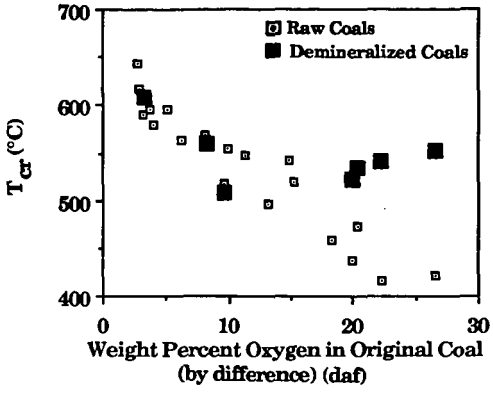

Figure 3. Variation of Reactivity with Coal Oxygen Content for Chars Prepared by Heating in Nitrogen at 30°C/min to 900°C.

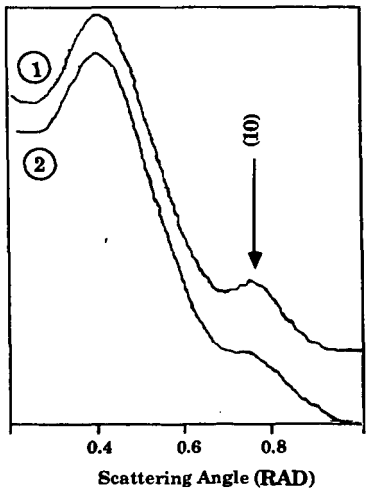

Figure 4. Diffracted X-ray Intensity Versus Angle, for Two Chars Formed from Demineralized North Dakota (Zap) Lignite. The Curves have been Displaced Vertically to Facilitate Comparison. The Char for (1) was Formed by Heating at 0.5°C/sec to 900°C; for (2) to 600°C.

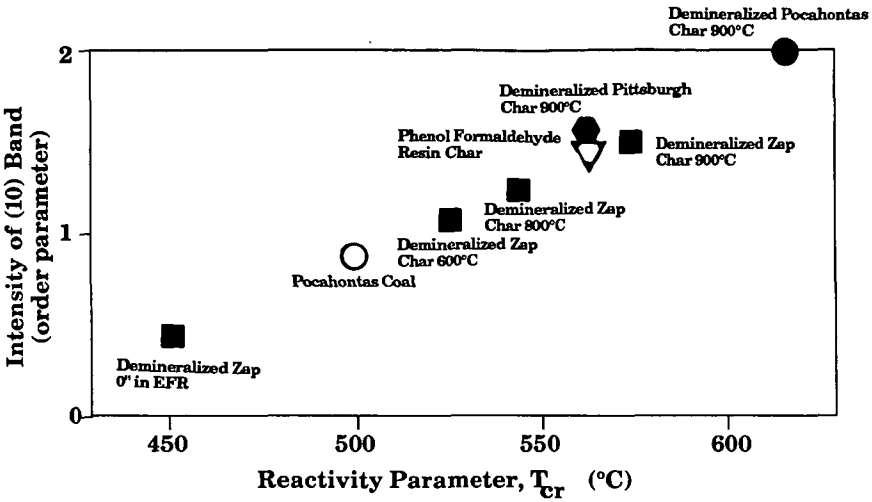

Figure 5. Plot of Order Versus Reactivity for some Eastern and Demineralized Western Chars Formed Under Slow Heating Conditions, and One High Rank Coal.

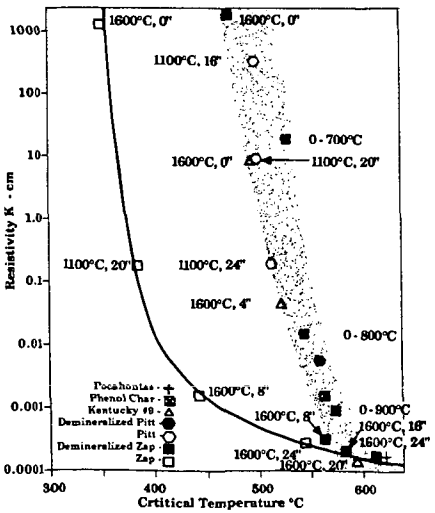

Figure 6. Plot of Resistivity Versus Critical Temperature for a Variety of Chars. The Data for Eastern Coals, or Demineralized Western Coals, Fall Within the Shaded Band.

Role of Carbon Active Sites in the Oxidation of Coal Chars

Robert G. Jenkins and Andrej Piotrowski

Fuel Science Program
The Pennsylvania State University
University Park, PA 16802

INTRODUCTION

Over the last two decades there have been numerous coal char and carbon gasification studies that have determined relative rates of the carbon/gas reactions. It has been demonstrated, quite clearly, that the measured chemical reactivities of chars are functions of coal rank, pyrolysis severity, the presence of catalytically active species, and, of course, the reactant gas and the specific reaction conditions utilized. The goal of this, and other investigations is to attempt to rationalize this range of reactivities in terms of some fundamental parameter/property of the char. The specific aim is to determine if a fundamental rate constant can be obtained for, say, the carbon-oxygen reaction. It is felt that such an approach will lead, eventually, to a better understanding of char gasification in terms of theoretical and practical considerations.

Our approach has been to examine further the role that carbon active sites play in governing the reactivity of a wide range of chars and carbons. This concept was first put forward by Laine et al. (1,2) and has been extended by others (3,4,5). There appear to be relationships between reactivity and active site concentrations (as determined by oxygen chemisorption). The thrust of this study was to extend these types of reactivity studies and to examine, especially, the changes in active site concentration with degree of gasification (burn-off). An attempt has been made to develop a concept of "reactive" sites. That is, to consider sites that are actively participating in gasification reactions. The starting point of this concept is to define an equivalent reactive surface area (RSA) that can be utilized to normalize rates in terms of a pseudo Turn-over Number (TON).

EXPERIMENTAL

i. Materials

Five coals ranging from lignite to anthracite have been used throughout this study. In addition, a relatively "pure" carbon was prepared from Saran polymer (a copolymer of vinyldene and vinyl chloride). The coals are PSOC 833 - a Montana lignite; PSOC 465 - a Wyoming subbituminous A coal; PSOC 1099 - a HVA coal from Pennsylvania; PSOC 1133 - LV, Pennsylvania coal; and PSOC 868 - a Pennsylvania anthracite.

Samples of the raw coals were subjected to a range of pretreatments to alter, in a selective fashion, the inorganic constituents. These modifications were brought about by ion exchange and acid-washing procedures for the lignite (PSOC 833) and by acid-washing procedure for the other coals. Selected samples of all the coals were treated with calcium acetate solutions, varying from 0.001 M to 1.5 M, in order to change the calcium loading in the coals. Chars/cokes from the raw and treated coals were prepared either by slow heating (10^{o}K/min) up to final temperatures of between 975 K and 1275 K, or by rapid pyrolysis (~ 10^{4} K/min) at 1275 K in an entrained flow reactor.

ii. Apparatus and Procedures

Isothermal and nonisothermal reactivities were determined in thermogravimetric analyzers (TGAs). Concentrations of CO and CO_2 in the product gas stream were measured by nondispersive infrared analyzers.

Nonisothermal reactivity measurements were performed using a small sample of coal (< 4 mg) placed in a TGA bucket and heated at a constant heating rate 5 K min^{-1} to an ultimate final temperature in the reactant gas (air). The weight loss, and its first derivative were recorded. The parameter used to represent this reactivity is T_m, the temperature at which the maximum rate of weight loss (maximum of the first derivative) occurs. For isothermal reactivity measurements a sample of char is heated to the desired reaction temperature, in the absence of oxidizing gas, and then the reactant (air) gas was introduced. Weight change and its first derivative with time were determined directly by the thermogravimetric analyzer and also calculated from the composition of the gaseous products of reaction (CO and CO_2). Thus, the TGA reactivity is estimated from the following expression

$$R_{TGA} = 1/w \times \frac{dw}{dt}$$

where R_{TGA} is the reactivity (min^{-1}) at a given temperature and burnoff; w is the mass of the sample and dw/dt the instantaneous slope of the burn-off curve. The reactivity determined from the gas composition is calculated by a similar expression.

Reactive surface area (RSA) at any given level of burn-off is calculated from a knowledge of the quantities of CO and CO_2 evolved. It is assumed that each oxygen atom occupies 0.083 nm^2 (1). Using the values of Reactivity (R) and Reactive Surface Area (RSA), a Turn-over Number (TON) can be calculated (R/RSA). The units of TON are g/m^2 min.

RESULTS AND DISCUSSION

Nonisothermal reactivities for the five coals are listed in Table 1. It can be observed that the reactivity of the coals (T_m-temperature at which maximum weight loss occurs) inversely follows rank. That is, as the rank of coal increases the reactivity decrease (higher value of T_m). Significant differences in the T_m values (630 K to 800 K) are noted over the rank range examined for the raw coals. The values for the demineralized coals exhibit somewhat less variability (701 K to 809 K). It is important to note that the reactivities of the raw subbituminous and lignitic coals are significantly greater than those determined for the respective demineralized samples. However, for the higher rank coals, demineralization can actually produce a slightly more reactive material. Thus, we see that in the lower rank coals, and their chars, the presence of inorganic species does indeed dominate reactivity. In all cases (except raw lignite), heat treatment does reduce "reactivity." As would be anticipated, one also observes that increasing the heat treatment temperature for any given sample produces a less reactive carbonaceous material. These results, of course, show the influence of reduction in active site concentration and possible catalyst deactivation with increasing heat treatment. Overall, perhaps the most important observation to be made is that catalytic effects of inorganic matter in higher rank coals are less important than those found for lower rank coals. In addition, it is possible that during the demineralization process some closed porosity is opened, thus, increasing the overall accessibility to active area. It is also possible that acid treatment reduces the thermoplastic properties of the higher rank coal, which in turn leads to slightly higher reactivity.

It is interesting to note that for lignite the reactivities follow the level of calcium loading. However, loadings above some value of the raw sample (0.09 mmol/g) have relatively little additional influence on reactivity. It should be noted that the biggest changes in reactivity occur at the lower calcium loadings.

Typical isothermal reactivity plots for a char (PSOC 833; Demineralized + 0.3 MCa; rapid pyrolysis at 1275 K, 0.3 s) are given in Figure 1. In this figure one can see that the reactivity profiles, as a function of burn-off, for this sample are very similar for the IR and TGA methods. The major discrepancy occurs at high levels of burn-off. In this case, the instantaneous reactivity appears to be increasing to about 10% burn-off, it then levels off to a relatively constant value up to 40% burn-off, and continues to increase to about 80% conversion. If one uses the gas analysis data to calculate the RSA then one obtains the plot shown in Figure 2. Using these RSA values, a TON as a function of burn-off (at 677 K) can be estimated (Figure 3). The variation of TON with conversion is quite small and appears to remain at a value of about 1.3×10^{-4} g/m^2 min. The only exceptions in this plot are at low levels of gasification (< 5%). We have found that application of this approach yields a relatively narrow range of values for TON for approximately 5 to 85% burn-off from all the chars and carbons studied (prepared at all degrees of pyrolysis severity). As an example, Figure 4 shows the values of TON for all the demineralized, heat treated coals used in this study (reactions for this suite of samples were made at temperatures between 658 to 721 K). It should be noted that TON's for the higher rank coal demineralized chars (anthracite and LV) have values of around 1.45×10^{-4} g/m^2 min, whereas the values for the equivalent chars from the lower rank coals (HVA, Subbit and Lignite) are somewhat lower (~ 1.3×10^{-4} g/m^2 min), and appear to decrease slightly with burn-off. A brief summary of the preliminary data is given in Table 2. These results do show a remarkable degree of constancy for all these materials being gasified in air.

CONCLUSIONS

Nonisothermal reactivity measurements, in air, indicate the influence of the severity of time/temperature history on the subsequent reactivity of chars derived from a wide rank range. Instantaneous reactivities can be normalized by use of a reactive site concept. The calculated TON is quite constant for several chars (and carbons), over a wide degree of conversion and reaction temperature.

ACKNOWLEDGEMENTS

This research was sponsored by the Gas Research Institute, Chicago. Special thanks is given to Dr. Charles Nelson for his continued interest in these studies.

REFERENCES

1. N. R. Laine, F. J. Vastola and P. L. Walker, J. Phys. Chem., 67, 2030 (1963).

2. N. R. Laine, F. J. Vastola and P. L. Walker, 5th Carbon Conf., p. 211, Pergamon Press, Oxford (1963).

3. L. R. Radovic, P. L. Walker, Jr. and R. G. Jenkins, Fuel, 62, 849 (1983).

4. L. R. Radovic, K. Steczko, P. L. Walker, Jr. and R. G. Jenkins, Fuel Processing Technology, 10, 311 (1985).

5. M. R. Khan, ACS (Fuel Chemistry Div.) Preprints, 32(1), 298 (1987).

TABLE 1

VALUES OF TEMPERATURE OF MAXIMUM WEIGHT LOSS (T_m) FOR NONISOTHERMAL REACTIVITIES IN AIR AT 5 K MIN^{-1} FOR ALL COALS AND THEIR RAPID AND SLOWLY PYROLYZED CHARS

Sample	T_m (K) No Pyrolysis	Slow Pyrolysis 975 K (1 h)	Slow Pyrolysis 1275 K (1 h)	Rapid Pyrolysis 1215 K (0.3 s)
Lignite				
Raw	630	630	697	593
Demin	723	755	829	744
Demin + 0.01 Ca	639	660	760	624
Demin + 0.1 Ca	630	613	741	574
Demin + 0.5 Ca	613	622	743	568
Demin + 1.0 Ca	608	619	748	570
Subbit				1275 K (0.3 s)
Raw	648	--	809	--
Demin	701	750	809	709
Demin + 0.1 Ca	--	735	--	588
Demin + 0.5 Ca	--	720	--	541
HVA				
Raw	711	--	846	--
Demin	686	790	811	725
Demin + 0.1 Ca	--	701	--	709
LV				
Raw	735	--	846	--
Demin	704	765	818	730
Demin + 0.1 Ca	--	738	--	728
Anth				
Raw	800	--	853	--
Demin	809	823	851	794
Demin + 0.1 Ca	--	774	--	780

TABLE 2

EXAMPLES OF CALCULATED TON'S AT 50% BO

Sample	Reaction Temp. K	Ton x 10^4 $g/m^2.min$
Saran Char	683	1.52
"	702	1.49
"	710	1.50
"	721	1.53
"	732	1.51
Lignite - Demin (1275, 1 h)	720	1.49
Lignite - Demin + 0.3 Ca (1275, 1 h)	677	1.30
Subbit - Demin (1275 K, 0.3 s)	654	1.38
HVA - Demin (1275, 0.3 s)	635	1.35
LV - Demin (1275, 0.3 s)	638	1.36
Anth. - Demin (1275, 0.3 s)	738	1.50

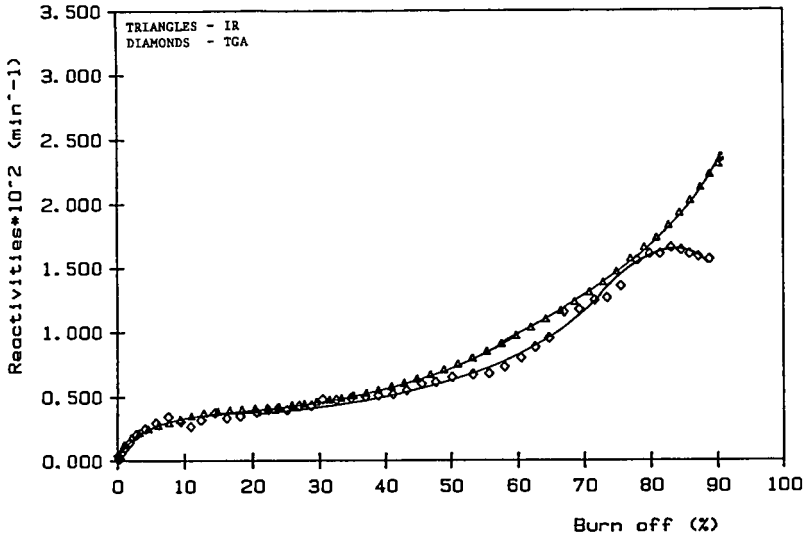

FIGURE 1. TGA and IR Ractivities at 677 K vs. Burn-off for PSOC 833 (DEM + 0.3 Ca) Heated to 1275 K (1 h)

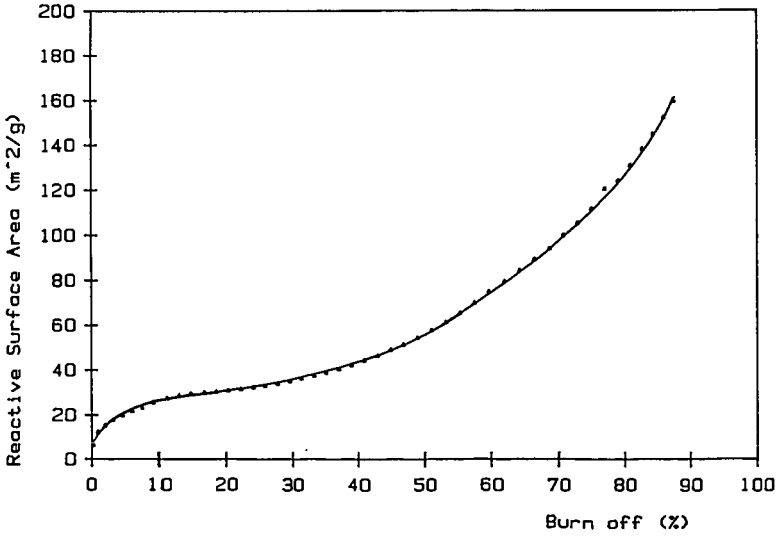

FIGURE 2. RSA vs Burn-off (677 K) for PSOC 833 (Dem + 0.3 Ca), 1275 (1 h)

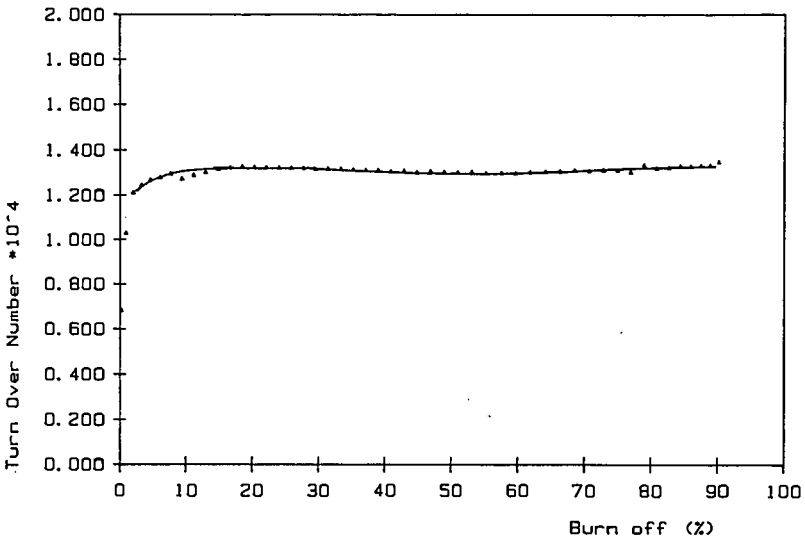

FIGURE 3. TON vs Burn-off (677 K) for PSOC 833 (Dem + 0.3 Ca), 1275 (1 h)

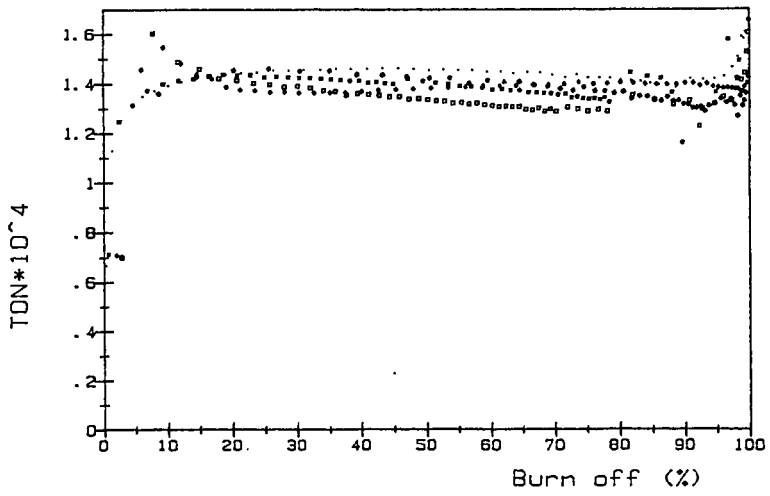

FIGURE 4. TON vs Burn-off for Demineralized Coal Chars (Rapidly Heated)

NON-MAGIC ANGLE SPINNING NMR - AN APPROACH TO DETERMINE THE CHEMICAL SHIFT TENSORS IN CHAR PARTICLES

Naresh K. Sethi,[a] Ronald J. Pugmire,[b]

and David M. Grant[a]

Departments of Chemistry[a] and Fuels Engineering,[b]
University of Utah
Salt Lake City, Utah 84112

INTRODUCTION

Carbon-13 NMR spectroscopy has been widely accepted as a major analytical technique for studying fossil fuels. Axelson[1] and Davidson[2] have reviewed the various solid state NMR spectroscopic techniques for coal studies. Cross polarization/magic angle spinning (CP/MAS)[3] provides information on aromaticity while the dipolar dephasing technique (DD/MAS)[4] provides additional definition of the structure of coal by using the ^{13}C-^{1}H dipolar coupling to separate the carbons into sub-classes; i.e., those that are strongly coupled to protons from those that are weakly coupled in both the aliphatic and aromatic regions of the spectrum. The combination of these two experimental procedures permits one to derive a carbon skeletal structure of coal samples.[5,6]

MAS experiments produce narrow lines in solids but valuable structural information is lost; i.e., the chemical shift anisotropy (CSA) which is a manifestation of the three-dimensional shielding of the nucleus by the surrounding electrons.[7] The CSA is a second rank tensor having three principal elements σ_{11}, σ_{22}, and σ_{33} characterized by unique resonance frequencies. These three tensor components taken together with the isotropic shielding value (the MAS value which is the average of the three tensor components) provide valuable data regarding the local electronic environment. The tensor can be obtained from the ^{13}C NMR spectrum of a finely powdered sample and the tensor elements are extracted by analysis of the line shape. This technique provides not only tensor components but population values as well. However, the spectral analysis is complicated if more than one tensor is present and unique results are not always achievable. Evenso, Pines, et al.[8] used the technique to analyze the static spectra of several coals. These workers succeeded in differentiating the contributions from aromatic and condensed aromatic carbons. Furthermore, they pointed out that there is little difference in the isotropic chemical shifts between these types of carbons and these shift differences cannot be resolved in a CP/MAS experiment. The DD/MAS experiment has been shown to differentiate between benzene-like (i.e., C-H) and non-protonated aromatic carbons[5] (substituted plus inner, or bridgehead) but the resolution of substituted and inner carbons is not readily attainable with standard MAS experiments. The shielding anisotropies of the three general types of aromatic carbons are quite different and, in principal, should be resolvable in the "non-spinning" experiment.

Only for isolated carbons, or for simple compounds where breakpoints in the powder pattern are discernible, is it possible to obtain unique fits of the line shape. Tensor information can be extracted by other techniques such as analysis of the spinning side bands from slow spinning MAS experiments[9] and variable angle sample spinning[10-13] (VASS). In this study we have used the static and VASS methods to study pertinent model compounds and have used these data as a guide to analyze line shapes and extract CSA tensor values and population factors in coals. The experimental techniques are applicable to chars as well as coals. The data permit us to estimate the size of the polycondensed aromatic structure that is the main structural component in chars. The aromatic structure of coal chars should provide valuable information regarding their reactivity.

EXPERIMENTAL

1. NMR Spectroscopy

The NMR spectra were obtained on a Bruker CXP-100 as described previously.[6] The VASS method has been described by Sethi, et al.[13]

2. Spectral Fitting Procedure

The NMR powder pattern analyses were carried out by means of recently developed fitting methods[14]. The technique is briefly described as follows. It is assummed that spins are only experiencing orientation dependent chemical shift interactions. This is usually the case when employing high power proton decoupling. Single spectral simulation requires an initial estimate of these parameters: 1) the principal values of the different CSA's or a linear combination of elements in an irreducible form; 2) the relative intensities; and 3) a broadening factor. One or more of these parameters can be locked to some predetermined or known value, which is then held constant throughout the fitting process. For example, in model organic compounds, the relative intensity is usually locked to the atomic ratios given by the molecular structure. In coals, however, these population parameters are allowed to vary freely so as to provide quantitative data on individual carbon types. Theoretical spectra are calculated using the "POWDER" method[14]. The parameters are adjusted with a simplex optimization routine to minimize the sum of squares deviation between the theoretical and experimental spectra. In cases which necessitate obtaining spinning spectra at different angles, all spectra are fit simultaneously with the same set of CSA values. The total sum of squares from all spectra is used as the minimization criteria. Using this technique, the redundant data provide refinements in fitting parameters which, for a single spectrum, may exhibit ill-conditioned behavior.

RESULTS AND DISCUSSION

Aromatic CSA bands can be calssified into four different subgroups which have tensor components that exhibit variations of ca. 10-20%. These groups are: 1) benzene-like (sp^2 C-H); 2) substituted (e.g. alkylated); 3) condensed (inner and bridgehead); 4) carbons

bonded to heteroatoms (nitrogen, oxygen, etc.).[15] The spectrum of an isolated carbon in a static sample presents a characteristic powder pattern which exhibits break points corresponding to the tensor elements of the individual carbons of each sub-class. Examples of the isotropic peak superimposed with their first three sub-classes, together with their isotropic peaks, are given in Figure 1. These three sub-classes represent the predominant types of aromatic carbons present in chars and high rank coals. An unambiguous tensor analysis usually cannot be performed on static lineshapes due to the overlap of several different CSA bands. This problem is especially accute for aromatic carbons since the upfield components of these bands are usually buried under the much narrower aliphatic resonances. The static spectrum of 1,2,3,6,7,8-hexahydropyrene provides a convenient representation of this problem. In addition, this molecule contains the types of carbons of interest in chars and high rank coals. The components of the individual aromatic carbon tensors have been simulated together with their composite pattern. This composite pattern is compared with the experimental data (Figure 2). The low field components are resolved but the high field (σ_{33} components) are obscured by the aliphatic carbons.

The VASS method scales the individual carbon tensors with respect to their isotropic frequencies by a factor of $1/2(\cos 3\theta^2-1)$ where θ is the spinning angle relative to the external magnetic field.[13] The break points from different bands change as θ is changed. The high field component of the aromatic carbon shielding tensors can be inverted through the isotropic value by proper selection of θ. Hence, overlapping tensor components can be unscrambled by this technique. In addition, a change in θ produces pronounced changes in all of the aromatic tensors so that the line shape is no longer a scaled replica of the static powder pattern. Such intensity and shape changes are readily recognized in our fitting routines which are sensitive to small changes in the line shape. In Figure 3, one observes the line shape changes of an alkylated aromatic carbon as the spinning angle is changed. In Figure 4 the VASS data on hexahydropyrene has been simulated and the tensor components are given in Table 1.

The ability to fit experimental data with high precision is vital to the analysis of complex materials. The hexahydropyrene model is of sufficient complexity to demonstrate the feasibility of unscrambling overlapping tensor components. The availability of multiple angle data decreases the chance of encountering a given spectrum which is insensitive to one or more of the adjustable parameters and therefore reduces ill-conditioned fits of the data.

Using the fitting procedure described above, we have fit the anthracite data (Figure 5). With an aromaticity value $f_a = 1.0$, no alkylated carbons are present and, hence, a multiple angle fit of the data was not deemed necessary. A two tensor fit of the static spectrum produced the results presented in Table 1. The population factor of 0.13 for the C-H tensor is essentially the same as the atomic ratio H/C = 0.123 for this coal. Hence, we are able to independently verify that the method gives valid results.

The anthracite provides a useful model for a char that has been subjected to extensive pyrolysis or to a high temperature environment and thus may be thought of as one extrema of a char model. On the other hand, coals that undergo pyrolysis for relatively short periods of time or at moderate temperatures are not composed entirely of polycondensed aromatic rings. Aromaticity values in the range 0.8 - 1.0 are observed in chars.[16] The inertinite macerals semi-fusinite and fusinite found in coals provide a useful model for char. Natural processes of heat and pressure have produced a char-like material. Such is the case for the Aldwarke Silkstone inertinite (86% inertinite) consisting chiefly of charcoal-like fusinite with an f_a value of 0.88.[6] The tensor components (see Figure 6) and population factors contained in Table 1 provide a distribution of the three major types of aromatic carbons present and one is not required to calculate the atomic ratio for hypothetical unsubstituted nuclei (H_{aru}/C_{ar}) as has been done in the past.[16] One can now directly measure this parameter together with the fraction of substituted carbons without resorting to calculated approximations.

The experimental value of H_{aru}/C_{ar} = 0.39 has been reported previously by means of dipolar dephasing data[6] and, hence, this value was used in fitting the spectra. The fit of the VASS data provided the other two tensors. The population of inner carbons (0.54) and substituted carbons (0.07) provide the remainder of the aromatic structural types. The substituted carbon population is of the order of 0.10, or less, and the total aliphatic carbon content is 0.12. Using the elemental analysis, i.e., the H/C ratio, it is clear that the alkyl substituents, on average, consist of 1-2 carbon fragments and that the non-methyl carbons are highly substituted.

The VASS technique provides a very useful means for supplementing other types of NMR data and is particularly useful in assessing the structure of polycondensed aromatic materials such as chars. As char reactivity is an important consideration in combustion studies, NMR data may be able to play a significant role in structure/reactivity correlation.

ACKNOWLEDGMENTS

This work was supported by the Office of Basic Energy Sciences, Department of Energy under Grant No. DE-FG02-86ER13510 and the National Science Foundation Advanced Combustion Engineering Research Center, Contract No. CDR-8522618.

REFERENCES

1. David E. Axelson, Multiscience Publications Ltd.; CANMET, Energy, Mines, and Resources Canada and the Canadian Government Publishing Centre, Supply and Services Canada, 1985.

2. R.M. Davidson, Nuclear Magnetic Resonance Studies of Coal, IEA Coal Research, Report Number ECTis/TR32, London, 1986.

3. J. Schaefer and E.O. Stejskal, J. Amer. Chem. Soc., 1976, 98, 1031.

4. S.J. Opella and M. A. Frey, J. Amer. Chem. Soc., 1979, 101, 5854.

5. L.B. Alemany, D.M. Grant, R.J. Pugmire, and L.M. Stock, Fuel, 1984, 63, 513.

6. A. Soderquist, D.J. Burton, R.J. Pugmire, A.J. Beeler, D.M. Grant, B. Durrand, and A.Y. Huk, Energy and Fuels, 1987, 1, 50.

7. A helpful review of chemical shift anisotropy can be found in C.A. Fyfe, Solid State NMR for Chemists, C.F.C. Press, Guelph, Ontario, 1983, Chapter 5.

8. D.B. Wemmer, A. Pines, and D.D. Whitehurst, Phil. Trans. Roy. Soc. Lond. A300, 1981, 15.

9. J. Herzfeld and A.E. Burger, J. Chem. Phys. 1980, 73, 6021.

10. E.O. Stejskal, J. Schaefer, and J. McKay, J. Magn. Reson., 1977, 25, 569.

11. J.S. Frye and G.E. Maciel, J. Magn. Reson., 1982, 48, 125.

12. P.D. Murphy, T. Taki, and B.C. Gerstein, J. Magn. Reson., 1982, 49, 99.

13. N.K. Sethi, D.M. Grant, and R.J. Pugmire, J. Magn. Reson. 1987, 71, 476.

14. D.W. Alderman, M.S. Solum, and D.M. Grant, J. Chem. Phys., 1986, 84, 3717.

15. T.M. Duncan, J. Phys, Chem. Ref. Data, 1987, 10(No. 1), 125.

16. E. Furimsky and J. Ripmeester, Fuel Proc. Technal., 1983, 7, 191.

TABLE 1

Tensor Components[a] for Aromatic Carbons

Sample/Carbon Type	σ_{11}	σ_{22}	σ_{33}	Population[b] Factor
1,2,3,6,7,8 hexahydropyrene				
Benzene-like	225	128	22	0.40
Substituted	231	168	9	0.40
Inner	203	197	-6	0.20
Anthracite (PSOC-867)				
Benzene-like	217	137	20	0.13
Inner	194	180	-8	0.87
Inertinite[c]				
Benzene-like	223	149	17	0.39
Substituted	231	161	46	0.07
Inner	204	192	-30	0.54

a. ppm from TMS.

b. Based on total aromatic carbon present.

c. Semi-fusinite from Aldwarke Silkstone coal (Great Britain). The sample is described in reference 6.

FIGURE CAPTIONS

FIGURE 1. Chemical shielding tensors of aromatic carbons. The characteristic shapes are used to fit overlapping tensor elements. The narrow isotropic line obtained by magic angle spinning is also shown for purposes of clarity.

FIGURE 2. The static spectrum (top) of 1,2,3,6,7,8 hexahydropyrene. The individual tensors for the three different types of carbons are shown (bottom) together with the composite pattern. This theoretical fit of the data is superimposed in the top of the figure. Only the simulated aromatic carbon tensors are shown.

FIGURE 3. The tensor for a substituted aromatic carbon is simulated as a function of θ, the spinning axis relative to the magnetic field. The VASS experiment can be used to scale the position of the tensor components σ_{11}, σ_{22}, and σ_{33}. At the magic angle, $\theta = 54.7°$, the components converge to the isotropic value.

FIGURE 4. VASS spectra of 1,2,3,6,7,8 hexahydropyrene together with the simulated spectra arising from the aromatic carbons.

FIGURE 5. Experimental and simulated spectra of an anthracite coal. The two tensor fit gives near ideal correlation and the population factor for the benzene like tensor is within experimental error of the H/C value.

FIGURE 6. VASS spectra of Aldwarke Silkstone inertinite maceral (fusinite). The simulated spectrum of the aromatic carbons (bottom) is used to portray the population factors. The simulated aromatic carbon spectra at 43° and 72° are overlaid on the experimental data.

CSA
(aromatic carbons)

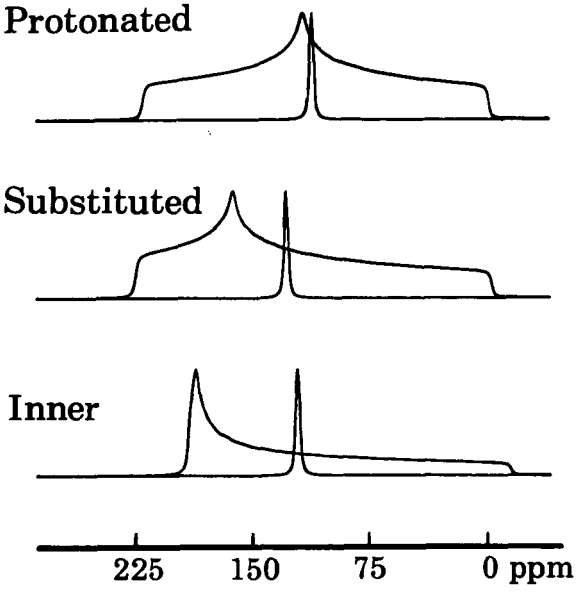

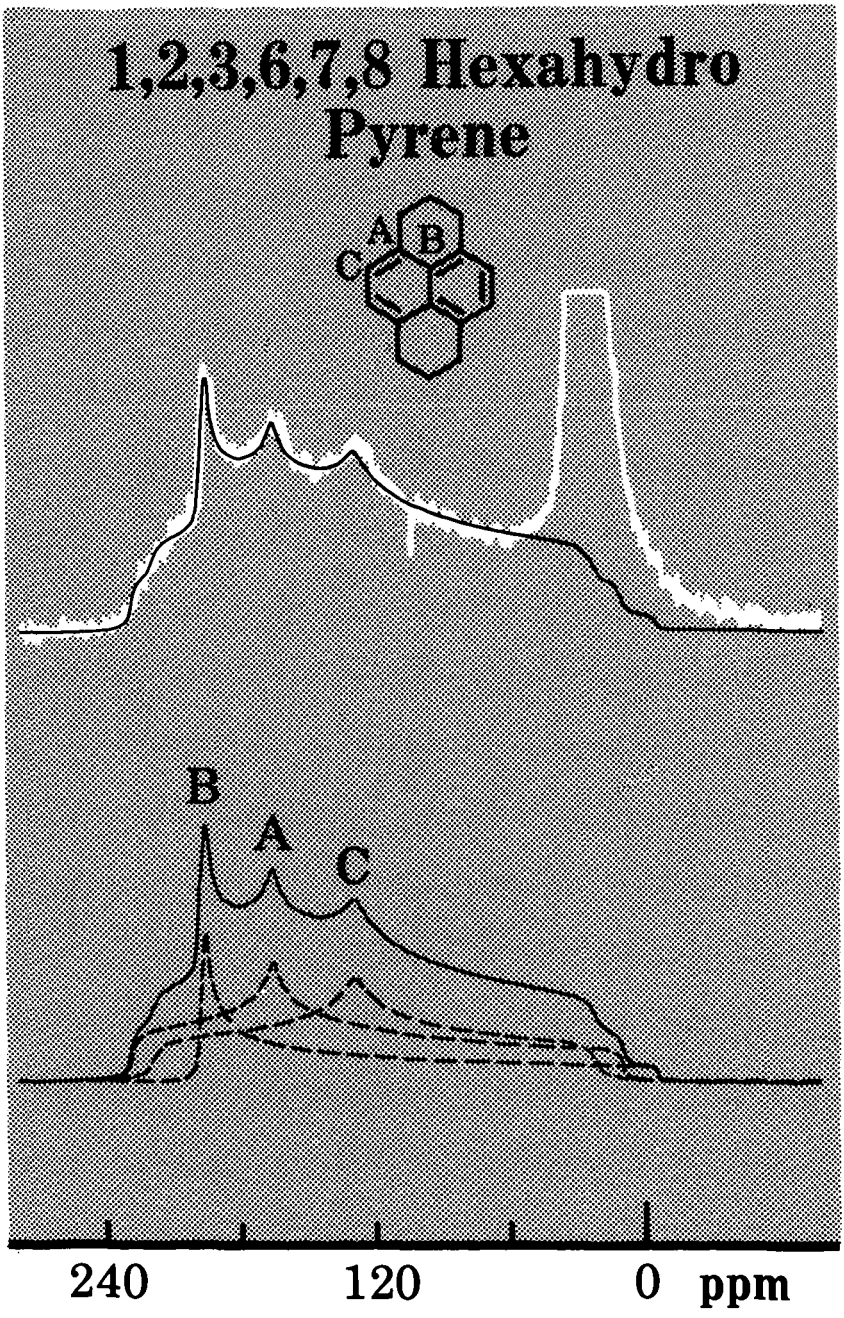
1,2,3,6,7,8 Hexahydro Pyrene
A
B
C
B
A
C
240
120
0 ppm

VASS

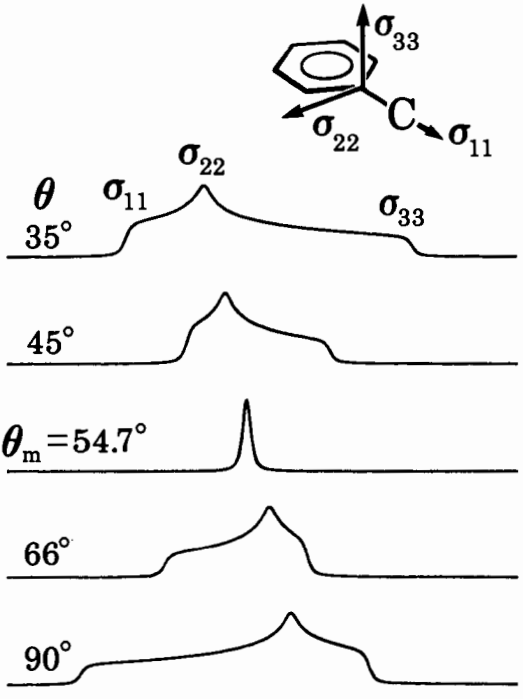

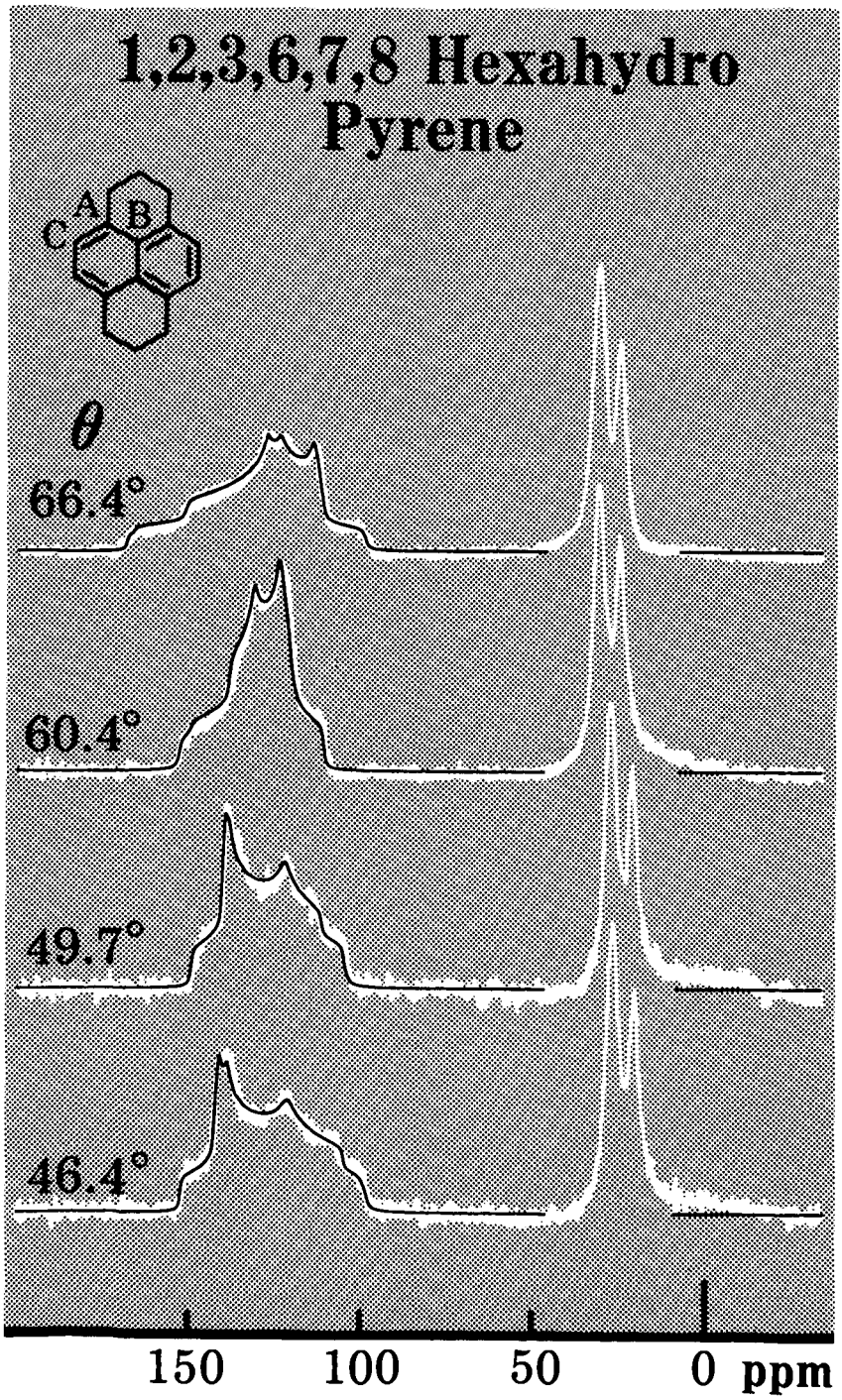
1,2,3,6,7,8 Hexahydro Pyrene
A
B
C
θ
66.4°
60.4°
49.7°
46.4°
150
100
50
0 ppm

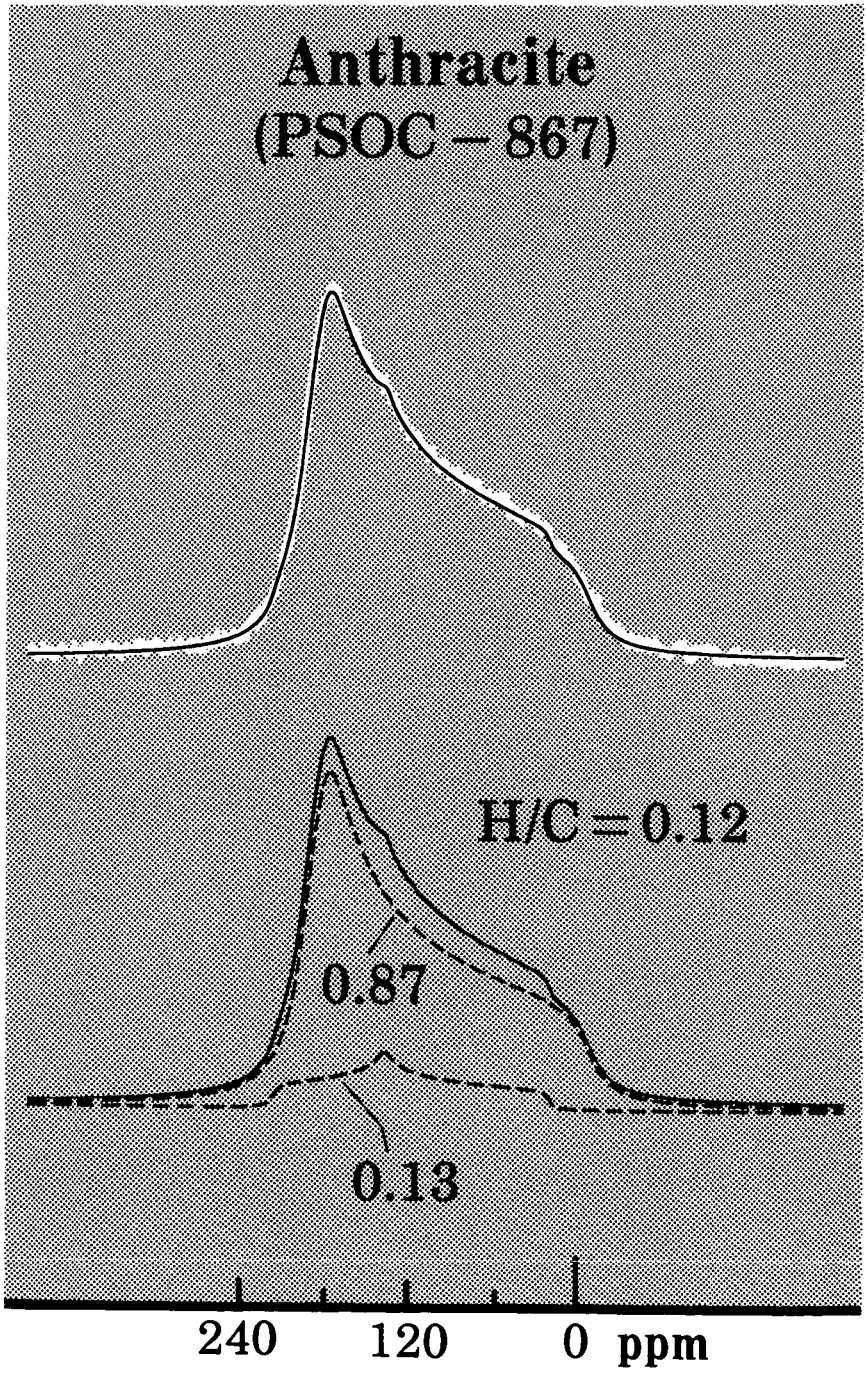
Anthracite
(PSOC – 867)
H/C = 0.12
0.87
0.13
240
120
0 ppm

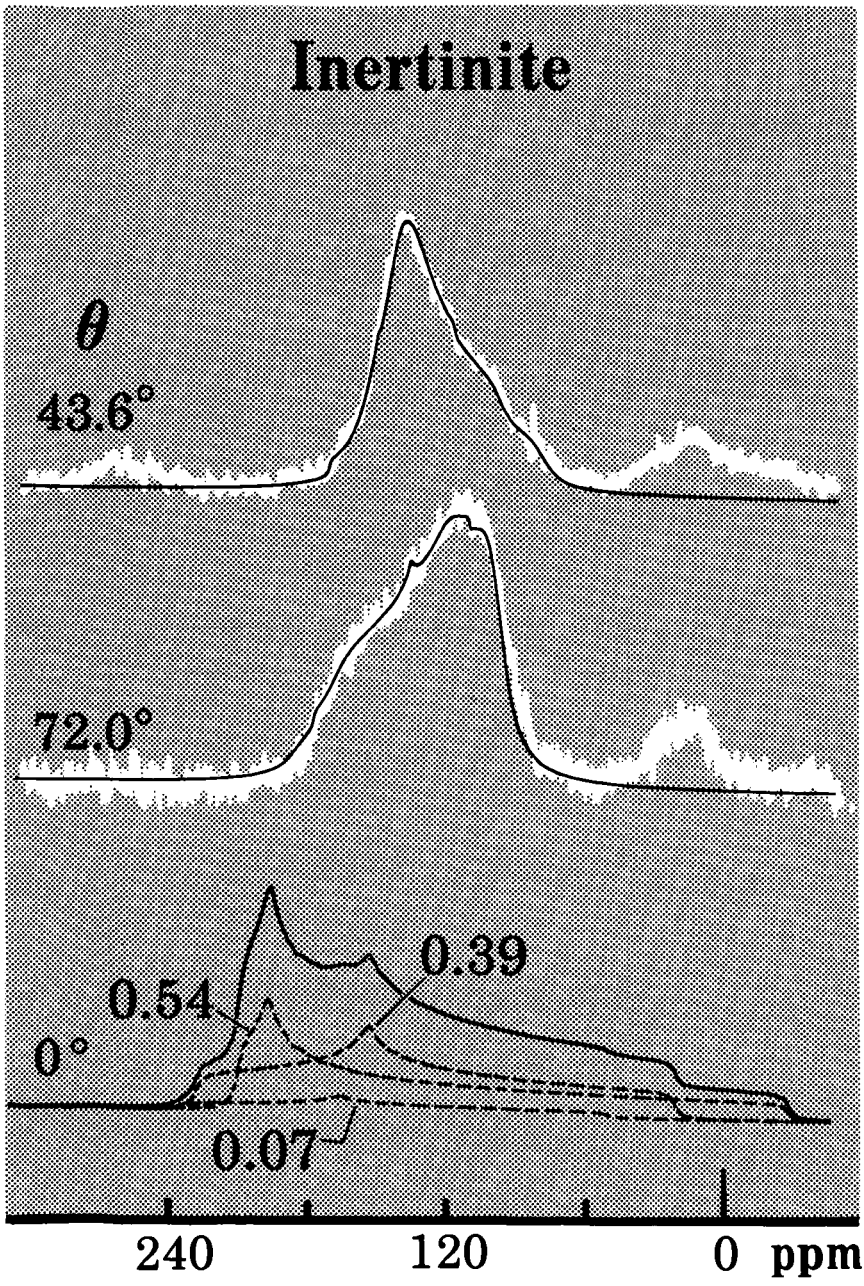
Inertinite
θ
43.6°
72.0°
0°
0.54
0.39
0.07
240
120
0 ppm

AN EXPERIMENTAL SIMULATION OF CROSSFLOW COAL GASIFICATION

M. Gallagher, J. Zondlo, E. Johnson, and E. Monazam
College of Engineering
West Virginia University
Morgantown, WV 26506-6101

ABSTRACT

A novel combustion test-pot facility was constructed and operated so as to simulate crossflow coal gasification with steam at ambient pressure. The test pot was fully instrumented to allow transient measurements of pressure drop, weight change of the bed, and product gas composition. In addition, the temperature front within the bed was tracked as a function of both time and position. Experiments were conducted at different air and steam flow rates in a packed particle bed of coke. The weight of an average coke charge was approximately 35 pounds and the fuel utilization rate ranged between 7.8 and 22 lb/ft^2-hr. Based on the experimental results, energy and mass balances were performed and closed to about 90%. Data obtained were used to verify a computer simulation of the process.

1. INTRODUCTION

The most common commercial coal gasification system in use today is the counter-flow moving bed system. In this system, the coal feestock moves downward and passes through four idealized zones in the gasification process. These zones in order from the top to the bottom of the bed are drying, pyrolysis, gasification and combustion. However, most moving-bed units are size-limited and several must be operated in parallel for larger throughputs.

An alternate approach to the design of a large-scale coal gasification system would be to borrow established technology from a similar process. One such process has long been utilized to sinter iron ore and produce a "strong clinker" suited for feed stock in a blast furnace. The sintering machine most commonly used today is a modification of the Dwight-Lloyd continuous sintering machine, formerly used only in the lead and zinc industry [1]. Originally developed in the early 1900's, the machine consists of a strong structural steel frame supporting two large gears and steel tracks. A system of pallets, or trays, with perforated bottoms is driven by these gears at a speed of 1 to 3 feet per minute. The sintering machine for iron ore may be 6 to 12 feet wide by 90 to 168 feet in length with pallets to hold the charge. Underneath the pallet train is a series of suction boxes which are connected with a fan to induce a downdraft through the perforated bottom and ore charge. Located at the input of the machine is a burner which serves to initiate the sintering process by igniting the top layer of charge. The charge is typically a mixture of ore particles up to 1/4-inch in diameter, flux, to aid in the agglomeration, and fuel, such as coke. The charge layer may be 6 to 12 inches deep. The largest machines will treat as much as 4500 tons of ore per day.

The possible application to coal gasification would be the replacement of the ore charge with coal [2]. The coal particles up to 1/4-inch in diameter would be placed on another layer of inert material, such as limestone, roughly 1/2-inch in diameter. This inert material would serve to protect the grate thermally, support the smaller coal particles, trap out particulates and possibly aid in sulfur removal from the product gas stream.

The main objectives of the work presented here were the design, construction and start-up of an experimental appratus that would effectively simulate the crossflow process. The independent variables such as air temperature and flow rate, and relative humidity of the air feed were selectively examined to determine their effect on the exit gas composition and fuel utilization rate. These data will assist in determining the reliability of the experimental test-pot system and its potential for use in future experimental and modelling efforts.

II. EXPERIMENTAL APPARATUS

A flowsheet of the proposed test-pot facility is shown in Figure 1. Ambient air, fed from a ring compressor, was preheated and humidifed before it entered the combustion pot. An orifice plate served as an air flowmeter, while the air was preheated using a steam heater. Supply steam at 30 psig was regulated, using a Kaye MacDonald regulator, to the pressure required to obtain the desired heater temperature. The air was humidifed by direct injection of saturated steam. The temperature and relative humidity (RH) of the feed air were measured as the air entered the combustion pot using an Omega RH-20F hygrometer. This instrument is capable of reading temperatures to 175°F ± 0.5°F and relative humidity to 95% ± 2%. The humidity measurement was backed with a Hygrodynamics L4-4822W sensor and L15-3050 Universal Indicator capable of reading to 98% RH ± 1.5%. After the product gas exited the test pot, a sample was taken for analysis and the remainder combusted in an afterburner.

The test pot itself is shown in Figure 2. It consists of a 24-inch o.d. steel pipe, 1/2-inch thick wall, with a 1/8-inch thick stainless steel plate welded to the bottom. The plate is perforated with 3/8-inch diameter holes located on 1/2-inch triangular centers. The pipe is lined with 5 inches of insulation brick refractory, resulting in an inside bed diameter of 13 inches. Pt vs. Pt 10% Rh thermocouples (TC) are placed at 2-inch intervals above a 6-inch layer of non-combustible material. The thermocouples are rated to 3000°F and can be used in oxidizing or reducing atmospheres. The temperature in the coal bed is monitored automatically as a function of time as well as position by means of a Doric Digitrend 220 data logger.

Operating at near atmospheric pressure, the test pot is free-hanging while the transient weight change of the coal is recorded utilizing a load cell. The load cell is a Sensotec model RM-1K, hermetically sealed to withstand humid and corrosive environments and temperature compensated to 160°F. It has a range of 0 to 1000 pounds mass and its stated accuracy is ± 0.2% of full scale or ± 2 pounds. A Sensotec 450D digital readout with a 0-5 volt recorder output is used in conjunction with the load cell. The separation between the inlet and outlet of the pot is maintained by a water seal which allows the test pot to hange freely and still maintain the division between the inlet and outlet of the bed.

a) Experimental Procedure

The bed was charged with 35 pounds of coke, resulting in a coke bed density of 38 lb/ft^3. Coke, the devolitalized product of coal, was selected as the feedstock for the initial tests as it would produce a less complex gasification product, free of tars and volatile material. For a typical experimental run, the procedure is as follows. The air, fed at 25 CFM and 77°F, is heated to 140°F and humidifed to near 100% RH before entering the combustion pot. The air feed is started first and allowed to reach steady state at which point the fuel charge is ignited with charcoal placed at the top of the charge. Ignition of the fuel occurs within 5 to 10 minutes. The data logger is used to record the temepratures at specific time intervals, initially every

minute. The weight change with time as monitored by the load cell is also recorded continuously with a strip-chart recorder. Finally, gas samples from the outlet of the test pot are taken at specific time intervals, every 10 minutes, and analyzed with a gas chromatograph (GC). The GC is a Gow-Mac Series 550 thermal conductivity-type gas chromatograph equipped with a gas sampling valve, series/by-pass column switching valve, one 5A molecular sieve column and one Porapak Q column. The run is considered finished when the combustion front reaches the bottom of the bed. This is tracked via the thermocouples placed at intervals within the depth of the bed, and is also indicated by abrupt changes in the gas composition and the pressure drop across the bed.

III. RESULTS

a) Product Gas Composition

Samples of the product gas were withdrawn from the bottom of the combustion pot at approximately 10 minute intervals. The GC was configured for the detection of N_2, CO_2, H_2, CH_4, CO and O_2. A representative composition/time profile is shown in Figure 3. After an initial transient period (around 20 minutes for the run in Figure 3), the product gas composition remains essentially constant for the duration of the test. The onset of breakthrough is signalled by an abrupt increase in the N_2 composition late in the run. A typical product gas contained roughly 20% CO_2, 10% CO, 10% H_2, 2% CH_4 and 60% N_2. The GC was checked before and after each run with a standard calibration gas obtained from Supelco, Inc.

b) Weight Change

The transient weight of the bed provided the data necessary to calculate the fuel utilization rate and the rate of progression of the combustion front. Representative data for a typical run are shown in Figure 4. This data, used in conjunction with the transient pressure drop across the bed, permitted the actual weight change with time to be determined.

In all cases, the weight change profiles showed an initial period in which the weight of the bed remained relatively constant, followed by a uniform decrease in weight until the end of the run. The slope of this line when divided by the cross-sectional area of the bed yielded the fuel utilization rate at the conditions of the experiment. This was found to vary from 7.8 lb/ft^2-hr at the lowest air flow rate to 22.1 lb/ft^2-hr at the highest air flow rate. These values are well within the range of those reported for the Wellman-Galusha gasifier with a coke fuel [3]. Comparable results were also found by Essenhigh who reported fuel utilization rates of 5 to 25 lb/ft^2-hr under similar experimental conditions [4].

The fuel utilization rate when multiplied by the density of the packed bed yielded the rate of progression of the combustion front which ranged from 0.06 to 0.13 inches per minute.

c) Temperature Profiles

The temperature profiles of a typical experimental run are shown in Figure 5. Such data are useful in determining the progression of the combustion and gasification zones through the bed. A sharp increase in temperature in the early stages followed by a peak as the combustion zone passed, and finally a decrease in slope as the gasification zone passed, are characteristics of all the profiles.

The temperature profiles were used as an alternate method for calculating the

progression of the combustion front through the bed by measuring the time between the temperature maxima at each thermocouple location. The progression of the combustion front determined in this manner was compared with the progression as determined from the weight change data as a check of the load cell instrumentation and as a check on the evenness of the burn. Good agreement was seen in the progression of the combustion front as determined by each method. This would indicate that the combustion front of the fuel bed is burning in a relatively uniform, plug-flow manner.

d) Mass and Energy Balances

The calculation of the mass and energy balances was done as a check of the overall performance of the instrumentation.

The mass balance focused primarily on the carbon present in the charge. In order to calculate the carbon balance, it was necessary to obtain the inlet gas flow rate and composition, the outlet gas flow rate and composition, and the length of time the run was in progress. From this information the mass of carbon present in the exit gas could be determined and compared to the mass of carbon that was consumed as calculated from the weight change. Such a balance resulted in closure to over 90% in most cases, indicating that the instrumentation was functioning adequately for the intended purpose.

The energy balances also showed good results, usually accounting for over 90% of the energy released from the coke fuel. Approximately 50% to 55% of the energy leaves the bed in the form of combustables in the product gas. The heat losses to the system were 20% of the energy available, while the energy carried as sensible heat in the product gas accounted for approximately 20% as well. These results are encouraging in showing that the instrumentation and the experimental system are operating reliably.

IV. DISCUSSION

For the Wellman-Galusha gasifier with a coke fuel the CO and H_2 concentrations observed in the product gas are 29 mol% and 15 mol% respectively [3]. The data collected from the test pot came to only 50% to 60% of those for the Wellman-Galusha gasifier. Moreover, the heating value reported for the Wellman-Galusha was 130 BTU/ft^3; the crossflow product gas was only 80 BTU/ft^3. Also, Essenhigh reports CO concentrations of 23 mol% for his similar test-pot studies using a coke fuel [4]. He does not report a value for hydrogen. In an associated modelling effort, both the results of the test pot and the other workers could be predicted by including a reactivity factor in the rate equations to account for variations in feedstock characteristics [5]. Thus differences in product gas composition may reflect variations in the physical and chemical characteristics and hence reactivity of the feedstock.

The test pot responded to changes in air feed to the bed as expected. Under the same steam feed conditions, higher air flow rate resulted in higher combustion temperature and a shorter run time. The test-pot also responded as expected to changes in the steam feed to the bed. High steam rates resulted in lower temperatures in both the combustion and gasification zones. This in turn affected the product gas compositions by suppressing CO production and increasing H_2 production. The lower combustion and gasification temperatures also allowed for more uniform heating of the bed and a more defined and stable gasification zone. Conversely, low steam flows yielded higher combustion and gasification temperatures, with CO production favored and H_2 suppressed.

It should also be noted that CO_2 generated in the combustion zone is not being completely converted to CO as it passes through the gasification zone. Low temperature, short residence time, gas channeling, clinker formation or low fuel reactivity are possible factors affecting conversion.

V. CONCLUSIONS

The fuel utilization rates for this system were comparable to those for the Wellman-Galusha gasifier [3]. The carbon mass balance resulted in over 90% closure in most cases, a result which is consistent with that reported by other researchers in the gasification area [3,4]. The energy balances show approximately 50% of the energy leaves the gasifier in the form of combustables. Another 20% of the energy leaves in the form of sensible heat and roughly 20% is lost to the system.

Based upon the data collected and the mass and energy balances performed, the experimental test pot system operated reliably and produced good data.

REFERENCES

1. Kirk-Othmer Encylopedia of Chemical Technology, Third Edition, John Wiley & Sons, New York, Volume 24, p. 816, 1980.

2. Gallagher, M. A., M. S. Thesis, Department of Chemical Engineering, West Virginia University, Morgantown, WV, 1986.

3. Probstein, R. F. and Hicks, R. E., Synthetic Fuels, McGraw-Hill, New York, pp. 95-107, 1982.

4. Eapen, T., Blackader, R., and Essenhigh, R. H., "Kinetics of Gasification in a Combustion Pot: A Comparison of Theory and Experiment," Proceedings of the 16th Symposium on Combustion, Pittsburgh, PA p. 515-522, 1977.

5. Monazam, E. R., Ph.D. Dissertation, Department of Mechanical & Aerospace Engineering, West Virginia University, Morgantown, WV 1986.

This work was funded in part by the State of West Virginia through the Energy Research Center at West Virginia University.

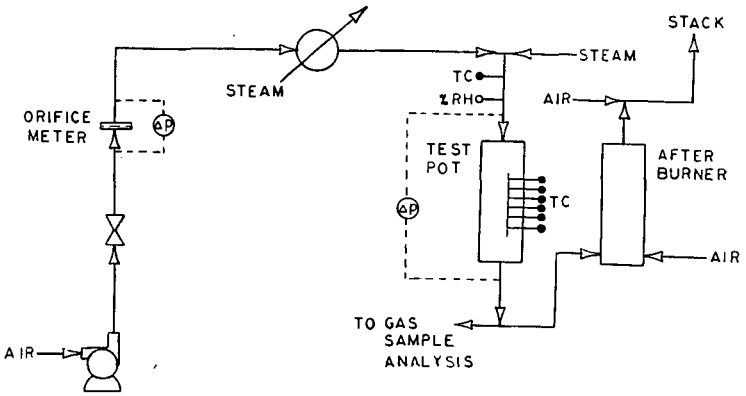

Figure 1. Overall flowsheet of crossflow coal gasification test pot facility.

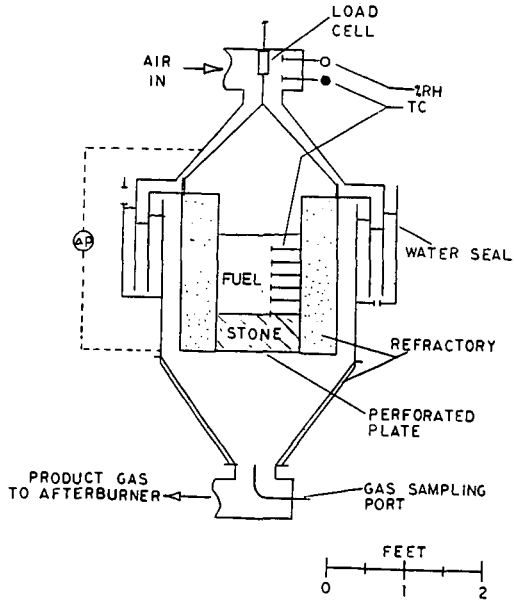

Figure 2. Cross-sectional view showing details of experimental test pot.

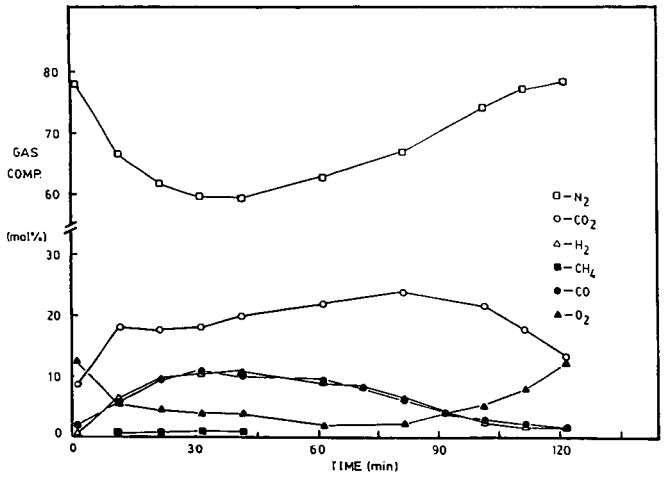

Figure 3. Representative composition/time profiles for major components in product gas stream.

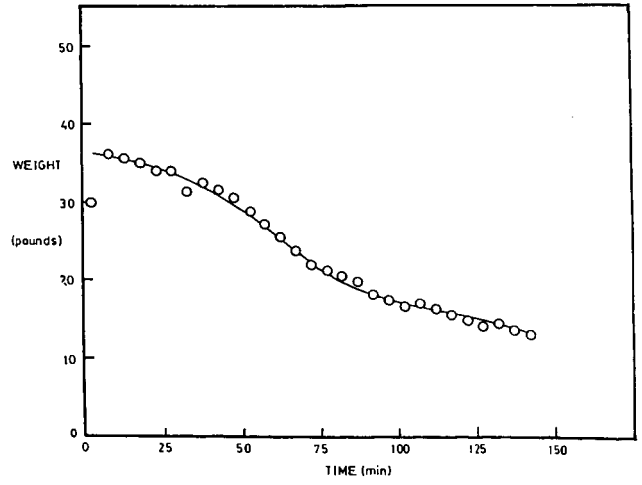

Figure 4. Transient weight change of coke charge for a typical gasification test.

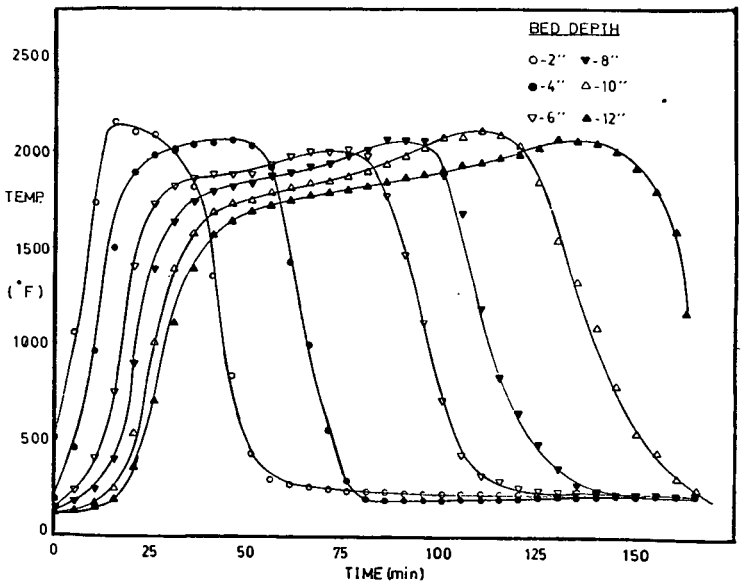

Figure 5. Transient temperature profiles at varous bed depths as measured from the top of the bed.

MODELING OF HYDROGASIFICATION OF A SINGLE LIGNITE CHAR PARTICLE

G.P.Sakellaropoulos, G.Skodras, S.P.Kaldis,
G.G.Stavropoulos and P.S.Kokorotsikos

Department of Chemical Engineering and
Chemical Process Engineering Research Institute
Aristotle University of Thessaloniki
Thessaloniki, Greece 54006

INTRODUCTION

Gasification, devolatilization, combustion and other coal conversion processes are quite complex, involving numerous, not well defined reactions, and simultaneous physical structure transformations. In order to describe these phenomena, several efforts have been reported, based either on empirical kinetic expressions (1-5) or on theoretical models (6-12). In the former, rate expressions are given in terms of volatile species, residual and active carbon, and reactant gas concentration or pressure. Theoretical models attempt to couple reaction rates with mass and heat transfer processes. The various models, however, differ significantly from each other, because of the diversity of the chemical and physical phenomena which they describe (e.g. pyrolysis, combustion, steam gasification etc) and the differences in assumptions and simplifications involved in each one.

Fast coal processes, such as oxygen combustion, rapid pyrolysis and devolatilization are usually considered to proceed via a shrinking core model, either isothermally or non-isothermally (6-11). Mass transport limitations are often assumed to occur within a reacted shell, surrounding a coal particle (6-7). The pore structure of the reacting particles is considered unchanged, in most of these models (6-9), although the effect of pore size distribution has been examined (8).

Structural variations of coal with reaction time have been included in few models, such as in hydropyrolysis of softening coals (10), in coal-oxygen reactions (11) and in char gasification (12). In a comprehensive analysis of coal combustion models, Sotirchos and Amundson (11) considered only the macropores of coal. Thus, local conversion and pore structure depended only on the thermal gradients at various total conversions. Lee at al. (12) developed a char gasification model, in which Knudsen diffusion (in the micropores), as well as pore structure variations due to carbon consumption, were included. However, only one reaction was considered to take place, with CO_2 as a gasifying medium. This model simplifies the reaction network, ignoring the participation of an active carbon species and also the product mass transfer and the reactant accumulation. These simplifications yield an analytical solution, at pseudosteady state conditions.

The model proposed here considers the physical and chemical processes occuring in a gasifying single particle and correlates the predicted results with experimental macroscopic data. An active carbon species is assumed (13) to react in two parallel steps to form a gaseous product or stabilized char (coke). Reactant and product diffuse in and out of the particle while the local micropore structure can vary due to carbon reaction and consumption. The model permits estimation of the local radial distribution of reactant and product concentrations, reaction rates, surface areas and porosities with time. Global properties, such as product yields, surface area and porosity are also calculated, for comparison with the corresponding experimental quantities. The model is applied here to coal hydrogasification, a process which has received less attention compared with steam or CO_2 gasification.

FORMULATION OF THE MODEL

A single spherical lignite or coal particle, of radius r_o, is considered to undergo hydrogasification, after initial rapid devolatilization. During this initial stage, a measurable, uniform pore structure, and an assumed hydrogen profile have developed within the particle. The following assumptions apply to the model formulation:
- Isothermal reaction in a uniform, constant hydrogen atmosphere.

- Constant particle size, with uniform radial pore structure distribution initially (t=0).
- Negligible film diffusion resistance around the particle.
- Predominantly micropore structure for the particle.

Char hydrogasification involves an active carbon species, which, with hydrogen yields methane, or by crosslinking results in coke formation and carbon stabilization:

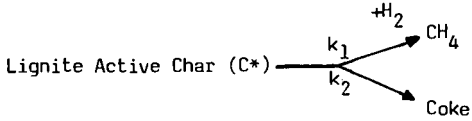

1a)

1b)

From available rate expressions for CH_4 and coke formation (13), the instantaneous, local reaction rates within the particle are given by Equations 2 and 3.

$$R_{CH_4}(r,t) = k_1^o \exp(-\frac{E_1}{RT})\ \rho_p S_g\ C_{C^*} C_{H_2} \qquad 2)$$

$$R_{Coke}(r,t) = k_2^o \exp(-\frac{E_2}{RT})\ \rho_p S_g\ C_{C^*} = \frac{dC_{coke}}{dt} \qquad 3)$$

Reactant (H_2) and product (CH_4) counter diffuse through the porous particle matrix which varies with time and location due to reaction. Thus, the continuity equation for the two gaseous species gives:

$$\frac{\partial C_{H_2}}{\partial t} = \frac{1}{r^2}\frac{\partial}{\partial r}(r^2 D_{e,H_2}\frac{\partial C_{H_2}}{\partial r}) - 2R_{CH_4}(r,t) \qquad 4)$$

$$\frac{\partial C_{CH_4}}{\partial t} = \frac{1}{r^2}\frac{\partial}{\partial r}(r^2 D_{e,CH_4}\frac{\partial C_{CH_4}}{\partial r}) + R_{CH_4}(r,t) \qquad 5)$$

The effective diffusivities ($D_{e,j}$) can be related to the Chapman-Enskog diffusivity (D_{H_2/CH_4}) and the Knudsen diffusivity into the micropores (D_k), (14), by

$$D_{e,j} = (\frac{I}{D_{12}} + \frac{1}{D_k})^{-1}\ \varepsilon^2 \qquad 6)$$

Weight (m) loss and increase of surface area (S_g) and porosity (ε) of the particle occur because of the first reaction, 1a, and, thus, they can be correlated with the conversion to methane (X_{CH_4})

$$\varepsilon = 1 - (1 - X_{CH_4})\ (1 - \varepsilon_o) \qquad 7)$$

$$m = m_o + \frac{4}{3}\pi r^2\ \rho_t(\varepsilon_o - \varepsilon) \qquad 8)$$

$$\rho_p = \rho_t\ (1 - \varepsilon) \qquad 9)$$

Relation 6, between bulk (ρ_p) and true (ρ_t) particle density, is valid for non-swelling or -shrinking particles of constant size. For moderate conversions, the surface area may be assumed to vary linearly with porosity (15)

$$S_g = S_o\ \varepsilon \qquad 10)$$

This system of non-linear partial differential equations was converted to a system of dimensionless non-linear algebraic equations by the explicit finite difference method. Equation 2-4 and 6-10 were solved iteratively, using the Brown technique (16) and the appropriate boundary conditions for C_{C*}, ϵ, C_{H_2} below. Solution of Eq. 5, with the pertinent B.C. for C_{CH_4} below, gives the methane distribution in the particle.

$$\text{At } t = 0 \text{ and } 0 \leq r \leq r_o \qquad \begin{cases} C_{C*} = C_{C_o^*} \\ \epsilon = \epsilon_o \\ X_{CH_4} = 0 \\ X_{coke} = 0 \end{cases}$$

$$t > 0 \text{ and } r = r_o \qquad \begin{cases} C_{H_2} = C_{H_2,S} \\ C_{CH_4} = 0 \end{cases} \qquad 11)$$

$$t > 0 \text{ and } r = 0 \qquad \begin{cases} \frac{\partial C_{H_2}}{\partial r} = 0, \quad \frac{\partial C_{CH_4}}{\partial r} = 0 \end{cases}$$

All char carbon ($C_{C_o^*}$) is considered reactive, as indicated by its complete conversion in high pressure experiments. Since hydrogasification occurs after initial rapid hydropyrolysis (17), some hydrogen profile is expected within the particle matrix. Thus, instead of the conventional boundary conditions for hydrogen, a simple linear initial profile has been assumed and tested

$$\text{At } t = 0 \text{ and } 0 \leq r \leq r_o \qquad C_{H_2} = \frac{r}{r_o} C_{H_2,S} \qquad 12)$$

A linear, or perhaps a parabolic, hydrogen profile should be more realistic, since hydrogen has penetrated into the pores during the first stage. Alternatively, a uniform zero hydrogen concentration may be assumed ($C_{H_2} = 0$ at $t = 0$, $r \leq r_o$), or even a uniform concentration equal to the bulk one ($C_{H_2} = C_{H_2,S}$ at $t = 0$, $r \leq r_o$).

Parameter values were obtained either experimentally or from the literature. Values of k_1^o, E_1, S_o, ϵ_o and ρ_t were measured at 800 - 950°C, while k_2^o and E_2 are experimental values reported in reference (18). The following values were used

E_1 = 35600 cal/mol
E_2 = 28600 cal/mol
k_1^o = 1.7x10^{-6} m^4/mol·min
k_2^o = 3.77x10^{-7} m/min
ρ_t = 1.42 gr/cm^3

S_o^{800} = 355 m^2/g
S_o^{850} = 388 m^2/g
S_o^{900} = 395 m^2/g
S_o^{950} = 410 m^2/g

ϵ_o^{800} = 0.17
ϵ_o^{850} = 0.175
ϵ_o^{900} = 0.18
ϵ_o^{950} = 0.19

EXPERIMENTAL

Lignite hydrogasification experiments, to obtain kinetic parameters and macroscopic, global properties, were performed in a TGA (DuPont 99) system and in an isothermal, tubular reactor (17, 19). Products were continuously analyzed by GC and IR. Pore structure, porosity, density and surface area of lignite chars, at various times and temperatures, were characterized by multipoint BET, helium pycnometry, CO_2 and N_2 adsorption (20).

RESULTS AND DISCUSSION

The model formulated above has been solved using a simple, linear profile for the initial concentration of hydrogen within the particle. Solution has been obtained at eleven radial positions for a time period of 30 min using a time increment of one minute. The results permit estimation of non-measurable quantities, such as the temporal-radial distribution of (a) hydrogen, methane and coke concentration; (b) porosity and surface area; and (c) local rates of methane and coke formation, under various reaction conditions. Integration of predicted results over the whole particle yields global properties, such as particle weight loss, methane yield and rate of formation, total porosity and surface area.

Comparison of predicted and measured macroscopic properties should establish first the adequacy of the model to describe the chemical and physical processes. Figure 1 shows calculated and experimental values of carbon conversion to methane at various times and temperatures. In most cases, agreement is good. Some deviation of experimental data, especially at high temperatures, may arise from a number of reasons, e.g. different initial hydrogen profile, slightly higher order in H_2 for reaction 1a, or higher k_2 and E_2 values than those obtained from the literature for the crosslinking and carbon stabilization reaction.

Similarly, the predicted development of total particle surface area and porosity is in good agreement with the measured physical properties up to 30-40 min, Figures 2 and 3. One should note, here, that Equations 7 - 10 of the model assume a linear growth of surface area and porosity, directly proportional to carbon conversion to methane. Pore blockage, because of carbon stabilization and crosslinking, is not currently considered in the model. This phenomenon may explain the decline of S_g and ε at prolonged times.

After the above macroscopic comparison of model and experimental results, a microscopic examination should unravel the transformations that a lignite particle undergoes during hydrogasification. Figure 4 shows the anticipated hydrogen concentration profile in the particle, at various times. If the initial (t=0) hydrogen concentration is assumed to vary linearly with radius, C_{H_2} in the pores increases with time; however, it always remains less than the bulk one, because of partial consumption of H_2 to form methane and counter-diffusion of the product. The hydrogen concentration in the pores is also expected to increase (albeit somewhat slower) in the case of uniform, zero C_{H_2} initially. If at t=0, $C_{H_2}=C_{H_2,S}$, hydrogen diffuses into the pores faster than it reacts and its concentration remains constant with time.

Methane is produced by reaction of active carbon with H_2 and diffuses out of the gasifying particle. Its concentration distribution radially can be predicted by this model, as shown in Figure 5. At the outer layers of the particle, the high local C_{H_2} results in high carbon-to-CH_4 conversion and, thus, methane concentration increases. The decline of CH_4 at the surface ($r=r_o$) is caused by the assumption that methane is so diluted in the bulk stream that its bulk and surface concentration is virtually zero. Methane concentration in the particle increases with time because of C_{H_2} increase, cf. Fig. 4.

Carbon consumption to form gaseous methane should increase the number and size of pores within the particle, dependent on rate. If the "specific surface area", S_g, is used as an approximate, lumped measure of pore structure development, a surface area radial distribution can be predicted, Figure 6. This area increases, from the center of the particle outwards, because of the higher H_2 concentration and rate in the outer shells. Since C_{H_2} increases with time within the particle, S_g also increases, to a substantial difference of ~ 50 m^2/g between surface and center at 30 min reaction time. A similar trend is predicted for the local "porosity", ε, radially with time.

The calculated local values of C_{H_2}, S_g, ε permit estimation of the local reaction rate for methane formation at any time, Figure 7. Rate increases outwards, following a trend analogous to C_{H_2} and S_g. Around the center of the particle, C_{H_2} increase with time results in significant increase of R_{CH_4} after 30 min. Near the surface, R_{CH_4} is affected by the surface area increase (cf. Fig. 6), since C_{H_2} there changes little (Fig. 4).

Figure 7 and Equation 2 indicate that hydrogasification is sensitive to H_2

partial pressure. Thus, recycle of the reactant stream without prior separation of product could affect rates in the pores significantly. Figure 8 shows a drastic decrease of methane formation rate within a gasifying particle, at 5 min. With $P_{CH_4} : P_{H_2} = 1 : 1$ in the bulk stream, rates drop to almost zero for $r < 0.5\ r_o$, and to less than 15 % of that for pure H_2, at r_o. Integration of these curves with location and time show that carbon conversion to methane at 900°C should drop from ~6% in pure H_2 to ~1% at $P_{H_2} = 0.5$ atm.

The model described here takes into account a realistic, two path reaction scheme for hydrogasification, with simultaneous variation of the pore structure properties of the gasifying char particle. Porosity and surface area do not develop uniformly, within the particle, with time and this affects hydrogen penetration, methane counter-diffusion and, thus, the microscopic and global rate of gasification. The model predicts succesfully experimental macroscopic quantities, up to 30-40 min of gasification. Beyond this time, carbon stabilization and pore blockage may cause some deviation. The use of the model can be easily extended to noncaking coals other than lignite and to other gasification media such as CO_2 or steam.

ACNOWLEDGEMENT

The authors wish to thank the European Coal and Steel Community and the Chemical Process Engineering Research Institute of Thessaloniki for financial support of this work.

LIST OF SYMBOLS

C^*	Active carbon concentration (mol/m^3).
C_{CH_4}	Intraparticle methane concentration (mol/m^3).
C_{H_2}	Intraparticle hydrogen concentration (mol/m^3).
$C_{H_2,S}$	Bulk hydrogen concentration (mol/m^3).
$D_{e,j}$	Effective diffusivity of species j (H_2 or CH_4) (m^2/s).
D_{12}	Chapman-Enskog diffusivity (m^2/s).
D_k	Knudsen diffusivity (m^2/s).
E_1, E_2	Activation energies of methane and coke formation (cal/mol).
ϵ	Porosity of particle.
I	Binary diffusivity coefficient (0.25 for D_{e,H_2} and -0.5 for D_{e,CH_4}).
k_1^o, k_2^o	Rate constants of methane and coke formation.
m	Particle mass (g).
ρ_p	Bulk density of particle (g/cm^3).
ρ_t	True density (g/cm^3).
r	Particle radial coordinate (μ).
r_o	Particle radius (μ).
R	Universal gas constant (1.987 cal/mol K).
R_{CH_4} (r,t)	Rate of methane formation (mol/m^3 min).
R_{coke} (r,t)	Rate of coking reaction (mol/m^3 min).
S_g	Specific surface area (m^2/g).
T	Temperature (K).
t	Time (min).
X_{CH_4}	Methane conversion.

Subscripts

o	Initial values at t = 0.
s	Bulk stream and particle surface property.

REFERENCES

1. Moseley F. and Paterson D., J. Inst. Fuel., 38, 13, (1965).
2. Johnson J.L., Adv. Chem. Ser., 131, 145, (1974).
3. Wen C.Y. and Huebler J., Ind. Eng. Chem. Process Des. Dev. 4, 142, (1965).
4. Schmal M., Monterlo J.L.F. and Castellan J.L., Ind. Eng. Chem. Process Des. Dev. 21, 256, (1982).

5. Anthony D.B. and Howard J.B., AIChE J., 22, 625, (1976).
6. Arri L.E. and Amundson N.R., AIChE J., 24, 72, (1978).
7. Russel W.B., Savill D.A. and Greene M.I., AIChE J., 25, 65, (1979).
8. Gavalas R.G. and Wilks K.A., AIChE J., 26, 201, (1980).
9. Bliek A., Poelje W.M., Swaalj W.P.M. and van Beckum F.P.H., AIChE J., 31, 1666 (1985).
10. Shaub G., Peters W.A. and Howard J.B., AIChE J., 31, 903, (1985).
11. Sotirchos S.V. and Amundson N.R., AIChE J., 30, 537, (1984).
12. Lee S., Angus J.C., Edwards R.V. and Gardner N.C., AIChE J., 30, 583, (1984).
13. Zahradnik R.L. and Glenn R.A., Fuel, 50, 77, (1971).
14. Walker Jr., P.L., Rusinko Jr., F. and Austin L.G., Adv. Catal., 11, 133, (1959).
15. Hill, Jr., C.G., "An Introduction to Chemical Engineering Kinetics and Reactor Design" J.Wiley, N.Y. (1977), pp 434.
16. Brown K.M., Comm. ACM, 10, 728, (1967).
17. Kokorotsikos P.S., Stavropoulos G.G. and Sakellaropoulos G.P., Fuel, 65, 1462, (1986).
18. Banerjee D.K., Laidler K.J., Nandi B.N. and Patmore D.J., Fuel, 65, 480, (1986).
19. Kokorotsikos P.S., Stavropoulos G.G. and Sakellaropoulos G.P., Proc. Int. Conf. Coal Sci., 253, Sydney, Oct. 1985.
20. Stavropoulos G.G., Kokorotsikos P.S., Sakellaropoulos G.P., Carbon 86, 4th Int. Carbon Conf., 579, Baden-Baden, July 1986.

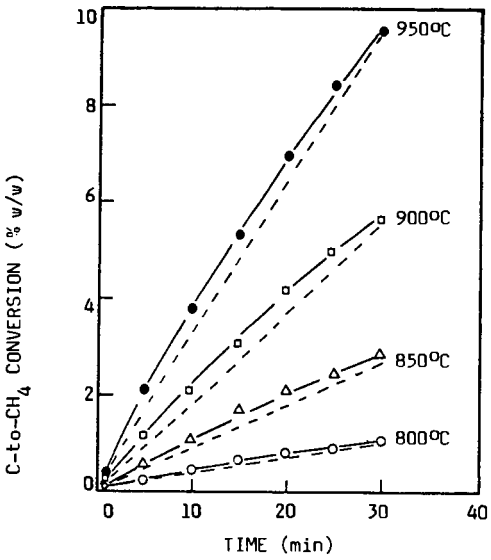

Figure 1. Comparison of model-predicted (dashed) and experimental values for the conversion of char carbon to methane. Points and solid lines are experimental data for hydrogasification.

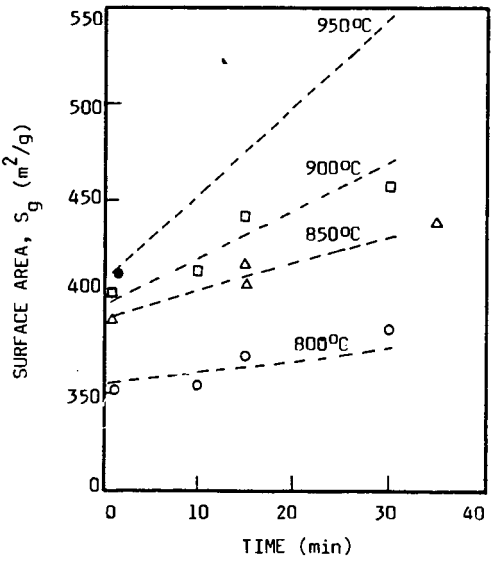

Figure 2. Calculated total surface area (dashed lines) and experimental data (points), compared at various conditions.

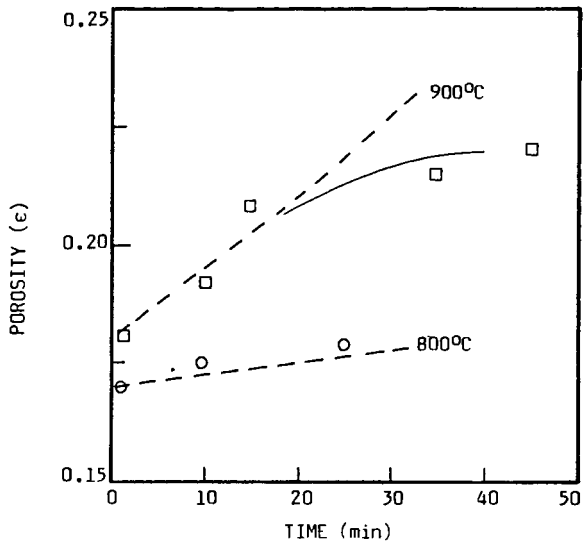

Figure 3. Porosity development of a lignite particle as measured experimentally (points) and predicted by the model (dashed lines).

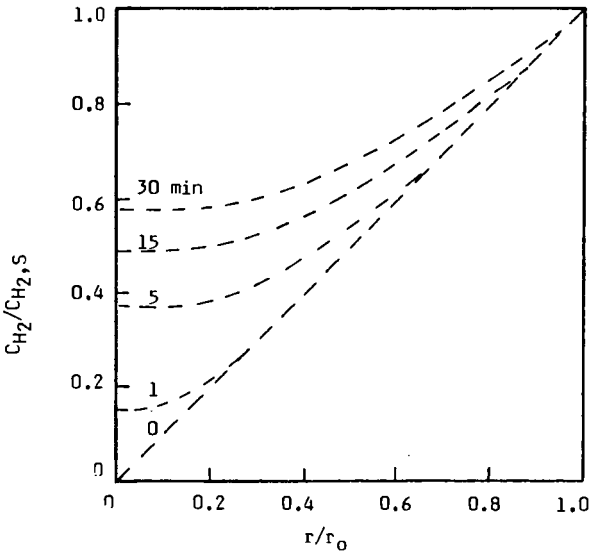

Figure 4. Hydrogen concentration profile with time in a gasifying lignite particle at 900°C (r_o=100μ).

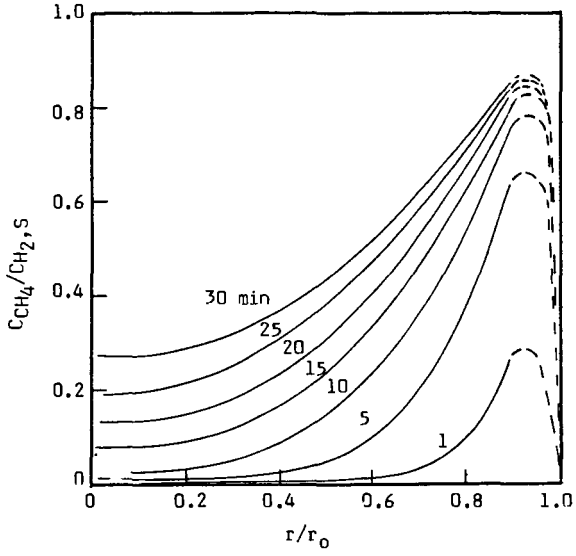

Figure 5. Methane concentration profile with time in a lignite particle at 900°C (r_o≈100μ).

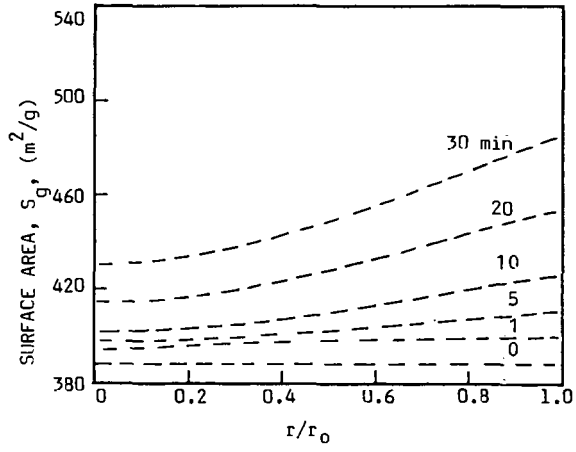

Figure 6. Surface area distribution with time, within a gasifying lignite particle at 900° C (r_o = 100 μ).

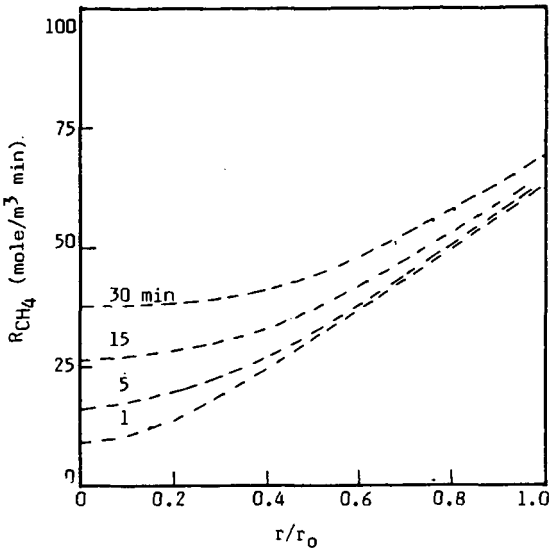

Figure 7. Radial distribution of methane formation with time in a lignite particle at 900°C (r_o = 100μ).

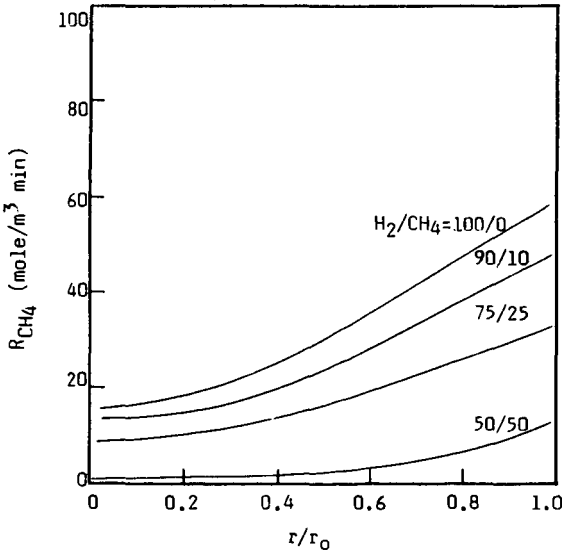

Figure 8. Effect of H_2 partial pressure on the radial distribution of methane formation, at 900°C and 5 min, (r_o = 100 μ).

DETERMINATION OF ATOMIC SODIUM IN COAL COMBUSTION USING LASER-INDUCED FLUORESCENCE

Philip G. Sweeny, Harmon B. Abrahamson, Lewis J. Radonovich, and Thomas A. Ballintine

Department of Chemistry, University of North Dakota, Box 7185 University Station, Grand Forks, North Dakota 58202

ABSTRACT

A laser-induced fluorescence spectrometer (LIFS) was assembled and sodium atom densities produced from the aspiration of solutions and direct introduction of a lignite into a flame were determined from fluorescence measurements. The average flame volume observed was 0.4 mm^3. This small volume allowed the measurement of sodium concentrations as a function of vertical and horizontal flame position. Temperature profiles of the flames employed were also obtained and compared with the sodium atom densities. The sodium atom densities calculated from the fluorescence measurements (N_{tf}) are compared with the sodium atom densities calculated from thermodynamic considerations (N_{tt}) and sodium concentrations derived from aspiration/introduction rates (N_{ta}).

INTRODUCTION

Many western low-rank coals contain significant quantities of alkali, primarily sodium, that is associated as salts of organic groups (1,2). Sodium content has been correlated with serious operational problems in combustion systems such as convective pass fouling (3,4). The flame-volatilized alkali can condense on surfaces of entrained fly ash particles forming low-melting-point layers which enhance adhesion of ash particles to heat transfer surfaces (5,6). Other studies relating flame composition and temperature to sodium volatilization have been published (7,8). These studies are all similar in that only the initial and final forms of sodium were analyzed. A few attempts have been made using mass spectrometry to directly measure amounts of alkali in coal-fed flames (8,9), with some difficulty. In order to accurately measure the density of volatilized sodium atoms in the flame region, an alternative approach is necessary.

Laser-induced fluorescence spectroscopy (LIFS) is well suited for probing various locations in flames to examine alkali release. This technique permits the quantitation of atomic species and has a small spatial resolution. The goal of this study was to determine if LIFS could be used to quantitate sodium atom densities in flames into which coal had been directly introduced, and to determine the effect of temperature and flame position on the sodium atom densities so measured.

EXPERIMENTAL

A laser-induced fluorescence spectrometer (LIFS) was used to measure the sodium atom densities produced from the aspiration of solutions and direct introduction of solids into a methane/argon/oxygen flame (2.9, 3.2, and 3.2 L/min, respectively). Argon (3.9 L/min) was used for the flame sheath. The excitation beam was generated by a flashlamp-pumped dye laser, focused and passed through a polarizing beam splitter. The horizontally polarized

beam was directed through the flame and the intensity of the vertically polarized rejected beam was monitored with a photomultplier tube (PMT). The bandwidth of the laser beam was 2-3 Å, the maximum energy available was 1 J, and the pulse length was 500-1000 ns. The diameter of the laser beam in the sample region was 2.0 mm.

The fluorescence detector was mounted perpendicular to the excitation beam in the horizontal plane, and two convex lenses were used to collect the Na fluorescence and focus it on the monochromator entrance slit. A polarizing filter set to pass only horizontally polarized light was placed directly in front of the monochromator. A PMT was positioned at the monochromator exit slit. The monochromator settings used for the Beulah lignite studies produced a bandpass of 1.2 nm and measured a sample volume of 0.4 mm^3. Various monochromator settings were used in the solution studies. Stanford Research Systems gated integrator/boxcar averagers were used to collect the signals from both PMTs. The first 300 ns of the fluorescence pulse was used to quantitate the sodium atom density. The boxcars were triggered by the laser flash via a photodiode.

The reported flame temperatures are those directly measured with a Pt/Pt-10%Rh thermocouple. The burner head was similar to that used by Daily and Chan (10). The radius of the burner head was 0.25 inch and the horizontal positions reported are those measured from the burner center with positive values indicating positions closest to the detector.

Solutions were aspirated into the flame via a Perkin Elmer nebulizer. The coal samples were introduced through a spouting bed coal feeder at a rate of 38.6 mg/min. The coal selected for the initial studies was a Beulah lignite. The proximate, ultimate, and ash analyses of this coal are shown in Table 1. A sized fraction between 200 and 325 mesh dried at 50 °C and 1 torr was used in this study.

The fluorescence intensity of the sodium solutions was defined as the difference between the intensity measured upon the aspiration of the analyte-containing solution less the intensity measured when plain deionized water was employed. The background signal for the coal studies was measured by tuning the laser and the monochromator to a wavelength 3 nm lower than the sodium doublet and introducing the coal sample. The fluorescence signal was taken as the difference between the intensity measured at the sodium doublet and the background measured at the lower wavelength.

The fluorescence data were obtained by taking ten points and averaging the results and calculating the standard deviation. The data among the original ten points not within a standard deviation were discarded leaving six to nine values to average for the reported data point.

The sodium atom densities were calculated in two different ways: from fluorescence intensities in the manner of Daily (11) to obtain N_{tf} values, and from a thermodynamic model described by Benson (12) to generate N_{tt} values. The total sodium concentrations in the flame were derived from sample aspiration/introduction rates following the procedure suggested by Wineforder and Vickers (13) to obtain N_{ta} values.

RESULTS

The LIFS was assembled and tested by aspirating sodium-containing solutions into the burner. The fluorescence signal was found to be linear over three orders of magnitude of Na concentration (N_{ta} = 7.6 x 10^7 atoms/mm^3 to N_{ta} = 7.6 x 10^{10} atoms/mm^3). The N_{tf} values for these solutions varied from 1.0 x 10^7 atoms/mm^3 to 1.0 x 10^{10} atoms/mm^3 respectively. The fluorescence measurements were taken at the flame edge closest to the detector. Five different sodium salts (NaCl, Na_2CO_3, $Na_2S_2O_3$, $NaCO_2C_6H_5$ and NaOH) were analyzed in the solution studies. The fluorescence intensity was independent of the sodium source.

In order to correlate the fluorescence measurements to actual sodium atom densities in the flame, it was necessary to establish saturation of the fluorescence signal (11). Plots of fluorescence intensity vs. laser power were obtained for both the solution studies and the Beulah lignite profiles. The laser intensity necessary to achieve saturation in the solution studies was 1.5 x 10^6 W/cm^2 nm and 1.2 x 10^7 W/cm^2 nm for the coal studies.

A horizontal fluorescence profile produced by the introduction of Beulah lignite into the methane/argon/oxygen flame was obtained (Figure 1). These results show that significantly higher fluorescence is observed upon viewing the side of the flame closest to the detector. The maximum fluorescence was observed at 0.28 inch from the flame center, producing the corresponding maximum in calculated sodium atom density.

A vertical fluorescence profile taken at the flame center is shown in Figure 2. The fluorescence signal was highest directly above the burner head, and decreased to a constant value at positions between 0.115 to 1.115 inches above the burner. A vertical temperature profile taken at a position of 0.175 inch is shown in Figure 3. The temperature was greatest at a distance of 0.056 inch above the burner. The temperature decreased from 1710 °C to 1600 °C upon travelling from 0.056 to 1.525 inches.

A vertical fluorescence profile was taken at the horizontal position of 0.35 inch (Figure 4). This graph shows that the fluorescence initially increases with vertical position and then levels off at an intensity corresponding to 1.6 x 10^9 atoms/mm^3. A vertical temperature profile was taken at the horizontal position of 0.35 inch (Figure 5). The temperature at this position increased rapidly with vertical position and leveled at a maximum near 1600 °C.

DISCUSSION

LIFS can measure changes in the density of sodium atoms generated by the introduction of solutions and solids into a flame. The linearity of the sodium concentration profile established this fact for solutions. The horizontal profile of Beulah lignite (Figure 1) establishes this fact for solids by showing increased fluorescence readings upon moving from outside to inside the flame zone.

The initial solution studies show that the LIFS can be used to quantitate sodium atom density in the flame, in addition to merely measuring differences in concentration. The

uniform increase in fluorescence signal with increased sample concentration demonstrates a range of concentration where quantitation is possible. The observation that the N_{tf} value is independent of the composition of the initial sodium salt indicates that equilibration of the sodium atoms with the other flame species is complete, and that this equilibrium is not significantly affected by the identity of the counter ion. It is significant that the N_{tf} values are only 14% of the N_{ta} values, while the thermodynamic calculations (N_{tf}) predict that 83 % of the sodium should be in the atomic form. The discrepancy between N_{ta} and N_{tf} values is of a magnitude similar to that reported by Smith et al. (14). These workers attributed this discrepancy to the estimates which contribute to N_{ta}, most significant in our case is the uncertainty in the degree of flame expansion. This explanation is realistic and therefore the difference between the percentages of sodium present in the atomic form calculated from the N_{tf}/N_{ta} ratio (14%) and that from thermodynamics (83%) is most likely due to the inaccuracy of N_{ta}.

The seemingly low N_{tf} values could also be due to decreased fluorescence intensity because of chemical reactions of the excited state sodium atoms (quenching). These types of reactions have been detailed by Muller et al. (15). In order to avoid this complication in our measurements only the initial 300 ns of the fluorescence was used for quantitation.

The calculation of the sodium atom densities depends on operation in the saturated state. Saturation was confirmed in both the solution and coal studies. The intensities needed for saturation are comparable to those reported by Smith et al. (14) for sodium solutions. Our observation that the saturation threshold is higher for solids than for solutions may be due to differences in the optical densities of the flames.

The horizontal profile of Beulah lignite (Figure 1) shows a maximum N_{tf} value at the flame edge closest to the detector. This asymmetry is a result of self absorption and/or the optical density of the coal entraining flame. A similar result was observed by Daily and Chan (10) when solutions of high sodium concentration were measured. This result points to the necessity of making measurements near the flame edge if accurate quantitation is desired.

The vertical fluorescence profile taken at the center of the flame (Figure 2) shows the fluorescence signal to be constant above 0.1 inch. Comparison of this result to the profile taken at the flame edge shows that the self absorption effect occurs up to flame positions of 1.115 inch. Comparison of Figure 2 with Figure 3 shows the fluorescence to be unaffected by small temperature changes. Comparison of Figure 4 to Figure 5 shows that the fluorescence apparently increases with flame temperature. The large variation in flame temperature at this latter horizontal position (0.35 inch) is because this is outside the burner radius and increasing vertical position moves the sample volume from outside to inside the expanded flame zone. Thus the fluorescence signal should increase as the observation point is moved into the active flame. (This latter fact leads to the conclusion that the data points taken at vertical positions of 0.015 inch are artifacts due to reflection of the laser off the burner head and do not represent actual sodium atom fluorescence.)

The vertical fluorescence profile taken at the flame edge (Figure 4) shows that N_{tf} reaches a maximum value of 2.1×10^9 atoms/mm^3; this corresponds to 1.8% of the N_{ta} value

(1.2×10^{11} atoms/mm^3). The thermodynamic calculations predict 83% of the sodium to be released at equilibrium. The N_{tf}/N_{ta} ratio for the coal (1.8%) is approximately 7.8 times smaller than that observed for solutions (14%). If we assume that equilibrium was reached in the solution studies, and that the N_{tf} values are correct, then the N_{ta} values are 5.9 times larger than the actual sodium densities. Incorporating this factor into N_{ta} for coal produces the conclusion that the maximum amount of sodium present as atomic vapor in the flame containing Beulah lignite is 11%.

SUMMARY AND CONCLUSIONS

LIFS can be used to measure differences in sodium atom concentrations in both solution- and solid-containing flames. Quantitation of the sodium atom density is possible at the flame edge. The sodium atom densities produced from the introduction of Beulah lignite are not affected by small changes in temperature. The maximum percentage of sodium present as atomic vapor in the Beulah lignite flame was 11% of the total sodium in the coal.

ACKNOWLEDGMENT

We are grateful for the support of the United States Department of Energy (through James Hickerson and Philip Goldberg at PETC), and the cooperation and assistance of the UND Energy Research Center.

REFERENCES

1. Benson, S. A.; Holm, P. L. *Ind. Eng. Chem. Prod. Res. Dev.* **1985**, *24*, 145.
2. Miller, R. N.; Given, P. H. U. S. Dept. of Eng. Report **1978**, FE-2494-TR1.
3. Raask, E. *Mineral Impurities in Coal Combustion* , Hemisphere Publishing Company: New York, 1985.
4. Sondreal, E. A.; Tufte, P. H.; Beckering, W. *Comb. Sci. .Tech.* **1977**, *16*, 95.
5. Wibberly, L J.; Wall, T. F. *Fuel* **1982**, *61*,87.
6. Boow, J. *Fuel* **1972**, *51*, 170.
7. Neville, M.; Sarofim, A. F. *Fuel* **1985**, *64*, 384.
8. Stewart, G. W.; Stinespring, C. D.; Davidovits, P. *Prepr., Div. Fuel Chem., Am. Chem. Soc.* **1982**, *27(1)*, 138.
9. Daily, J. W.; Chan, C. *Combustion and Flame* **1978**, *33*, 47.
10. Milne, T. A.; Beachey, J. E.; Greene, F. T. in *Ash Deposits and Corrosion Due to Impurities in Combustion Gases* , Bryers, R. W., Ed.; Hemisphere Publishing Corp.: Washington, 1978, p 217.
11. Daily, J. W. *Appl. Opt.* **1977**, *16*, 568.
12. Benson, S. A. Ph. D. Dissertation, Pennsylvania State University, 1987.
13. Winefordner, J. D.; Vickers, T. J. *Anal. Chem.* **1964**, *36*, 1939.
14. Smith, B.; Winefordner, J. D.; Omnetto, N. J. *Appl. Phys.* **1977**, *48*, 2676.
15. Muller, C. H.; Schofield, K.; Steinberg, M. J. *Chem. Phys.* **1980**, *72*, 6620.

TABLE I.
Analysis of Beulah High-Sodium Lignite.

Ultimate Analysis (wt% moisture-free)	
C	62.8
H	3.9
N	1.5
S	1.7
O	16.8
ash	13.3

Proximate Analysis (wt% as received)	
H_2O	34.9
ash	8.7

Ash Analysis (wt% ASTM)	
SiO_2	20.4
Al_2O_3	12.6
Fe_2O_3	10.8
TiO_2	1.2
P_2O_5	0.9
CaO	18.9
MgO	5.9
Na_2O	6.3
K_2O	0.0
SO_3	22.8

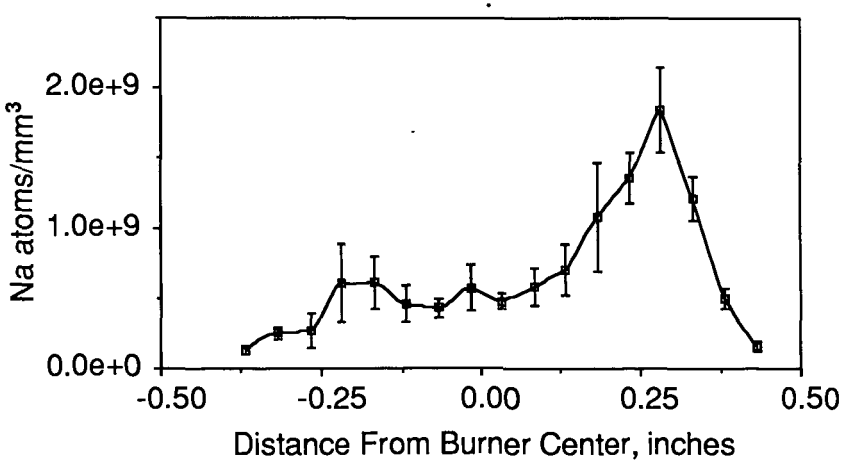

Figure 1. Horizontal fluorescence profile of Beulah lignite at a vertical position of 0.415 inch.

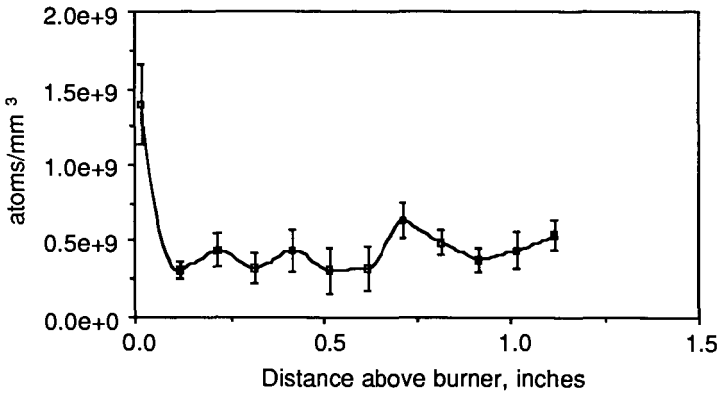

Figure 2. Vertical fluorescence profile of Beulah lignite at the flame center.

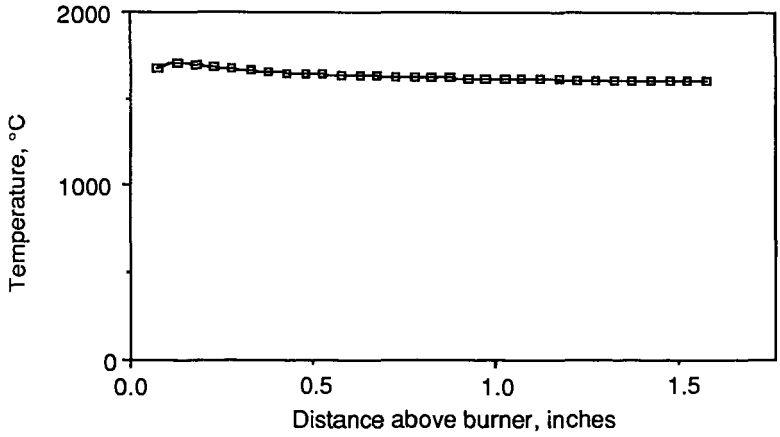

Figure 3. Vertical temperature profile of Beulah lignite at a horizontal position of 0.175 inch.

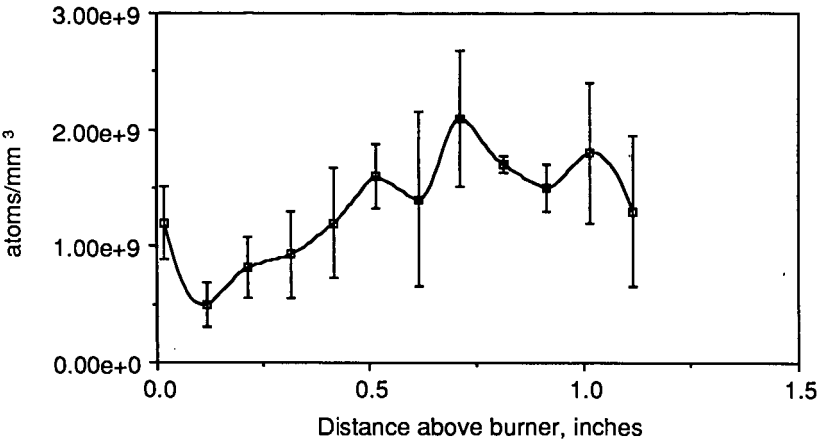

Figure 4. Vertical fluorescence profile of Beulah lignite at a horizontal position of 0.35 inch..

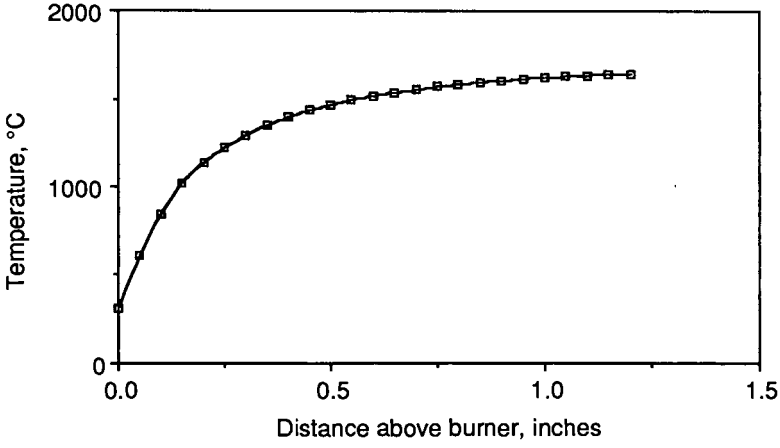

Figure 5. Vertical temperature profile of Beulah lignite at a horizontal position of 0.35 inch.

The Effects of Ion-exchanged Cobalt Catalysts on the Gasification of Wood Chars in Carbon Dioxide

William F. DeGroot and G.N. Richards

Wood Chemistry Laboratory, University of Montana, Missoula, Montana 59812 USA

Wood is composed primarily of cellulose, hemicelluloses, and lignin, with lesser quantities of extractives (material extractible in organic solvents) and mineral matter. The cottonwood species used in this study has been analyzed previously in this laboratory and it was found to contain 44% cellulose and 32% hemicelluloses on an extractive-free basis (1). The major component of the hemicelluloses is O-acetyl-4-O-methylglucuronoxylan, a polymer comprised of repeating units of xylose with acetyl and 4-O-methylglucuronic acid substituents substituted along the polymer chain. Figure 1 shows a representative chemical structure of this polymer, but does not correctly represent the frequency of substituents; approximately half of the xylose residues contain an acetyl group and there is one 4-O-methylglucuronic acid group per 10-20 xylose residues (1,2). These acid groups provide a means of incorporating catalysts into wood in a reproducible, highly-dispersed manner by ion exchange. Similar methods are used in catalysis of low-rank coals, but the ion exchange capacity of wood is much lower than that of coals. Our wood sample was found to contain 8-10 meq of carboxylic acid groups per 100 grams of wood (2), while low-rank coals typically contain 10-50 times higher concentrations of carboxylic acid groups (3,4).

The effects of several ion-exchanged catalysts on gasification of wood chars in carbon dioxide were described in an earlier paper (5). Ion-exchanged cobalt and calcium were found to be very effective catalysts of gasification of wood chars (HTT 800°C). In this paper we focus on the activity of cobalt catalysts for gasification of wood chars prepared at different heat treatment temperatures.

The gases formed by pyrolysis of low-temperature chars have also been determined by temperature-programmed desorption (TPD) using mass spectrometry. This analysis is indicative of structural features of the char and helps to elucidate the chemical transformations occurring in low-temperature chars (HTT 400°C) as they are heated to high temperatures.

EXPERIMENTAL

The wood sample used in this study was sapwood from black cottonwood (Populus trichocarpa). The wood was ground in a Wiley mill, sieved, and the 20/30 mesh fraction was retained for analysis. Chars were prepared in a tube furnace purged with flowing nitrogen, as described previously (1), and they were stored in nitrogen- or argon-purged containers between analyses.

Acid washing and cobalt ion exchange treatments were carried out by column percolation. For cobalt ion exchange the ground, acid-washed wood (2.5 g) was degassed in a small quantity of 0.01 M cobalt acetate solution and transferred to a glass chromatography column. The wood was then washed slowly with 500 ml of the 0.01 M cobalt acetate solution, followed by a thorough wash with distilled, deionized water to remove any unbound salt. Acid washing was carried out by essentially the same procedure except that 0.01 M HCl was used.

Reactivity measurements were carried out in a gasification reactor/detector system described previously (1). Briefly, the system consists of a small-scale temperature-programmed alumina reactor coupled to a combustible gas detector. The reactor can be maintained under either an inert or a reactive atmosphere. For inert conditions it is swept with nitrogen or helium (40 cc/min) and an equivalent flow of carbon dioxide is valved into the reactor for gasification.

The detector consists of a ZrO_2 solid electrolyte oxygen sensor which is maintained at a temperature of 650-700°C. Combustible gases formed in the reactor combine with an air stream after they leave the reactor and they undergo combustion in the hot detector. The detector monitors the depletion of oxygen content in the combined gas streams. The rate of carbon gasification is calculated from the combined gas flow rates and the oxygen depletion, assuming that one mole of carbon is gasified for each mole of oxygen consumed.

The rate of gasification of a char (HTT 800°C) prepared from untreated cottonwood is shown in Figure 2. The detector output can be integrated over the entire run to give the total extent of gasification, or it can be integrated above the baseline defined by the rate of pyrolytic gasification (dotted line) to give the extent of gasification due to reaction with CO_2. The extents of gasification reported in this paper are those due to gasification alone, i.e. excluding pyrolysis. Extents of conversion determined in this way compare well with measured weight losses, generally amounting to 100-110% of the weight loss. This system is preferred to gravimetric systems for our purposes because of its greater sensitivity and better control of temperature and gas flows.

The gasification system was modified to include a unit resolution mass spectrometer (Hewlett-Packard Model 5970B) for qualitative analysis of gas mixtures formed during pyrolysis of the sample prior to gasification. When the mass spectrometer was in use helium was used as the reactor purge gas. A splitter was placed in the gas line between the reactor outlet and the combustion air inlet. One meter of uncoated vitreous silica capillary tubing (0.20 mm ID) connected the splitter to the mass spectrometer. The capillary tubing was contained in a transfer line heated to 100°C. This arrangement diverted approximately 0.1 ml/min (0.3%) of the reactor gas flow to the mass spectrometer. On the basis of preliminary runs which revealed no high molecular weight pyrolysis products, the mass range of 10 to 110 amu was scanned and approximately fifteen mass spectra were accumulated per minute.

X-ray diffraction patterns were obtained using a Phillips diffractometer (CuKα, 35kV, 20mA) at a scan rate of 1 degree per minute. The sample was mounted on a glass slide using a vaseline smear.

RESULTS

Gasification Rate Determination

Table 1 shows the yields and reactivities of chars prepared at different HTT's from wood treated by ion exchange with cobalt, calcium, and potassium. The char prepared from one of the cobalt-exchanged samples was initially so reactive that the rate of gasification exceeded the detection limits of the detector, i.e., all of the oxygen in the combustion air supply was consumed by combustion of product gases. In this case the maximum rate of gasification was not observable, and the extent of gasification was therefore indicated as being "greater than" the value of the integrated detector response. The change in sample weight is indicated to show the total extent of reaction.

The reactivities of the chars containing cobalt catalyst are clearly less dependent on HTT than are those of the chars containing calcium and potassium. The reactivities of the latter chars toward gasification at 800°C increase by at least a factor of two as the HTT is reduced from 1000° to 800°C. This behavior is typical of trends shown by other investigators who have studied the effects of HTT on catalyzed gasification of lignite chars (6-8). By contrast, chars prepared from cobalt-exchanged wood at 800° and 1000°C are gasified to a similar extent at 800°C. When HTT and gasification temperature are reduced to 600°C, the char prepared from cobalt-treated wood is completely gasified, whereas the chars prepared from calcuim and potassium-exchange wood are completely unreactive at this temperature. When

cobalt-exchanged wood was charred and gasified at 400°C, no gasification occurred.

Table 1. Effect of HTT on extent of CO_2 gasification of chars from ion-exchanged wood. Gasification was for 30 min in 90.9 kPa of CO_2.

Treatement	HTT (°C)	Char Yield[b] (%, d.a.f.)	Gasification Temperature (°C)	Percent Gasified
Co-exchanged	1000	7.4	800	>69[a]
	800	9.2	800	73
			600	46
	600	12.9	600	96
	400	21.3	400	0
K-exchanged	1000	9.9	800	6%
	800	13.4	800	13
	600	17.5	600	0
Ca-exchanged	1000	8.1	800	36
	800	9.3	800	102[c]
	600	12.7	600	0

[a]Measured weight loss was 73%.

[b]Char yields are reported on a dry, ash-free basis assuming that the weight of the ash in the original wood remains in the char.

[c]Sample gasified completely. Percent of conversion determined by integration of combustible gas detector signal was consistently 100-110% of measured weight loss.

In order to better assess the dependence of reactivity on HTT in more detail, chars prepared from cobalt-exchanged wood at 100°C increments of HTT were gasified at 500°C. The results are shown in Table 2. The maximum reactivity is attained at the HTT 600°C. The reactivity decreases slightly when the HTT is raised to 700°C and more dramatically when the HTT is raised to 800°C. There is very little reaction for the sample of HTT 500°C. These results suggest that there is a threshold temperature for activation of the catalyst at about 600°C.

Table 2. Effect of heat treatment temperature (HTT) on the yield and reactivity of chars prepared from cobalt-exchanged wood. Gasification was carried out for 30 min at 500°C in 90.9 kPa of CO_2.

Sample	HTT	Char Yield (%, d.a.f.)	Percent Gasified
Co-exchanged wood	800	9.2	16
(0.23% Co, 0.34% ash)	700	10.9	66
	600	12.9	70
	500	17.2	3

To obtain a more detailed description of the nature of catalysis by cobalt it is helpful to consider the changes in reaction rate with extent of gasification or "gasification rate profiles", as shown in Figure 3. The gasification rate profile for the HTT 800°C char prepared from cobalt-exchanged wood undergoes two phases of reaction when gasified at 800°C. The first stage is very rapid but decreases as the

reaction proceeds. The second phase is characterized by a lower, more constant rate of reaction.

Figure 4 shows the gasification rate profile of a low-temperature char (HTT 600°C) gasified at 600°C. This char was much more reactive than the char prepared at 800°C and the maximum rate exceeded the detector capacity. As shown by the extents of gasification in Table 1, the low-temperature char was completely gasified in this case, and there was no evidence of the second, slower phase of gasification which was observed in gasification of higher temperature chars (HTT 800°C) at 800°C.

Pyrolytic Gasification of Low-Temperature Chars

We investigated the pyrolytic transformations that occur in chars (HTT 400°C) prepared from untreated and cobalt-exchanged cottonwood upon heating to 800°C in order to determine the existence and nature of any significant catalyst/substrate interactions which occur during pyrolysis. Figure 5 shows the gasification rate profile and the total ion profile for a char (HTT 400°C) prepared from untreated cottonwood heated in flowing helium to 800°C; both curves are from the same experiment. The shape of the gasification rate profile is distinctly different from that of the total ion profile. The former peaks at 10.5 min, corresponding to the end of the temperature ramp, while the total ion profile peaks at 8.5 minutes (600°C). The difference in the two profiles is apparently due to evolution of molecular hydrogen in the higher temperature range. Hydrogen is not detected by the mass spectrometer, but the combustible gas detector is very sensitive to the evolution of hydrogen, since its combustion requires three times more oxygen per unit weight than does combustion of carbon. Comparison of these curves therefore suggests that evolution of molecular hydrogen from the char predominates at high temperatures (T>650°C), while carbonaceous compounds are evolved at lower temperatures.

Analysis of individual mass spectra acquired during these experiments indicates that the most prominent species evolved are CO (m/z 28) and CO_2 (m/z 44), with CO_2 evolution decreasing at higher temperatures. There is also a smaller, but significant quantity of water (m/z 18) evolved throughout the pyrolysis process. Mass peaks indicative of methanol, low molecular weight aldehydes and hydrocarbons are also present in very low abundances.

The gasification rate profile shown in Figure 5 has been demonstrated to be representative of untreated wood as well as wood treated with alkali and alkaline earth metals (9). However, as shown in Figure 6, the gasification rate profile of low-temperature chars containing the cobalt catalyst differs from this pattern. The profile for the char (HTT 400°C) prepared from cobalt-exchanged wood peaks much earlier than that of the char from untreated wood, and this appears to be due to a peak (5.8 min, 630°C) superimposed on the profile of the untreated wood. The same peak is evident on the total ion profile, which suggests that this additional transition involves evolution of carbonaceous species. However, analysis of the mass spectra corresponding to this peak does not indicate that this peak in the gasification rate profile corresponds to the enhanced evolution of any single product. The data do not, therefore suggest a specific solid phase reaction involving interaction of the cobalt catalyst with carbon. However, we believe that this transition, which is unique among the catalysts studied and corresponds to the HTT at which the catalyst became active (see Tables 1 and 2), corresponds to the reduction of the catalyst to the elemental state which has been shown to be the active state of transition metal catalysts for gasification of graphite (10), wood chars (11), and coal chars (12).

X-Ray Diffraction

X-ray diffraction (XRD) patterns for chars prepared at 800° and 1000°C from cobalt-exchanged wood are shown in Figure 7. The diffraction patterns show evidence

of different crystalline phases in the two chars. Two of the peaks in the diffraction pattern of the higher temperature char, correspond to d-spacings characteristic of elemental cobalt (2θ=44.2° and 51.5°) (13). The large, broad peak in the XRD pattern for this char is not identified and probably corresponds to ordered regions in the carbon lattice. The peaks in the diffraction pattern of the char of HTT 800°C could not be correlated with a crystalline cobalt compound or with compounds of the small quantity of calcium remaining in this sample. No XRD peaks were observed in chars (HTT 800°C) from potassium- or calcium-exchanged samples.

DISCUSSION

The results obtained in this study demonstrate the exceptionally high activity of cobalt in catalyzing the gasification of wood chars in carbon dioxide. A pyrolysis temperature of about 600°C appears to be required to activate the catalyst. At higher heat treatment temperatures the maximum catalytic activity declines.

Figueiredo et al. studied the gasification of chars (HTT 850°C) prepared from pine wood doped with higher levels of cobalt nitrate (1.6% metal) (14). These authors report gasification behavior in pure CO_2 similar to that reported here, i.e., an initial period of rapid gasification lasting a few minutes followed by slow gasification of the remaining char. They measured gasification rates in the temperature range of 740-910°C and report an initial (presumably maximum) rate at 805°C of 0.18 min^{-1} which is very comparable to the initial rate of 18 mMoles $C \cdot min^{-1} \cdot g^{-1}$ (0.22 $g \cdot g^{-1} \cdot min^{-1}$) found in this study for a char (HTT 800°C) gasified at 800°C (see Figure 3). Their data extrapolate to much lower rates at 600° and 500°C than those found in this study for gasification of a char prepared at 600°C (see Figure 4). The effect of the higher concentration of cobalt in their wood is presumably offset by lower dispersion of the catalyst due to the mode of addition, higher HTT, and larger heat treatment time used in preparation of chars (1 hr vs 10 min in this study). These authors suggest that the decline in activity is due to oxidation of the active reduced form to CoO during gasification, and they cite XRD evidence for CoO in chars after gasification. However, the results of this study show that the rapid, catalyzed stage of gasification can be maintained throughout the reaction to give complete gasification of chars prepared and gasified at lower temperatures (600°C, see Figure 4). We therefore believe that the slower stage of gasification is due to gasification of carbon which is no longer in contact with the catalyst due to its agglomeration at high temperatures.

The combined data from this study suggest a picture of catalysis by cobalt involving (1) reduction to an active catalytic state, probably elemental cobalt, near 600°C followed by (2) agglomeration of the catalyst particles to form crystalline cobalt. The latter process, which is much more important at temperatures greater than 800°C, gives rise to two distinct phases of gasification. The first, corresponding to gasification of carbon in contact with cobalt crystallites is fast, while the second, slower rate corresponds to gasification of char which is not in contact with catalyst (see Figure 1). On the basis of the XRD evidence for crystalline elemental cobalt in chars of HTT 1000°C, we believe that elemental cobalt is the active phase of the catalyst throughout the reaction, but it is detectable by XRD only when crystallite growth is at an advanced stage.

The presence of reduced cobalt in wood chars also suggests that the relative activities of transition metal catalysts in gasification by carbon dioxide might be associated with the rate of dissociation of the reactant gas on the metal surface. Grabke has reported rate constants for dissociation of CO_2 on cobalt, nickel and copper at 1000°C (15), which are pertinent to the non-equilibrium conditions used in our studies. The rate constants decrease in the order: $k_{Co} > k_{Ni} >> k_{Cu}$, which is the same order of relative activities reported for transition metal catalysts in the earlier paper (5). The results of these studies are therefore consistent with an oxygen transfer mechanism, as described by Walker et al. in the iron-catalyzed

gasification of graphite by CO_2 (10) or possibly an oxygen 'spillover' mechanism (16), depending on whether the adsorbed atomic oxygen reacts with the metal to form the metal oxide before reacting with carbon in contact with the catalyst particle.

ACKNOWLEDGEMENT

This work was supported by the Gas Research Institute under Grant No. 5082-260-0683. We are grateful to Dr. John Wehrenberg of the University of Montana Department of Geology for providing the XRD data and to Dr. R.K. Osterheld of the University of Montana Department of Chemistry for helpful discussions.

REFERENCES

1. Shafizadeh, F. and McGinnis, G.D., Carbohydr. Res., 16, 273 (1971).

2. DeGroot, W.F., Carbohydr. Res., 142, 172 (1985).

3. Kube, W.R., Schobert, H.H., Benson, S.A., and Karner, F.R., in The Chemistry of Low-Rank Coals, H.H. Schobert, ed., American Chemical Society, Washington, D.C., 1984, pp. 39-52.

4. Shafer, H.N.S., Fuel, 49, 197 (1970).

5. DeGroot, W.F. and Richards, G.N., Prepr. Pap., 191st ACS National Meeting, Division of Fuel Chemistry, 31(2), 28 (1986).

6. Radovic, L.R., Walker, P.L., Jr., and Jenkins, R.G., Fuel, 62, 209 (1983).

7. Jenkins, R.G., Nandi, S.P., and Walker, P.L., Jr., Fuel, 52, 288 (1973).

8. Hippo, E.J., Jenkins, R.G., and Walker, P.L., Jr., Fuel, 58, 388 (1979).

9. DeGroot, W.F. and Richards, G.N., "Chemistry of Carbon Gasification Reactions," Final Report, Gas Research Institute, Chicago, 1986.

10. Walker, P.L., Jr., Shelef, M., and Anderson, R.A., "Chemistry and Physics of Carbon," P.L. Walker, Jr., ed., Marcel Dekker, New York, 1968, Vol 4, p. 287.

11. DeGroot, W.F. and Shafizadeh, F., Fuel, 63, 210 (1984).

12. Kasaoka, S., Sakata, Y., Yamashita, H., and Nishino, T., Int. Chem. Eng., 21, 419 (1981).

13. ASTM Publication No. PDIS-17i, "Index (Inorganic) to the Powder Diffraction File," Amer. Soc. for Testing and Materials, Philadelphia, 1967.

14. Figueiredo, J.L., Orfao, J.J.M., and Ferraz, M.C.A., Fuel, 63, 1059 (1984).

15. Grabke, H.J., Ber. Bunsenges Phys. Chem., 71, 1067 (1967).

16. Baker, R.T.K. and Chludzinski, J.J., Carbon, 19, 75 (1981).

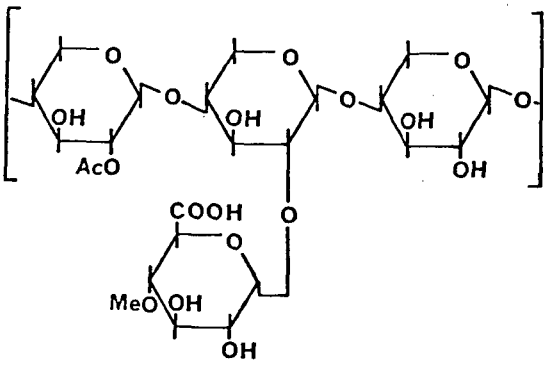

Figure 1. Representative structural elements of acetyl 4-O-methylglucuronoxylan.

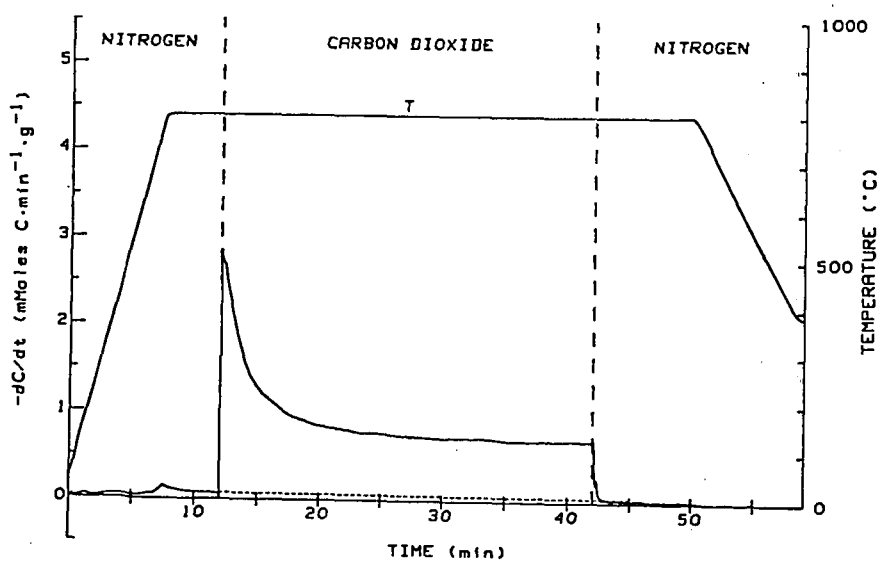

Figure 2. Gasification rate profile for gasification at 800°C of char (HTT 800°C) prepared from untreated cottonwood.

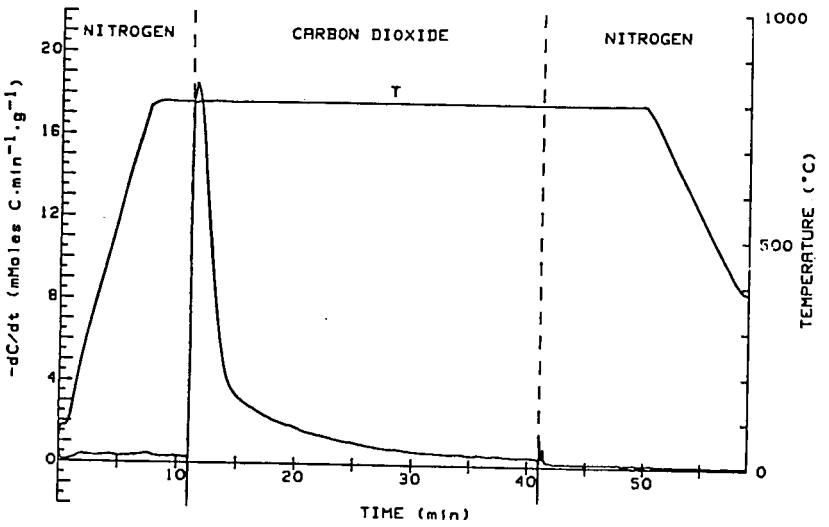

Figure 3. Gasification rate profile for gasification at 800°C of char (HTT 800°C) prepared from cobalt-exchanged cottonwood.

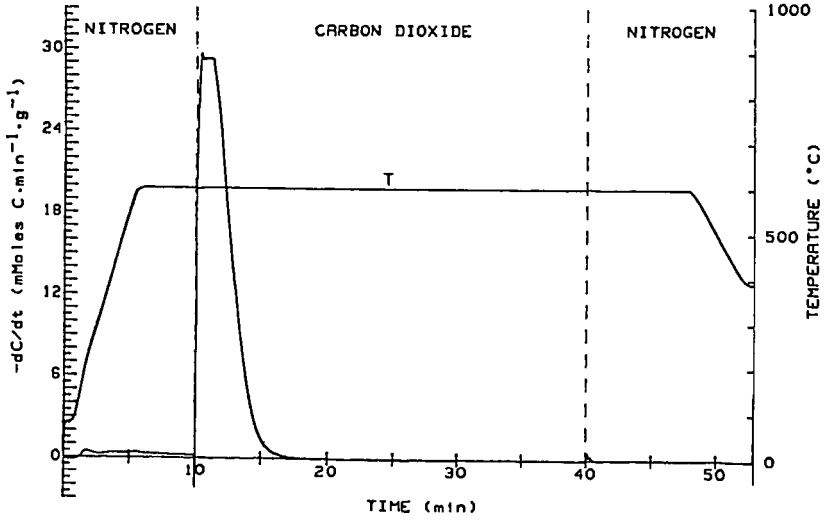

Figure 4. Gasification rate profile for gasification at 600°C of char (HTT 600°C) prepared from cobalt-exchanged cottonwood.

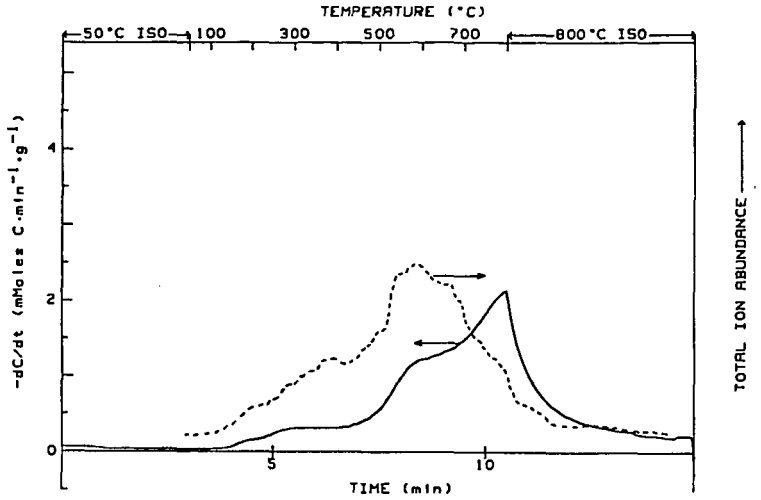

Figure 5. Gasification rate profile and total ion profile for pyrolytic gasification in helium of char (HTT 400°C) prepared from untreated cottonwood.

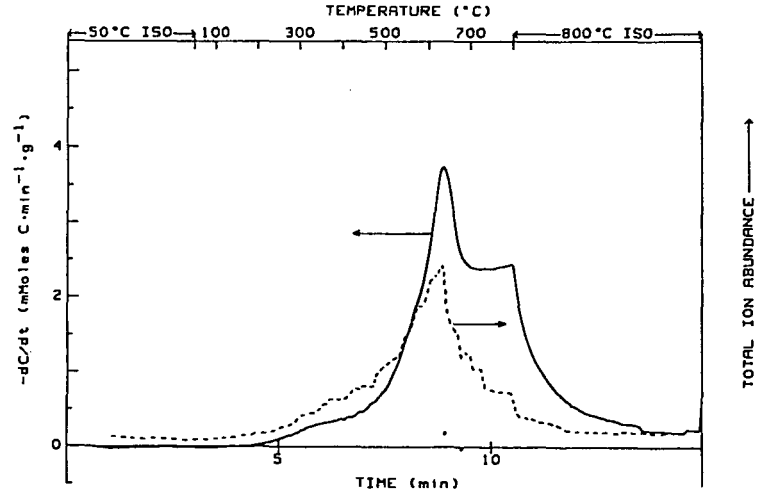

Figure 6. Gasification rate profile and total ion profile for pyrolytic gasification in helium of char (HTT 400°C) prepared from cobalt-exchanged cottonwood.

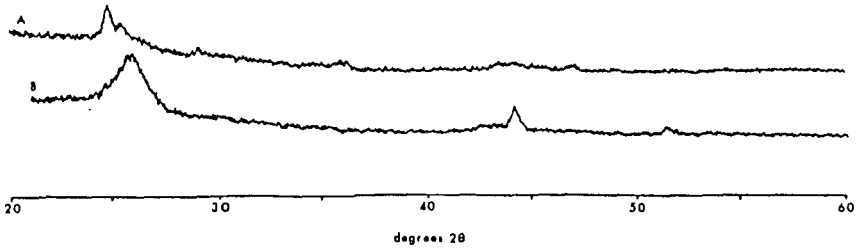

Figure 7. XRD patterns obtained from chars prepared from cobalt-exchanged cottonwood at HTT's of (A) 800°C and (B) 1000°C.

Determination of the Distribution of Ash, Pyrite and Basic Constituents in Coal Particles

D. M. Mason and S. S. Chao

Institute of Gas Technology
3424 South State Street
Chicago, Illinois 60616

INTRODUCTION

In fluidized-bed gasification of high-sulfur coals, such as the KRW and U-GAS processes, relatively low melting ash is produced by reaction of iron from pyrite with the siliceous components produced from clays and quartz.(1,2) To prevent catastrophic growth of ash clinkers and defluidization of the bed, ash in the bed must be limited to 40 to 50 weight percent. As a result of this low ash content of the bed, the ash must be agglomerated to facilitate its removal from the bed without unacceptable loss of char carbon and decrease of gasification efficiency. To obtain a detailed understanding of the behavior of mineral matter and ash in fluidized-bed gasification, a fundamental research investigation is in progress at IGT under a program supported by the U.S. Department of Energy.(2,3)

In our approach to the problem, we note that pyrite quickly decomposes to ferrous sulfide when the coal is introduced into the hot fluidized bed of a gasifier; also that sufficient hydrogen sulfide is produced from high sulfur coal to stabilize the ferrous sulfide in the back-mixed fluidized bed away from the oxygen inlet region; also that in the back-mixed bed the gasification reactions with steam and carbon dioxide occur relatively slowly and thus tend to occur throughout char particles. Complete removal of the carbon in char particles must occur before the oxidized iron can contact the siliceous components in the ash. Both this carbon removal and the oxidation of the ferrous sulfide occur only in the oxygen inlet region. Elevated temperatures in this region also facilitates the reaction of oxidized iron with the siliceous components to form relatively low-melting iron aluminosilicates. In both the KRW and U-GAS processes, oxygen is introduced through a central jet, forming an oxygen reaction region resembling a burner flame. Thickness, shape, and temperature of this reaction region is known only within wide limits.

We envision that the initial formation of ash reaction products occurs by reaction of the minerals present in single particles of char formed from single particles of coal. The oxide composition of the ash of single particles determines their melting point, viscosity and potential for agglomeration. In this paper we report the results of the application of some methods of investigation of ash composition in single particles of coal.

Selection of Coals

As part of the research on the behavior of ash in fluidized-bed gasification, several coals were selected for test in a 2-inch reactor. These were five eastern U.S., one western (New Mexico) bituminous, and one subbituminous coal. All had been washed except the subbituminous coal. Four of the eastern U.S. coals were selected to cover a range of iron oxide content of the ash from about 10 to 30 weight percent Fe_2O_3 along with a calcium oxide content of 2.5 weight percent or less; the other, an Illinois No. 6 seam coal, was selected to show the effect of high calcium oxide content with low iron oxide. Analytical data pertaining to minerals and ash of the coals, including iron distribution by Mossbauer spectroscopy and mineralogy by computer-assisted scanning electron microscopy (SEM), are presented in Table 1.

Table 1. ANALYSES OF MINERALS AND ASH OF COALS USED IN GASIFICATION TESTS

Seam Mine	KY No. 9 Providence	OH Pitt No. 8 Franklin 125	KY No. 13 Ken No. 13	IL No. 6 Burn. Star 4	IN VI Universal	York York Canyon	Rosebud Rosebud
Ash Composition, wt %							
SiO_2	54.5	41.6	58.5	54.1	51.1	44.4	48.8
Al_2O_3	17.8	20.9	26.9	16.9	21.9	24.3	23.5
Fe_2O_3	19.9	31.7	8.1	10.7	15.7	9.0	7.02
TiO_2	0.80	1.02	0.87	0.70	0.85	1.02	0.12
P_2O_5	0.07	0.07	0.16	0.13	0.12	2.11	0.25
CaO	2.29	1.14	0.90	8.34	2.48	8.15	7.16
MgO	0.67	0.36	1.21	0.95	1.18	2.15	2.57
Na_2O	0.54	0.35	0.24	0.75	0.65	0.90	0.09
K_2O	2.20	0.98	2.94	1.96	2.85	0.44	0.36
SO_3	2.10	1.00	0.80	7.00	1.30	5.50	9.91
Total	100.9	99.2	100.6	101.5	98.1	98.0	99.78
Ash Content (as ashed for analysis of ash, dry basis)	7.9	7.7	8.2	13.4	13.5	8.0	
Iron Distribution (by Mossbauer Spectrocopy)*							
Pyrite	92.1	95.8	71.4	91.6	80.5	9.7	--
Clay	--	--	11.2	--	6.9	70.6	--
Siderite	--	--	--	--	--	15.5	--
Ferrous Sulfate[a]	7.9	4.2	--	4.6	tr?	--	--
Ferric Sulfate[b]	--	--	17.4	3.8	12.7	4.2	--
Mineral Distribution (by SEM)*							
	wt % of total minerals						
Quartz	20	11	17	20	23	6	--
Kaolinite	5	10	7	3	3	14	--
Illite	7	11	20	7	18	2	--
Chamosite[c]	--	--	1	<1	<1	8	--
Montmorillonite	<1	1	1	2	1	5	--
Mixed Silicates[d]	22	20	28	23	25	31	--
Pyrite	33	36	17	23	18	1	--
Iron Sulfates	3	2	2	<1	1	--	--
Siderite	<1	<1	<1	--	<1	2	--
Calcite	5	--	<1	16	4	10	--
Ankerite	--	--	--	--	--	1	--
Rutile	<1	1	<1	<1	<1	--	--
Apatite	--	--	--	--	--	2	--
Misc. Mixed	>4	>8	>6	>5	>5	18[e]	--

*By G. F. Hoffman and Associates at Macro-Arom, Inc.

[a] $FeSO_4 \cdot H_2O$ and $FeSO_4 \cdot 7H_2O$.

[b] $KFe_3(SO_4)_2(OH)_6$.

[c] Hydrated magnesium-iron aluminosilicate.

[d] Mostly mixed layer clays.

[e] Includes many Ca(Sr)-Al(Si)-P particles, possibly crandallite.

Distribution of Ash Composition Among Particles

Moza and Austin have described the analysis of individual pulverized coal particles by computer-assisted SEM.(4) The objective of this work was the evaluation of coals for slag deposition in electric utility boilers fired with pulverized coal. Sieve fractions of particles from 10 to 106 μm in diameter were mounted separately, sectioned and polished; those particle cross-sections falling within the size range of the sieve fraction were selected for x-ray emission analysis; about 280 particles of the coarsest fraction and 800 to 900 of the finest were analyzed.

Moza and Austin's method seems admirable for pulverized fuel, but of doubtful applicability to the 1/4-inch top size feed to fluidized-bed gasifiers. One difficulty is that sections oriented parallel to the coal bedding are not representative of the minerals of the whole particle.

For this investigation, we adopted a chemical method in which the ash compositions of 32 single particles were determined. Particles from the -10+12 mesh fraction of the 1/4 inch top size coal were taken for analysis; this size furnishes enough ash for the chemical analysis and is about the average size, by weight, of the coal feed to a pilot plant or commercial fluidized-bed gasifier. Particle weight, ash content, and iron oxide and calcium oxide in the ash were determined. In addition to determined contents of iron and calcium oxide in the ash, the content of basic constituents was estimated by adding the average amount of other basic oxides (MgO, K_2O and Na_2O), as determined by a conventional major and minor oxides analysis, to the determined iron and calcium oxides. A correction for sulfur trioxide in the particle ash was made, based on the average ratio of SO_3 to CaO in the conventional analysis of the ash of the eastern U.S. coals that we investigated. This method of correction was not satisfactory when the content of calcium oxide in the single particle ash was higher than about 20%.

Analysis of the single particles are reported in detail elsewhere.(3) Averages for the first 16, the second 16, the odd-numbered particles, the even-numbered particles, and for all particles are also listed; the subsets were calculated to obtain a measure of the effect of number of analyzed particles. For eastern bituminous coals, the most important distribution is that of the iron oxide content of the ash. For the Kentucky No. 9 coal, the average iron oxide contents of the four groups of 16 particles ranges from 21.72 to 26.35 weight percent, and the average for all particles is 22.27 weight percent compared to 19.9 weight percent obtained by the conventional analysis for major and minor oxides. We conclude from this and similar data on the other coals that analysis of 32 particles is necessary and may be sufficient for characterizing the distribution.

A comparison of the averages of the particles with the values of the conventional major and minor oxides is presented in Table 2. While the average iron oxide in the ash of the 32 particles of Kentucky No. 9 coal agrees well with the conventional analysis, less than half as much calcium oxide was present in the -10+12 mesh particles as in the conventional analysis. We think that the missing calcium oxide occurs as calcite in the cleat of the coal, along which fracture occurs in crushing and sieving, resulting in its concentration in the finer sieve fractions. Presence of plates of calcite, about 10 μm thick, in the cleat fractures of the Kentucky No. 9 coal is shown in a photomicrograph (Figure 1) of a polished section of coal etched by low temperature oxidation to expose the minerals. In the photomicrograph, only the crack normal to the bedding is a cleat fracture; the curved cracks are artifacts produced in the preparation and etching.

Similar loss of calcium oxide from the -10+12 mesh particles is also evident with the Indiana VI coal (Table 2), while 90% of the average 8.34 weight percent of calcium oxide in the ash of the Illinois No. 6 coal has been lost. No loss, or

Table 2. SUMMARY OF SINGLE PARTICLE ANALYSES

	Ash Content (moist basis)		Fe_2O_3 in Ash		CaO in Ash	
	Avg. of Particles	Conventional	Avg. of Particles	Conventional	Avg. of Particles	Conventional
	wt %					
KY No. 9	6.3	7.6	22.3	19.9	1.10	2.29
Pittsburgh	10.9	7.5	34.2	31.7	1.14	0.90
KY No. 13	8.2	7.3	8.6	8.1	0.69	0.90
IL No. 6	10.3	11.9	12.1	10.7	0.83	8.34
IN VI	16.4	13.4	6.9	15.7	0.36	2.48
Rosebud	10.3	11.3	0.55	7.0	9.4	7.2

only a marginal one, is evident from the Pittsburgh No. 8 or Kentucky No. 13 coals. Neither did it occur with the subbituminous B Rosebud coal in which the calcium occurs dispersed in the organic matter, partly as carboxylate and (probably) partly as calcite from decomposition of calcium carboxylates. However, about 90% of the average amount of iron oxide is absent from the -10+12 mesh particles of this coal. This is in accord with observations on coal from this seam by other investigators; Kuhn et al. examined pyrite grains in coal ground to pass a 20-mesh sieve and found that all were unattached to coal.(5) The mean diameter of the pyrite grains was 80 μm. Chadwick et al. reported that "pyrite in the coal occurs principally as sheets or film on vertical fracture, or cleat, surfaces."(6)

The distributions in the Kentucky No. 9 particles are shown in Figure 2. To prepare a plot, the particle analyses were arranged in the order of increasing amount of the component, such as iron oxide and the cumulative amount of ash for that order was calculated. Note that a different order of the particles is obtained for each component in the ash of a coal. The plots for iron oxide and basic constituents indicate the presence of two different populations, one with iron oxide content up to about 30 weight percent and the other from 20 to 100 weight percent. It appears likely that the first is from attrital coal and mixtures of attrital coal and vitrain, and the second mainly from vitrain only. Vitrain is recognized as shiny black layers or lenses in the coal thicker than 0.5 mm, and is attributed to the coalification of relatively large fragments of wood and bark. Thus it is almost entirely free of particles of minerals except those, such as pyrite, that are deposited from infiltrating solutions or are present in the woody plant. Alternatively, it is possible that the iron-rich particles contain pyrite of a bedding layer adjacent to vitrain; however, this appears unlikely, as the ash in these particles ranges only from 2.3 to 10.0 weight percent.

The distributions in larger and smaller particles than the -10+20 mesh also should be considered. In general, the distribution is expected to become wider (greater deviation from the average) as particle size decreases; and, for example, the number of particles with a single layer, whether attrital coal or vitrain, increases. The opposite may be true of larger particles, but not if the size of particles is less than that of the predominant width of layers. Ashes of individual -4+5 mesh particles of the Kentucky No. 9 coal are shown in the photograph of Figure 3. Large differences in the iron content of the ash is indicated by the white or gray appearance of some, which have little or no iron, in contrast to others that are very dark because of the presence of hematite from pyrite. This suggests that the distribution of iron in -4+5 mesh particles does not differ much from that of the -10+12 mesh particles.

Distributions in the particles of the Pittsburgh No. 8, Kentucky NO. 13, and Rosebud coal (except for basic constituents) are shown in Figures 4, 5, and 6. Distributions in the particles of the Illinois No. 6 and Indiana VI coals were similar to those of the Kentucky No. 13.

When a knowledge of jet temperatures and a correlation between composition, temperature, and agglomerating tendency becomes available in the future, the distributions will indicate how much of the ash, after burnoff of the char, is immediately available for agglomeration — that is, without need for combination with the ash of a different particle. At present, it is estimated that, in the absence of more than about 2 weight percent of calcium oxide, ash with iron oxide contents from about 20 to 80 weight percent may fall in this category. This upper limit is expected to decrease with decreasing silica-to-alumina ratio and increasing magnesia content, according to phase diagram considerations.(2)

A summary of the distribution of iron oxide in the ash of the -10+12 mesh particles is presented in Table 3 for the eastern bituminous coals, together with

the average iron oxide content. Ash of Kentucky No. 9 coal, from the same mine as that used here, agglomerated without difficulty in U-GAS pilot plant tests with bed temperatures at about 1870°F. (Temperaturea in the jet are substantially higher.) The particle analyses of this coal show 59% of the ash to have 0 to 20 weight percent Fe_2O_3 and 38% to have 20 to 80 weight percent Fe_2O_3. Although the ash of the Pittsburgh No. 8 coal has an average Fe_2O_3 content of 31.7 weight percent, much higher than that of the ash of the Kentucky No. 9, its fraction of ash in the 20 to 80 weight percent Fe_2O_3 range is much lower, only 10%. This suggests that the ash of the Pittsburgh coal should agglomerate more slowly, but its real significance has not been determined as yet. The same is true of the Indiana VI coal, whose total ash has sufficient iron, 15.7 weight percent Fe_2O_3, for agglomeration although very little falls in the 20% to 80% range. The Kentucky No. 13 and Illinois No. 6 coals probably have insufficient iron for agglomeration of their ash, but in this case the ash content of the bed in a gasifier can be allowed to rise to such an extent that very little carbon is ungasified.

Table 3. SUMMARY OF DISTRIBUTION OF Fe_2O_3 IN -10+12 MESH PARTICLES OF EASTERN BITUMINOUS COALS

Coal	Avg. Fe_2O_3 Content, wt %	0-20% Fe_2O_3	20-80% Fe_2O_3	80-100% Fe_2O_3
		% of ash		
Kentucky No. 9	19.9	59	38	3
Pittsburgh No. 8	31.7	61	10	29
Kentucky No. 13	8.1	95	5	0
Illinois No. 6	10.7	93	5	2
Indiana VI	15.7	96	4	0

CONCLUSIONS

The distribution of ash compositions in single particles of coal fed to fluidized bed gasifiers governs the amount and particle size of low-melting ash immediately available as agglomerating medium after burnoff of char from the particles. We have investigated the distribution in the 1/4-inch top size coal from several sources by chemical analysis, for ash content and calcium and iron oxides content of the ash, of 32 particles of the -10+12 mesh fractions of the coals. The distributions, though probably not very accurate, show substantial differences among the coals that were investigated. For example, much of the calcium oxide of the coal, as shown by the conventional analysis for major and minor oxides, was missing from a Kentucky No. 9 seam coal and from an Illinois No. 6 seam coal; the loss was attributed to the presence of calcite in the cleat of the coals, resulting in its attrition from the particles in crushing and other handling. Pyrite in the cleat was similarly lost from particles of some of the coals. Other differences in distribution were also evident; the Kentucky No. 9 coal had a substantial amount of ash with ferric oxide content between 20 and 80 weight percent whereas a Pittsburgh No. 8 coal from Ohio had little of this, although its average iron oxide content was much higher.

Etching by oxygen plasma of 1-1/2-inch pieces of the Kentucky No. 9 coal, sectioned normal to the bedding and lightly polished, furnished a striking display of the prevalence of minerals in the attrital layers of coal and its virtual absence in vitrain, except that the presence of thin plates of calcite in the cleat of the vitrain was clearly evident.

ACKNOWLEDGEMENT

The funds for this research investigation were provided by the Morgantown Energy Technology Center, United States Department of Energy under Contract No.: DE-AC21-84MC21313

REFERENCES CITED

1. Mason, D. M. and Patel, J. G., "Chemistry of Ash Agglomeration in the U-GAS® Process," Fuel Processing Technology 3, 181-206 (1980).

2. Institute of Gas Technology, "Coal Gasification Research Studies," Washington: U.S. Department of Energy, DOE/MC-19301-10, November 1985.

3. Carty, R. H., Mason, D. M. and Babu, S. P., "Reaction Kinetics and Physical Mechanisms of Ash Agglomeration," Washington: U.S. Department of Energy, DOE/MC/61075. To be published in 1987.

4. Moza, A. K. and Austin, L. G., "Analysis of Pulverized Coal Particles (10-100 μm) for Fe, S, Ca, Si and Al on a Particle-by-Particle Basis," Fuel 62, 1468-73 (1983).

5. Kuhn, J. K., Fiene, F. and Harvey, R., "Geochemical Evaluation and Characterization of a Pittsburgh No. 8 and a Rosebud Seam Coal," Report METC/CR-78/8, 1978.

6. Chadwick, R. A., Rice, R. C., Bennett, C. M. and Woodriff, R. A., "Sulfur and Trace Elements in the Rosebud and McKay Coal Seams, Colstrip Field, Montana," Mont. Geol. Soc. Ann. Field Conf. Guide. 22, 167-75 (1975).

APPENDIX

Method of Analysis of Single Particles

Thirty-two coal particles were randomly selected, and individually ashed overnight (16 to 20 hours) in small Pt-5% Au boats. The boats were specially fabricated for this experiment by cutting a 0.006-inch thick Pt-5% Au crucible into 10 X 10 mm squares and folding up all sides to form boxes in the shape of cubes. A Cahn automatic electrobalance Model 25 was employed to obtain the particle and ash weights. The crucible plus ash was dropped into an acid-cleaned 10 ml volumetric flask to which 5 ml of 6N HCl was then added. The flasks were heated on a hot plate to the boiling point until the reddish color of the oxidized iron from the ashed particle solids had disappeared. Cesium chloride and lanthanum chloride solutions were added to the volumetric flask to obtain a final concentration of 1000 mg/l and 2500 mg/l, respectively, as the metal. The volumetric flask was then diluted to volume using double-distilled water. The volume of the Pt-Au crucible did not contribute any significant volume to the solution. The standards were diluted from commercially obtained stock solutions of iron and calcium, and were made to contain Cs, La and HCl matrices the same as those of the samples. Both iron and calcium were determined by atomic absorption spectrophotometry using a Perkin-Elmer 305B double beam instrument.

An observation was made that the coal particles were not completely destroyed by the ashing and acid treatment. Subsequently, the residual solids of the first coal analyzed were collected and analyzed by X-ray fluoresence spectrophotometry utilizing a Phillips 3100 X-ray generator and a PW1410 X-ray spectrometer. Silica was found to be the major constituent. Iron and calcium were found in trace quantities, however their quantities were negligible in comparison with those determined by HCl leaching.

LTA Etching

Pieces of coal about 1-1/2-inch in size were cut across the bedding, and the resulting section was lightly polished and cemented to a 1 X 2-inch glass slide. A parallel cut was made to obtain a section 1/8- to 1/4-inch thick; the top surface was polished by thin section techniques to a final polish with 1000 grit diamond impregnated on a metal disc.

After drying in a vacuum oven the section was exposed for periods of 15 minutes to an hour in an oxygen-plasma LTA asher.

PAP/mason-pap

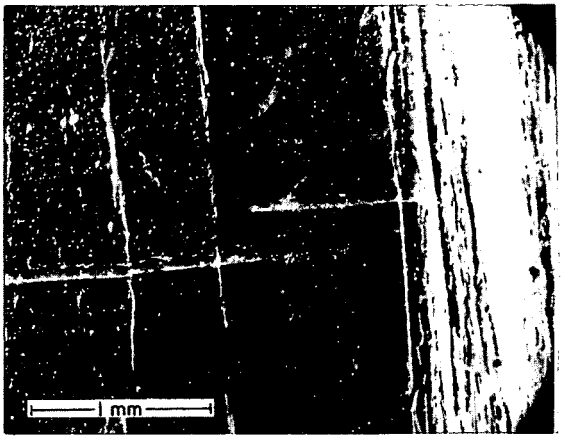

Figure 1. PHOTOMICROGRAPH OF LTA ETCHED KENTUCKY NO. 9 COAL

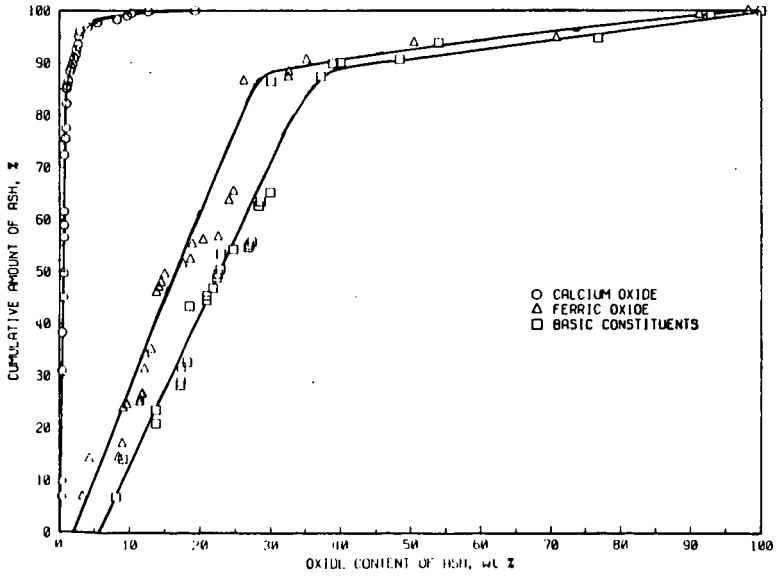

Figure 2. DISTRIBUTION OF BASIC OXIDES IN PARTICLES OF KENTUCKY NO. 9 COAL

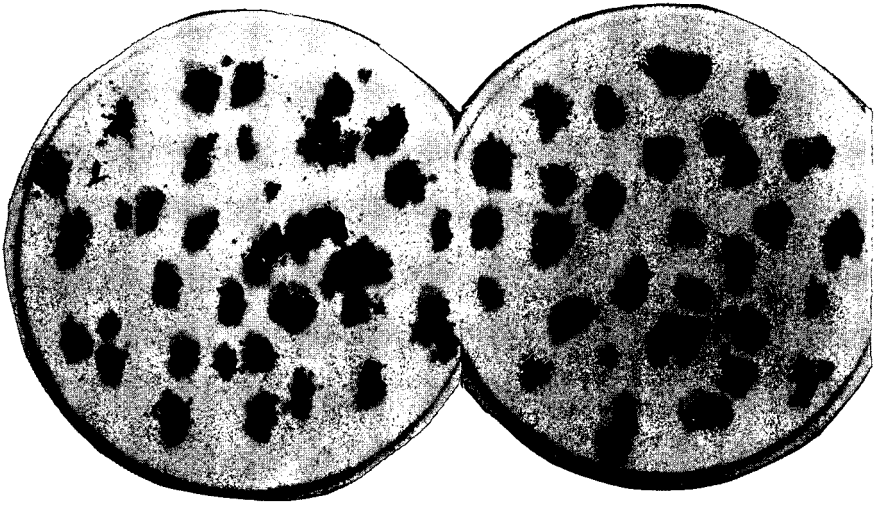

Figure 3. ASH FROM -4+5 MESH PARTICLES OF KENTUCKY NO. 9 COAL

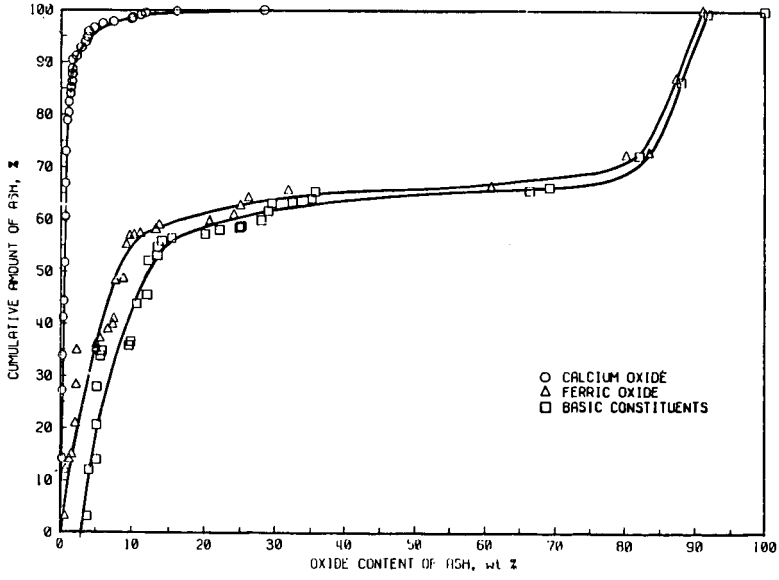

Figure 4. DISTRIBUTION OF BASIC OXIDES IN PARTICLES OF PITTSBURGH NO. 8 COAL

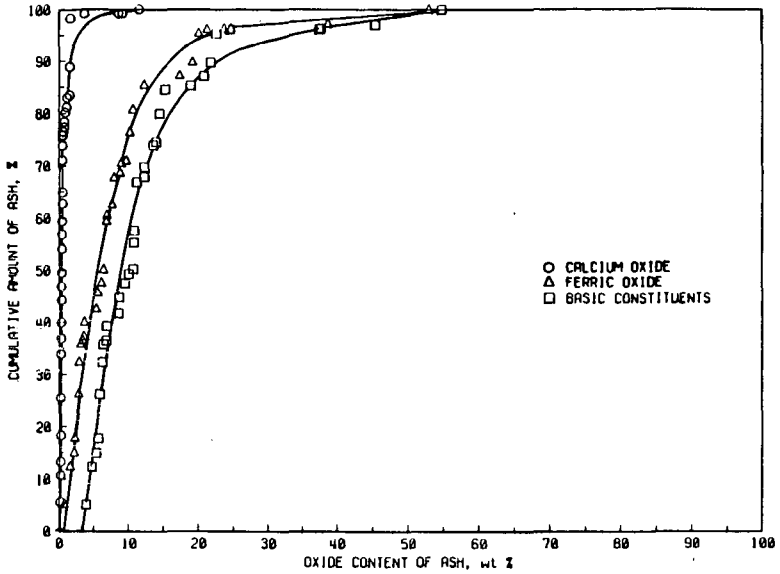

Figure 5. DISTRIBUTION OF BASIC OXIDES IN PARTICLES OF KENTUCKY NO. 13 COAL

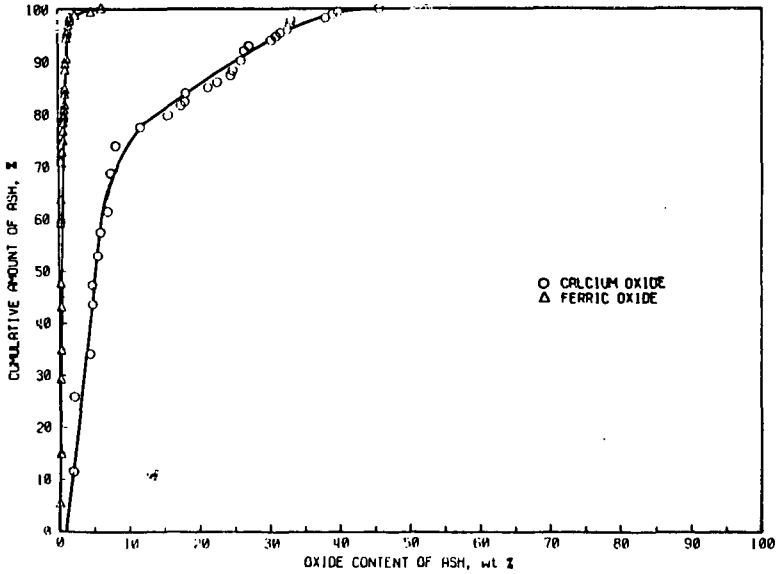

Figure 6. DISTRIBUTION OF FERRIC OXIDE AND CALCIUM OXIDE IN PARTICLES OF ROSEBUD COAL

IMPROVED METHODS FOR DETERMINATION OF FERROUS SULFIDES IN COAL CHARS

S. S. Chao, D. M. Mason, and A. Attari

Institute of Gas Technology, 3424 S. State St., Chicago, IL 60616

INTRODUCTION

A fundamental research investigation of the behavior of mineral matter in fluidized bed gasification of coal is in progress at IGT under a program largely supported by the U.S. Department of Energy. Special attention has been focused on the gasification of high sulfur and high iron containing coals, and the mechanism of ash agglomeration which facilitates the selective removal of ash from a reactor bed without loss of unacceptable amounts of char carbon.

Sulfur occurs in coal mineral mostly as iron disulfides, mainly pyrite with some marcasite. The disulfides quickly decompose to pyrrhotites ($Fe_{(1-x)}S$) and hydrogen sulfide in the charring process with an inert atmosphere or in the absence of air (1-3). The same transformation was also observed when the coal, especially bituminous coal, is fed into the fluidized bed of a gasifier typically at about 1850°F (4). The resulting pyrrhotites may partly transform to troilite (FeS) on cooling to room temperature.

It has been noted that ferrous sulfides, especially pyrrhotite, play a variety of important roles in coal conversion processes. Their possible catalytical activity in coal liquefaction (5) and coal gasification (6,7) was reported recently. In our pilot plant studies we have occasionally found that ferrous sulfide may play an independent role in agglomeration, acting as a binding medium between shale particles in the bed when run-of-mine coal is fed (Fig.1) (4). Under some circumstances, ferrous sulfide has formed deposits in the hot cyclone, which returns entrained char particles to the bed. In order to better understand their functions in coal conversion, an accurate quantitative method for ferrous sulfides determination is needed.

Mossbauer spectroscopy has been employed as a useful method for the semi-quantitative determinations of various iron-containing species including ferrous sulfides in coal chars and gasification residues (8,9). It's accuracy highly depends upon the complexity of the Mossbauer spectra and the concentration level of ferrous sulfides.(10) The major disadvantage of this method is that it can not detect non-iron containing sulfide species, such as calcium sulfide.

X-ray diffraction spectroscopy has also been used to analyze the mineral contents of chars and residues. But, it's utility in the analysis of non-stoichiometric ferrous sulfides is often limited to the qualitative determination, because these sulfides may or may not be present in crystalline forms and their x-ray spectra is often complicated and obscured by the spectra of other major minerals.

In the past IGT has developed a wet chemical method, involving determination of hydrogen sulfide evolved by treating a sample with 6N hydrochloric acid. Although this method was successfully employed to determine the sulfide sulfur contents of chars prepared at 1700°F and gasification residues that had been subjected to higher temperature, it was found to be unsatisfactory when applied to ferrous sulfide-rich coal chars prepared at 1400°F for use as feed for gasification. In most of cases only a fraction of sulfur from ferrous sulfide (sulfide sulfur) could be recovered as hydrogen sulfide. The calculated total sulfur of these chars from sulfide sulfur, pyritic sulfur and organic sulfur is usually 5 to 20% lower than the total sulfur determined by the Eschka method, depending on the types of ferrous sulfides present and their concentration.

In the search of a more accurate method, we have re-evaluated a number of potential existing methods and developed a few new methods for ferrous sulfides analysis. The most successful method uses a reducing agent to enhance the recovery of ferrous sulfide as hydrogen sulfide in a hydrochloric acid evolution procedure. Results from the analyses of six 1400°F coal chars using different methods are presented and discussed.

EXPERIMENTAL

Two model coal char compounds synthesized from high purity carbon plus a composite 1400°F coal char sample were prepared for the initial study of the recovery of sulfide sulfur during hydrochloric acid digestion. The first model consists of troilite and the second a natural pyrrhotite. Using an acid-evolution train, the efficiencies of hydrogen sulfide evolution were examined for these three samples at four hydrochloric acid concentrations (1,2,4 and 6 normal) with and without the addition of the reducing agent, stannous chloride. The hydrogen sulfide evolved was collected in an alkaline trap composed of 10% cadmium chloride in water and subsequently determined by an iodometric method with thiosulfate back titration. The hydrochloric acid extract was then filtered and analyzed by atomic absorption method for the HCl-soluble iron. The residue collected was examined by an x-ray diffraction spectroscopic (XRD) method for the amount of ferrous sulfide left intact.

For the composite coal char, a complete sulfur-by-types analysis was also carried out to check the sulfur mass balance. A modified method of ASTM D-2492 procedure for forms of sulfur in coal was employed to analyze the sulfate, pyritic, organic, and total sulfur. The sulfate sulfur was determined by a gravimetric method as barium sulfate. The pyritic sulfur was calculated from the concentration of pyritic iron found in the dilute nitric acid extract of the residues, which was determined by an atomic absorption method. The organic sulfur was determined by digesting the residue from the dilute nitric acid digestion with concentrated nitric acid and analyzing the resulting sulfate as barium sulfate gravimetrically. The total sulfur was determined by the Eschka method.

In the course of a gasification investigation, five coal chars were prepared at 1400°F in a 4-inch diameter devolatilizer purged with nitrogen from washed bituminous coals with 1/4-inch top size. The residence time of the feed coal at 1400°F was approximately 30 minutes. A -200 mesh fraction of Kentucky No. 9 coal was used to prepare the sixth coal char. All samples were ground to about 325 mesh and analyzed for their contents of sulfide sulfur, residual sulfur, 6N HCl-soluble iron and total iron. Both the residual sulfur and total sulfur were determined by the Eschka method. The 1N, 1.6N (5%) and 2N HCl-soluble iron were also determined separately and used to calculate the sulfide sulfur content.

A Philips vertical goniometer and a copper x-ray source were employed for the x-ray diffraction analysis of all coal char samples. The total concentration of iron sulfides was determined using potassium chloride as an internal standard. The diffraction peak at a 2 theta angle of about 43.3 degree was used for the quantitation. The same peak was also profile-fitted in an attempt to deconvolute the complex peaks, measuring their precise d-spacings at the 102 crystal plane and consequently estimating the iron content of various hexagonal pyrrhotites (11).

A Ranger Scientific MS-900 Mossbauer spectrometer with a 5 mCl Co-57 source was used to acquire Mossbauer spectra of all char samples. The relative percentage of sulfide iron in total iron as ferrous sulfides was measured by a spectral subtraction technique. The concentration of sulfide sulfur in each coal char was calculated by multiplying the total iron percentage of coal char by the relative percentage of sulfide iron and a S/Fe conversion factor of 0.574.

RESULTS AND DISCUSSION

Figure 2 represent the effects of hydrochloric acid and the reducing agent, stannous chloride, on the recovery of sulfide sulfur by the described evolution method. By comparison of the mole ratios of sulfide sulfur to HCl-soluble iron, we found that the troilite (FeS) could be easily decomposed to hyrogen sulfide and determined quantitatively. However, pyrrhotite was not completely converted to hydrogen sulfide even though all ferrous sulfides would be completely decomposed in hydrochloric acid with a concentration higher than 2 normal as indicated by XRD analysis of the digested residue, unless a suitable reducing agent, such as stannous chloride, was present. We believe that pyrrhotite is partially degraded to elemental sulfur in the hydrochloric acid medium as the following equation. The stannous chloride and possible other reducing agents may inhibit this competitive degradation mechanism, converting all sulfide sulfur to hydrogen sulfide.

$$Fe_{(1-x)}S + 2\,(1-x)\,HCl \xrightarrow{\Delta} (1-x)\,FeCl_2 + (1-x)\,H_2S + S^0$$

The results in Table 1 indicate that a good sulfur mass balance was obtained when 10% or more stannous chloride was used. The insignificant difference between the calculated total sulfur of 2.02% and 2.05% while using 4N and 6N HCl respectively suggests that either concentration is adequate for effective hydrogen sulfide evolution. The variation of the mole ratios of sulfide sulfur to HCl soluble iron in the same table further confirms that stannous chloride definitely promotes the hydrogen sulfide evolution. The sulfide sulfur calculated from 2N HCl-soluble iron provides good agreement with the determined sulfide sulfur using stannous chloride. This method could be used as a quick method to determine the sulfide sulfur in coal char, provided that there are little other types of HCl-soluble iron, such as iron oxides, iron sulfates, illites and chlorites, present in the sample.

Table 1. Sulfur-by-types analysis of a composite 1400°F Coal Char

Digestion Acid Promoting Agent	4N HCl	4N HCl 10% $SnCl_2$	4N HCl 20% $SnCl_2$	6N HCl	6N HCl 10% $SnCl_2$
Sulfate Sulfur %	<0.01	<0.01		<0.01	<0.01
Sulfide Sulfur %	.66	1.04	1.07	.74	1.04
Pyritic Sulfur %	.06	.05		.06	.04
Organic Sulfur %	1.06	.93		1.05	.97
Total S % (calc.)	1.78	2.02		1.85	2.05
Total S % (detn.)	2.09	2.09		2.09	2.09
HCl Soluble Fe %	1.81	1.84	1.86	1.92	1.88
S/Fe Mole Ratio	.64	.98	1.00	.67	.96
2N HCl-Soluble Fe	1.81	1.84	1.86	1.92	1.88
Sulfide S % (calc. from Fe)	1.05	1.07	1.08	1.11	1.09

We found also that the organic sulfur contents determined in the procedure without stannous chloride are higher than those found in the procedure with stannous chloride. This is probably because the elemental sulfur, formed during the hydrochloric acid digestion, may be partially associated with the solid residue and recovered as organic sulfur in the subsequent concentrated nitric acid digestion. This indicates that the acid evolution method without stannous chloride is likely to give a high estimation of organic sulfur in char in addition to a low quantitation of sulfide sulfur.

Table 2 presents the concentrations of sulfide sulfur, residual sulfur and total sulfur of six coal chars. The total sulfur calculated from the sulfide and residual sulfur was again found to agree well with the determined total sulfur in all analyses when stannous chloride was used in the evolution procedure. The mole ratios of sulfide sulfur to the HCl-soluble iron deviate significantly from unity in four analyses, indicating the presence of other 6N HCl-soluble iron species in those char samples. However, the quick method to determine the sulfide sulfur using the percentage of iron soluble in 1N, 1.6N (5%) and 2N HCl seems to be quite satisfactory in most of the cases (Table 3). Further studies should be conducted to select an optimum hydrochloric acid concentration for this method.

Another method, using the relative percentage content of the sulfide iron determined by Mossbauer spectroscopy and the total iron percentage in char to calculate the sulfide sulfur, was successfully employed. However, only the results of two coal char samples with high ferrous sulfide content were reported in Table 3. They agree quite well with the data reported by the evolution method. Greater difficulties were encountered in analyzing the rest of the samples because of their relatively low iron concentration and the presence of various other iron species. During this study, we found that pyrrhotites ($Fe_{(1-x)}S$) with varying stoichiometric quantity of sulfur may give different Mossbauer spectra, rendering the Mossbauer spectral subtraction technique inaccurate, especially when no suitable pyrrhotite standards were available.

Table 2. Determination of sulfide sulfur of 1400°F coal chars using HCl evolution method

1400 °F Coal Char	Sulfide S %	Residual S %	Total S % (Calc)	Total S % (Detn.)	HCl-Soluble Fe %	S/Fe (Mole)
Kentucky No. 9						
(with $SnCl_2$)	.90	1.38	2.28	2.50	2.00	.78
(w/o $SnCl_2$)	.57	1.53	2.10		1.97	
Kentucky No. 9 (prepared from -200 mesh coal fines)						
(with $SnCl_2$)	.74	1.30	2.04	2.14	1.65	.78
(w/o $SnCl_2$)	.24	1.35	1.59		1.64	
Pittsburgh No. 8						
(with $SnCl_2$)	2.11	.90	3.01	2.96	3.76	.98
(w/o $SnCl_2$)	1.70	1.12	2.82		3.70	
Kentucky No. 13						
(with $SnCl_2$)	.30	.68	.98	1.02	.60	.87
(w/o $SnCl_2$)	.04	.85	.89		.60	
Illinois No. 6						
(with $SnCl_2$)	1.44	1.35	2.79	2.79	2.46	1.02
(w/o $SnCl_2$)	.87	1.61	2.48		2.40	
Rosebud						
(with $SnCl_2$)	.56	.74	1.30	1.33	1.20	.81
(w/o $SnCl_2$)	.30	.93	1.23		1.18	

Table 3. Comparison of methods for sulfide sulfur analysis of 1400°F Coal Chars

1400 °F Coal Char	Sulfide S % (determined) w/o $SnCl_2$	Sulfide S % (determined) with $SnCl_2$	Sulfide S % (calculated) From Mossbauer	From HCl-soluble Fe (1N)	(1.6N	(2N)	(6N)
Kentucky No. 9	.57	.90	ND	.87	.80	.88	1.13
Kentucky No. 9 (-200 mesh coal)	.24	.74	ND	.76	.81	.84	.94
Pittsburgh No. 8	1.70	2.11	2.07	2.08	2.05	1.98	2.12
Kentucky No. 13	.04	.30	ND	.30	.30	.30	.34
Illinois No. 6	.87	1.44	1.41	1.35	1.37	1.33	1.38
Rosebud	.30	.56	ND	.61	.60	.57	.68

NOTE: ND = not determined.

No results from XRD analysis were reported at this time. The quantitative method using potassium chloride as an internal standard gave erroneous results because no effective method was developed yet to resolve and quantitate the broad and deformed x-ray peak corresponding to diffractions at the crystal 102 planes of various ferrous sulfides. The even broader XRD background induced by the char itself further complicates the XRD spectra. In order to achieve better accuracy in the quantitative measurement of total ferrous sulfide, the sensitivity of diffraction from each of the different ferrous sulfides must also be determined.

CONCLUSION

A hydrochloric acid evolution method using stannous chloride as a promoting agent was developed and employed successfully for ferrous sulfides determination in 1400°F coal char. This method not only provides an accurate analysis of ferrous sulfides, but also improves the accuracy of the organic sulfur analysis of coal char. We believe this method could be and should be employed in the sulfur-by-types analysis of all coal derivatives containing ferrous sulfides.

Among other methods studied, the methods using 1N, 1.6N (5%) and 2N HCl-soluble iron to calculate the ferrous sulfides content could be employed to determine the ferrous sulfides content in coal char, provided that little other HCl-soluble iron species are present. The method using Mossbauer spectroscopy to determine the sulfide iron concentration and atomic absorption spectroscopy to determine the total iron would be a good technique, if pyrrhotite standards as well as other iron standards resembling the iron species in coal char were found. Further Mossbauer apectroscopic studies with temperature control may provide more information and may simplify the current procedure. X-ray diffraction spectroscopy also encounters a similar problem caused by various ferrous sulfides with discrete composition and structures. However, the latter problem is even more significant and tends to be too complex to resolve.

ACKNOWLEDGMENT

The funds for this research investigation were provided by the Morgantown Energy Technology Center, United States Department of Energy under Contract No. DE-AC21-84MC21313 and The Institute of Gas Technology under IR&D Project 20317.

The authors would like to thank Ms. K. L. Crippen for her technical assistance in analyzing the samples.

REFERENCE

(1) M. Saporoschenko, et.al., "Mossbauer spectroscopic studies of the mineralogical changes in coal as a function of cleaning, pyrolysis, combustion and coal conversion processes," FUEL 59, 567 (1980).

(2) I. Stewart, S. G. Whiteway, P. J. Cleyle, and W. F. Caley, "Decomposition of pyrite in a coal matrix during the pyrolysis of coal." Mineral Matter and Ash in Coal, K. S. Vorres, ed. ACS Symposium Series No. 301, 485 (1985).

(3) P. A. Montano, V. Shah, S. Reddy and A. S. Bommannavar, "Mossbauer study of the transformation of iron minerals during coal conversion," New Approaches in Coal Chemistry, ACS Symposium Series 169, 377 (1981).

(4) R. H. Carty, D. M. Mason and S. P. Babu, "Reaction kinetics and physical mechanisms of ash agglomeration," Final Report to U.S. Department of Energy, March 1987 (DE-AC21-84MC21313).

(5) M. G. Thomas, T. D. Padrick, F. V. Stohl and H. P. Stephens, "Decomposition of pyrite under coal liquefaction conditions: a kinetic study," FUEL 61, 761 (1982).

(6) K. J. Huttinger and W. Krauss, "Catalytic activity of coal minerals in hydrogasification of coal," FUEL 60, 93 (1981).

(7) O. P. Mahajan, A. Tomita, J. R. Nelson and P. L. Walker, Jr., "Differential scanning calorimetry studies on coal. 2. Hydrogenation of coals," FUEL 56, 33 (1977).

(8) A. S., Bommannavar and P. A. Montano, "Mossbauer study of the thermal decomposition of FeS_2 in coal," FUEL 61, 523 (1982).

(9) Pedro A. Montano, "Characterization of iron-bearing minerals in coal," Coal Structure, M. L. Goorgbatz and K. Ouchi, ed. ACS Advances in Chemistry Series 192, 337 (1981).

(10) R. H. Carty, D. M. Mason and S. Babu, "Coal gasification research studies," Report to U.S. Department of Energy for Aug. 1983 through Nov. 1983 (DOEMC/19301-5).

(11) J. R. Craig and S. D. Scott, "Sulfide phase equilibria," Sulfide Mineralogy, P. H. Ribbe, Volume 1, s-21, November 1974.

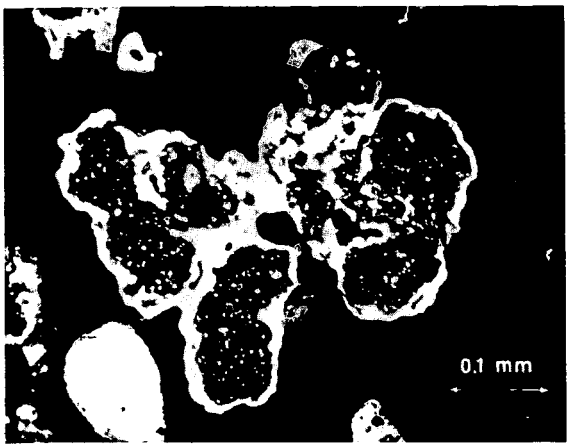

Figure 1. FeS (white) Joining Shale Particles in Bed Material From a Pilot-Plant Run on Run-of-Mine Coal

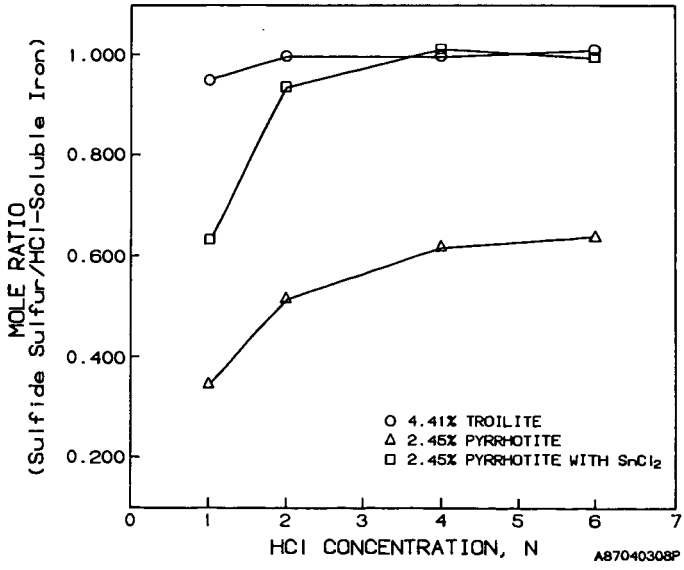

Figure 2. Recovery of Ferrous Sulfide as Hydrogen Sulfide in a Hydrochloric Acic Evolution Procedure With and Without Stannous Chloride